

Università degli Studi di Napoli Federico II  
Dipartimento di Scienze Fisiche



## TESI SPERIMENTALE DI DOTTORATO

# Scanning Probe Techniques for the Characterization of Electronic Properties of Transition Metal Oxide Surfaces and Interfaces

Supervisore:

Dr. Marco Salluzzo

Coordinatore:

Prof. Antonello Andreone

Candidato

Zoran Ristić

22° Ciclo di Dottorato



Scanning Probe Techniques for the  
Characterization of Electronic Properties of  
Transition Metal Oxide Surfaces and Interfaces

Zoran Ristić

November 2009



*for Sofija...*



## Abstract

Scanning tunneling spectroscopy has been a window into the (sub)atomic world for more than two decades now, but the wealth of information that this technique offers seem yet to be exploited to its maximum. In this thesis it is tried to optimize STM and, more precisely, STS techniques for the investigation of transition metal oxides, especially ones that exhibit interesting correlated structural and electronic phenomena like  $\text{Pr}_{1-x}\text{Ca}_x\text{MnO}_3$  and  $\text{LaAlO}_3/\text{SrTiO}_3$  system; the first is an insulator characterized by intriguing magnetic and charge-ordered phases, and the second is unique example of 2D electron gas, confined to the buried interface between two band-insulators. To this purpose, different numerical methods are proposed, which greatly help the handling of the data obtained in STS measurements. This approach allowed to determine important correlations between structural and electronic properties of the TMO surfaces/interfaces investigated in this thesis.



# Contents

<b>List of figures</b>	<b>v</b>
<b>List of Tables</b>	<b>xi</b>
<b>Introduction</b>	<b>1</b>
<b>1 Scanning Tunneling Microscopy</b>	<b>5</b>
1.1 Principles of scanning tunneling microscopy . . . . .	6
1.1.1 Quantum mechanical tunneling effect . . . . .	6
1.1.2 Piezoelectric effect . . . . .	11
1.1.3 Electronics and the Feedback Loop . . . . .	12
1.1.4 Mechanical decoupling . . . . .	14
1.2 MODA system . . . . .	15
1.2.1 Growth chamber . . . . .	15
RHEED	
Reflection high-energy electrons diffraction . . . . .	16
1.2.2 Analysis chamber . . . . .	18
XPS . . . . .	18
SPA-LEED . . . . .	19
1.2.3 Omicron VT-AFM	
Variable Temperature	
Atomic Force Microscope . . . . .	20
VT-AFM stage and UHV chamber . . . . .	20
Preamplifier stage . . . . .	22
MATRIX control system . . . . .	23
PC control and analysis software . . . . .	24
1.2.4 STM and AFM tip preparation . . . . .	25
1.3 SPM modes . . . . .	26
1.3.1 STM - Topography . . . . .	26
1.3.2 STM - Spectroscopy . . . . .	27

1.3.3	AFM - Topography . . . . .	28
	Contact AFM . . . . .	29
	Non-contact AFM . . . . .	30
<b>2</b>	<b>Numerical methods</b>	<b>31</b>
2.1	Differentiating noisy curves- total variation regularization . . . . .	32
2.1.1	Numerical example . . . . .	35
2.1.2	TVR applied on experimental curves: example . . . . .	37
2.2	Normalization of differential tunneling conductance . . . . .	38
2.2.1	Total conductivity normalization . . . . .	39
2.2.2	Ukrainitsev normalization . . . . .	40
2.2.3	Normalization comparison . . . . .	41
2.3	K-means classification method . . . . .	42
2.3.1	Two-dimensional observation example . . . . .	46
2.4	Summary . . . . .	46
<b>3</b>	<b>Pr<sub>1-x</sub>Ca<sub>x</sub>MnO<sub>3</sub>: general considerations</b>	<b>47</b>
3.1	Strongly correlated materials . . . . .	47
3.1.1	Transition metal oxides . . . . .	48
3.1.2	Manganites . . . . .	52
3.2	Pr <sub>1-x</sub> Ca <sub>x</sub> MnO <sub>3</sub> . . . . .	53
3.2.1	Structure . . . . .	53
3.2.2	Phase diagram . . . . .	54
3.3	STM on manganites . . . . .	57
3.4	Summary . . . . .	61
<b>4</b>	<b>Scanning tunneling spectroscopy on Pr<sub>1-x</sub>Ca<sub>x</sub>MnO<sub>3</sub> thin films</b>	<b>63</b>
4.1	Pr <sub>0.5</sub> Ca <sub>0.5</sub> MnO <sub>3</sub> . . . . .	63
4.2	Pr <sub>0.7</sub> Ca <sub>0.3</sub> MnO <sub>3</sub> . . . . .	75
4.3	Summary . . . . .	84
<b>5</b>	<b>LaAlO<sub>3</sub> on SrTiO<sub>3</sub> 2D electron gas at the interface:</b>	
	<b>Overview</b>	<b>85</b>
5.1	LaAlO <sub>3</sub> . . . . .	85
5.2	SrTiO <sub>3</sub> . . . . .	86
5.3	LaAlO <sub>3</sub> on SrTiO <sub>3</sub> . . . . .	88

5.4	SPM/STS measurements on LaAlO <sub>3</sub> /SrTiO <sub>3</sub> interface . . . . .	97
5.5	Summary . . . . .	98
<b>6</b>	<b>Scanning tunneling spectroscopy on LaAlO<sub>3</sub> on SrTiO<sub>3</sub> systems</b>	<b>99</b>
6.1	Tunneling through insulating barrier . . . . .	99
6.2	4 u.c. LaAlO <sub>3</sub> on SrTiO <sub>3</sub> . . . . .	101
6.3	2 u.c. LaAlO <sub>3</sub> on SrTiO <sub>3</sub> . . . . .	116
6.4	Summary . . . . .	119
<b>7</b>	<b>Conclusion</b>	<b>121</b>
	<b>Bibliography</b>	<b>123</b>
	<b>Acknowledgments</b>	<b>133</b>



# List of Figures

1.1	Principal scheme of STM device . . . . .	6
1.2	Schematics of quantum mechanical tunneling effect . . . . .	7
1.3	The energy diagram of the STM tunneling process . . . . .	8
1.4	Typical construction of an a) $z$ cylindrical motor; b) $x,y$ scanner piezoelectric motor . . . . .	12
1.5	Block diagram of typical negative feedback realization in STM instruments. . . . .	13
1.6	MODA facility(down) and schematic top view (up) . . . . .	15
1.7	Layer by layer surface growth and corresponding RHEED oscillation . . . . .	17
1.8	The principles of X-ray photoemission technique . . . . .	19
1.9	Schematic diagram of OMICRON Nanotechnology GmbH SPA-LEED installed on MODA system . . . . .	20
1.10	Block diagram of Omicron VT-AFM . . . . .	21
1.11	3D model of the Omicron VT-SPM . . . . .	21
1.12	Schematics of MATRIX system architecture for the basic STM experiment . . . . .	23
1.13	Omicron VT-AFM STM (left) and AFM(right)tip holder . . . . .	25
1.14	Two operational modes of STM a) constant current mode b) constant height mode . . . . .	26
1.15	The measurement of differential conductance by <i>lock-in</i> technique . . . . .	28
1.16	The force-distance curve between the tip and the sample material in atomic force microscopy measurements. . . . .	28
1.17	Contact AFM functioning principle . . . . .	29
1.18	Non contact AFM functioning principle . . . . .	30
2.1	The comparison of TVR differentiation method to finite differences differentiation of smoothing curve method as a function of present noise . . . . .	36

2.2	Comparison of spectra obtained by lock-in technique and numerical TVR method on set of 250 spectra; . . . . .	37
2.3	Calculation of a single I(V) curve differential (a) by TVR (blue) and SPIP (red) and average of single I(V) curves differentials calculated by TVR (blue) and SPIP (red) (c,d,e) . . . . .	38
2.4	Influence of small parameter $\epsilon$ on NDC curves a) Total conductance normalization b) $\ln I/\ln V$ normalization . . . . .	42
2.5	a) I(V) characteristic (obtained by averaging a spectroscopic set) and b) different normalization done for the optimized parameters ( $\epsilon$ being of the order of noise current) . . . . .	42
2.6	The schematic diagram of the application of the K-means algorithm on STS data. . . . .	43
2.7	Illustration of k-means algorithm in two-dimensional space with $n = 47$ , $k = 3$ . . . . .	45
3.1	Energy diagram of two types of strongly correlated insulators .	48
3.2	Perovskite structure; $SrTiO_3$ example . . . . .	49
3.3	Crystal field lifting of 3d level degeneracy . . . . .	50
3.4	The shape of d-orbitals . . . . .	50
3.5	Occupation of 3d sub-shells for two different Mn valences . . .	52
3.6	PCMO structure and correspondence between orthorhombic and pseudo-cubic unit cell parameters. . . . .	54
3.7	Phase diagram for $Pr_{1-x}Ca_xMnO_3$ . . . . .	55
3.8	Effect of applied a) pressure and b) magnetic field on $Pr_{1-x}Ca_xMnO_3$ resistivity . . . . .	55
3.9	The CE-type magnetic structure present in $x=0.5$ PCMO at low temperatures. . . . .	56
3.10	Evolution of insulating and metallic domains just below $T_C$ with magnetic field . . . . .	57
3.11	Maps of conductance peak separation $\Delta_B$ at different temperatures from Seiro et al. . . . .	58
3.12	I-V curves obtained 115 K on a bond stripe by Sudheendra et al. . . . .	59
3.13	Topographic (left) and spectroscopic atomic-scale signatures (right) of phase separation into metallic and insulating regions in the paramagnetic phase of $Bi_{0.24}Ca_{0.76}MnO_3$ at 299 K. . . .	59
3.14	Topographic atomic-scale images probing occupied states and unoccupied states on $La_{5/8-0.3}Pr_{0.3}Ca_{3/8}MnO_3$ thin film grown on Nb-doped (001)-oriented $SrTiO_3$ . . . . .	60
3.15	The topographic images obtained on <i>in situ</i> cleaved $La_{1.4}Sr_{1.6}Mn_2O_7$ . . . . .	61

4.1	RHEED oscillation during the growth of PCMO(x=0.5) (left) and RHEED pattern after the deposition (right) . . . . .	65
4.2	XRD and rocking curve of PCMO(x=0.5) thin film on NGO . . . . .	65
4.3	X-ray reflectivity measurements and the fit for the 10 nm thickness . . . . .	66
4.4	NC-AFM image of PCMO(x=0.5) thin film surface . . . . .	66
4.5	Step edge profile (left) and corresponding height histogram distribution (right) for the NC-AFM measurement presented in Fig. 4.4 . . . . .	67
4.6	STM image of PCMO(x=0.5) thin film surface, $I_{SET}=500$ pA; $V_{BIAS}=1$ V . . . . .	68
4.7	Step edge profile (left) and corresponding height histogram distribution (right) for the STM measurement presented on Fig. 4.6 . . . . .	69
4.8	a) Terrace details, showing that the layer is incomplete, and b) corresponding segment image identifying valleys (uncovered parts) of the surface . . . . .	69
4.9	STM image of re-annealed PCMO(x=0.5) thin film surface, $I_{SET}=2$ nA; $V_{BIAS}=1.25$ V . . . . .	70
4.10	Step edge profile (left) and corresponding height histogram distribution (right) for the STM measurement presented in Fig. 4.9 . . . . .	70
4.11	The terrace detail showing not fully covered layer of PCMO(x=0.5) on NGO after annealing . . . . .	71
4.12	Parts of the sample characterized by a topography consisting of double terminated islands present also on a single terrace away from the edges . . . . .	72
4.13	K-means classification applied on the normalized conductivity data with different number of classes assumed. Upper row: the whole voltage range is included during classification process; lower: only values outside the gap were used ( $V_{BIAS} \geq 0.4$ ) . . . . .	73
4.14	K-means classification image for the 2 classes (left) and corresponding medians of the spectra by class (right). . . . .	74
4.15	K-means classification image for the 3 classes (left) and corresponding medians of the spectra by class (right). . . . .	74
4.16	K-means classification image for the 2 classes (left) and corresponding medians of the spectra by class (right). . . . .	75
4.17	RHEED oscillation during the growth of PCMO(x=0.3) (left) and RHEED pattern after the deposition (right) . . . . .	76
4.18	STM image of re-annealed PCMO(x=0.5) thin film surface, $I_{SET}=2$ nA; $V_{BIAS}=1.25$ V . . . . .	77

4.19	Step edge profile (left) and corresponding height histogram distribution (right) for the STM measurement presented in Fig. 4.18 . . . . .	77
4.20	The stripe region and corresponding profile reveal 4 nm distance between stripes on PCMO(x=0.3) thin film on B-terminated STO . . . . .	78
4.21	The topographic image obtained during STS measurement on PCMO[x=0.3] thin film on STO . . . . .	79
4.22	a) The result of the k-means classification for 2,3 and 4 assumed classes taking into account whole spectra, only negative voltages and only positive voltages; b) corresponding average spectra for each class shown on a) (the curves and classes are appropriately color coded) . . . . .	80
4.23	a) The result of the k-means classification for 2,3 and 4 assumed classes taking into account whole spectra, only negative voltages and only positive voltages excluding the gap states in each b) corresponding average spectra for each class shown on a) (the curves and classes are appropriately color coded) . . .	81
4.24	Gap map obtained from STS data on PCMO(x=0.3) (left) and corresponding gap histogram of the gap value distribution. . .	83
4.25	Map of average surface potential obtained from STS data on PCMO(x=0.3) using Ukraitsev tunneling probability function(left) and corresponding $\Phi$ histogram. . . . .	83
4.26	Map of tip to surface separation obtained from STS data on PCMO(x=0.3) using Ukraitsev tunneling probability function(left) and corresponding w histogram. . . . .	83
5.1	Structure of LaAlO <sub>3</sub> . . . . .	86
5.2	Universal band structure for transition metal/rare earth oxide dielectrics . . . . .	87
5.3	Structure and DOS of SrTiO <sub>3</sub> . . . . .	87
5.4	Two possible LaAlO <sub>3</sub> /SrTiO <sub>3</sub> interfaces. . . . .	89
5.5	Charge, field and potential distribution for two possible LaAlO <sub>3</sub> /SrTiO <sub>3</sub> interfaces. . . . .	90
5.6	Charge, field and potential distribution for two possible LaAlO <sub>3</sub> /SrTiO <sub>3</sub> electronically reconstructed interfaces. . . . .	91
5.7	Density of states of the n-type LaAlO <sub>3</sub> /SrTiO <sub>3</sub> interface and charge and orbital ordered state of Ti ions . . . . .	92
5.8	The conductance threshold thickness was found to be 3 u.c. in n-type LaAlO <sub>3</sub> /SrTiO <sub>3</sub> system . . . . .	93

5.9	Density of states and layer-resolved density of states calculated for n-type, 1-5 u.c. thin, LaAlO <sub>3</sub> film on SrTiO <sub>3</sub> . . . . .	94
5.10	Results of XAS measurements . . . . .	94
5.11	The role of the deposition oxygen pressure on the final state of LAO STO interface. . . . .	95
5.12	a-d) patterning technique for fabricating all LAO/STO device; e) Schematics of the AFM patterning experiment where positively biased AFM tip "writes" the conductive line at the interface of 3 u.c. thin film f) the change in channel conductance as the tip reaches second electrode. . . . .	96
5.13	Cross-section C-AFM on LaAlO <sub>3</sub> on SrTiO <sub>3</sub> interface . . . . .	98
6.1	The energy diagrams associated with tunneling through insulating barrier. . . . .	100
6.2	C-AFM image of LaAlO <sub>3</sub> /SrTiO <sub>3</sub> 4 u.c. thin film surface . . .	102
6.3	Step edge profile (left) and corresponding height histogram distribution (right) for the C-AFM measurement presented on Fig. 6.2 . . . . .	103
6.4	Current-distance dependence on 4 u.c. LAO/STO and gold . . .	103
6.5	Single measurement current-voltage characteristic and corresponding calculated differential conductance . . . . .	104
6.6	Different topographic response when working above and below CBM at 4 u.c. LAO/STO system . . . . .	105
6.7	Proposed mechanism to address step edge sizes much greater than 1 u.c. in LAO/STO measurements below CBM. . . . .	106
6.8	STM image on 4 u.c. showing ordered pattern . . . . .	107
6.9	The analysis of ordered pattern on 4 u.c. LAO/STO . . . . .	108
6.10	Autocorrelation image of on terrace part of the sample and corresponding profile enhancing the real space periodicity showing quasi-rectangular lattice . . . . .	109
6.11	Topographic image, autocorrelation map and 2D FFT obtained during STS measurement . . . . .	109
6.12	a) Average I(V) curve obtained from the whole spectra set; b) Average of all dI/dV(V) calculated at each point using SPIP and TVR; c) Average normalized conductivity obtained by using dlnI/dlnV method calculated using SPIP and TVR . . . . .	110
6.13	The result of the k-means classification for 2,3 and 4 assumed classes on LaAlO <sub>3</sub> /SrTiO <sub>3</sub> bilayer - gap included . . . . .	111
6.14	The result of the k-means classification for 2,3 and 4 assumed classes on LaAlO <sub>3</sub> /SrTiO <sub>3</sub> bilayer - gap not included . . . . .	112

6.15	Small scale $32 \times 32 \text{ nm}^2$ topographic, class, cross-correlation images and averaged spectra on LAO/STO . . . . .	114
6.16	C-AFM image of $\text{LaAlO}_3/\text{SrTiO}_3$ 2 u.c. thin film surface . . .	116
6.17	Step edge profile (left) and corresponding height histogram distribution (right) for the C-AFM measurement presented on Fig.6.16 . . . . .	117
6.18	STM image obtained on 2 u.c. LAO/STO system under ambient light . . . . .	118
6.19	a) Evolution of NDC and b) peak shift with time and light intensity; c) average NDC for different light intensities. . . . .	118
6.20	Comparison between average 4 u.c normalized conductivity spectra and that of photo-doped 2 u.c.. LAO/STO bilayer . .	120

# List of Tables

1.1	Scanning probe techniques and corresponding feedback. . . . .	5
-----	---	---



# Introduction

Scanning tunneling microscopy and spectroscopy [STM/STS], for a quarter of a century, has been used to probe the electronic and the structural properties of conducting surfaces, helping to understand the physics happening at the surfaces of many materials. In the case of strongly correlated materials, the full potentialities of STM/STS has been demonstrated by the studies on high  $T_c$  superconductors, since in these materials the majority of interesting phenomena occurs near the Fermi level and at low temperatures, where STS is able to determine the local density of states quantitatively. However, recently, there are activities to better understand the tunneling process away from the Fermi level, also in the case of other systems, often characterized by semiconducting and sometimes insulating characteristics. Among them, the class of transition metal oxides [TMO] are considered quite promising for the possibilities to implement new functionality in modern electronics. Indeed, transition metal oxides exhibit a plethora of interesting electronic, magnetic and structural phenomena often present simultaneously in the same material, competing with each other and thus giving rise to the possible applications in devices.

In this framework, this thesis is devoted to the optimization of the STM and, more precisely, of the STS techniques for the investigation of transition metal oxides, with a special attention toward compounds exhibiting interesting structural and electronic phenomena, like  $\text{Pr}_{1-x}\text{Ca}_x\text{MnO}_3$  thin films and  $\text{LaAlO}_3/\text{SrTiO}_3$  interface.  $\text{Pr}_{1-x}\text{Ca}_x\text{MnO}_3$  is an insulating material characterized by interesting charge order and magnetic phases depending on the doping level and on the temperature, while the  $\text{LaAlO}_3/\text{SrTiO}_3$  interface is an example of 2D electron gas confined to the buried interface below a thin  $\text{LaAlO}_3$  insulating film. Moreover, an attempt to unveil the possible physical mechanisms happening in these materials has been tried, by applying the novel analytical techniques developed in this thesis.

The outline of the thesis is presented in Chapter 1. Moreover, a general introduction to the STM/STS technique will be given, together with the description of the experimental setup used to achieve the experimental

results.

In the second Chapter, the numerical algorithms developed here to determine, from the STS measurements, the local density of states of badly conductive or even insulating materials at room temperature, will be presented. This is done by using STS in the spectroscopic mode, where only  $I(V)$  curves are acquired, allowing faster and more stable measurements compared to the standard lock-in implementation, usually used especially in the case of superconductors. In particular, a robust numerical algorithm for differentiating  $I(V)$  curves, called Total Variation Regularization (TVR), is introduced. Moreover, the problematic associated to the normalization of the spectroscopic data is addressed since, differently from superconductors, here interesting features in the DOS are often far from the Fermi level. Therefore, the role of the energy dependence of the tunneling probability should be taken into consideration with a particular care. At the end of the chapter, a method for classification of spectra in the spatial resolved STS map measurements, called K-means, is proposed to help more easily the identification of surface electronic inhomogeneities in the spectral response of surfaces and interfaces.

In Chapter 3, an overview of STM/STS studies done on correlated TMO is presented, with a general introduction to the field of correlated material and with a focus on manganites and, more specifically, on  $\text{Pr}_{1-x}\text{Ca}_x\text{MnO}_3$ . The chapter is completed with a short summary of the main experimental results obtained by STM/STS on manganites.

The STM/STS measurements on  $\text{Pr}_{1-x}\text{Ca}_x\text{MnO}_3$  thin films, with doping  $x=0.3$  and  $0.5$ , are presented in Chapter 4. The measurements are done for the doping concentrations corresponding, in the phase diagram, to the boundaries of the charge-orbital-ordered phase. In both system, it was possible to demonstrate a correlation between topographic and electronic inhomogeneities. In particular in the  $x=0.5$  phase, we found that PrCaO terminated islands show a more insulating character than MnO<sub>2</sub> terminated layers. For the  $x=0.3$  phase, nanostructured domains observed in the first layers close to the interface, exhibit a more insulating characteristic, and larger gap, again demonstrating a strong correlation between structural and electronic properties of the surface.

Chapter 5 introduces the  $\text{LaAlO}_3/\text{SrTiO}_3$  system that gained strong interest in the last years, being one of the few example of two dimensional [2D] electron gas realized at the interface between two band-insulator transition metal oxides. The possible role of the electron correlations in the physics of this system, attracted the attention of the condensed matter community. An overview of some of the theoretical and experimental results obtained in the last years is presented. At the end of this chapter, the state of art of

scanning probe microscopy [SPM] studies in this field is shortly summarized.

Finally, the STM/STS measurements done on the  $\text{LaAlO}_3/\text{SrTiO}_3$  system are presented in Chapter 6. The results obtained on 4 u.c. (conducting interface) and 2 u.c. (insulating)  $\text{LaAlO}_3/\text{SrTiO}_3$  bilayers, grown by the Augsburg group of Prof. J. Mannhart, will be presented. The data show different spectral responses, as expected. In particular the presence of an intriguing superstructure, correlated with an inhomogeneous response, in the case of the conducting 4 u.c. bilayer, has been interpreted as signature of important structural and orbital reconstruction of the interface. At the same time, we found the insulating 2 u.c. bilayer become locally conducting when light is impinged onto the surface, by a photo-doping effect.

In the last chapter, a summary of the results with the possible outlook for further measurements is presented.



# Chapter 1

## Scanning Tunneling Microscopy

The development of the family of scanning probe microscopes starts with the original invention of the scanning tunneling microscope (STM) by Gerd Binnig and Heinrich Rohrer at IBM Zurich Research Laboratories in Switzerland in 1981 [1]. Binnig and Rohrer were awarded with the Nobel prize for their invention just 5 years later.

The significance of their discovery is reviewed in the possibility to overcome the diffraction limits of optical and electron microscopes that were limiting the view into the atomic world. It also opened the road to plethora of new scanning probe techniques that do not necessary use tunneling effect but that strongly rely on the technology behind STM (table 1.1).

The STM works by scanning a very sharp metal wire (TIP) over a surface which properties are being investigated (SAMPLE) [Fig. 1.1]. By bringing the tip very close to the sample, and by applying an electrical voltage to the tip or to the sample, one can image the surface at an extremely small scale down to resolving individual atoms. This is possible due to the tunneling current that is an exponential function of tip-sample separation.

$$I_T(w) = I_0 e^{-2kw} ; k = \sqrt{\frac{2m\phi}{\hbar}} \quad (1.1)$$

Table 1.1: Scanning probe techniques and corresponding feedback.

Technique	Feedback
Scanning Tunneling Microscopy	tunneling current
Contact Atomic Force Microscopy	force (caniliver bending)
Non-contact Atomic Force Microscopy	force (frequency shift)

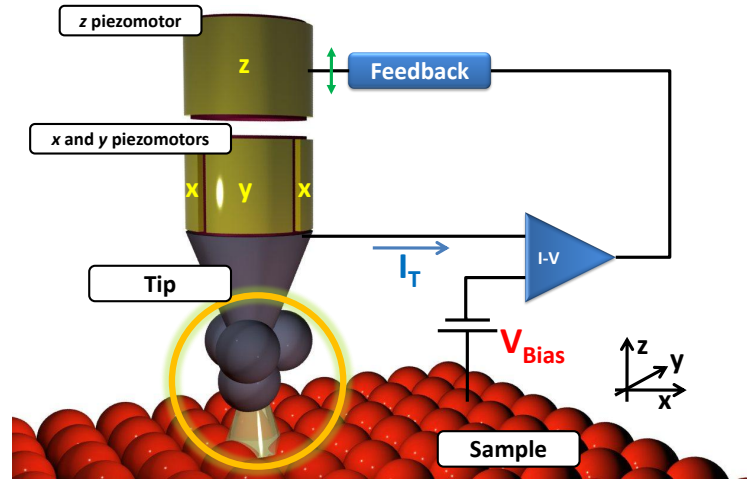


Figure 1.1: Principal scheme of STM device

To understand in more details how the STM operates several principles, discussed in the next chapter, must be introduced.

### 1.1 Principles of scanning tunneling microscopy

There are several principles that made the realization of STM possible:

- Quantum mechanical tunneling effect
- Piezoelectric effect
- Electronics and the feedback loop
- Mechanical decoupling

#### 1.1.1 Quantum mechanical tunneling effect

Quantum mechanical tunneling effect, which has no counterpart in classical physics, describes the propagation of the particle wave function  $\Psi(E, \mathbf{r})$  through the thin potential barrier of height  $\phi$  and width  $w$ , such that  $\phi > E$ , where  $E$  is the total energy of the particle [Fig. 1.2].

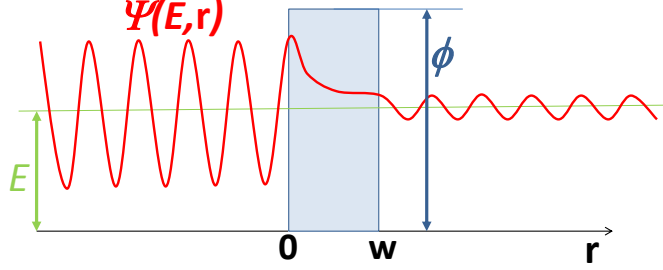


Figure 1.2: Schematics of quantum mechanical tunneling effect

As a quantum mechanical phenomenon, tunneling effect was known since the early days of quantum mechanics. It was George Gamow who, in 1928, first used the idea of introducing tunneling phenomena to describe the alpha decay of a nucleus [2]. The generality of the quantum-mechanical tunneling was quickly recognized.

If the tunneling particles are electrons, a tunneling current occurs when electrons move through a barrier classically forbidden. The wave-function amplitude (the square-root of the probability to find the particle at a given spatial coordinate) decays rapidly through the barrier (the decay is exponential in the case of a constant height barrier in one-dimensional case), so to have a finite probability of finding the particle at the opposite side of the barrier thickness  $w$  should be very small. Hence, for a thin enough barrier and large enough number of electrons, measurable currents can be produced by electron tunneling from one electrode to the other.

In the STM, tunneling takes place between two electrodes [Fig. 1.3]: S-sample electrode of the investigating material and T -tip, a metallic point probe electrode. When the two electrodes are brought in close proximity, the tunneling effect takes place. The tunneling process is described by the eq. 1.2 and 1.3

$$dI_{T \rightarrow S}(E, V, w) \cong \int A \frac{2\pi e}{\hbar} \left(\frac{\hbar^2}{2m}\right)^2 T(E, V, w) \rho_S(E) f(E) \rho_T(E - eV) (1 - f(E - eV)) dE \quad (1.2)$$

$$dI_{S \rightarrow T}(E, V, w) \cong \int A \frac{2\pi e}{\hbar} \left(\frac{\hbar^2}{2m}\right)^2 T(E, V, w) \rho_T(E - eV) f(E + eV) \rho_S(E) (1 - f(E)) dE \quad (1.3)$$

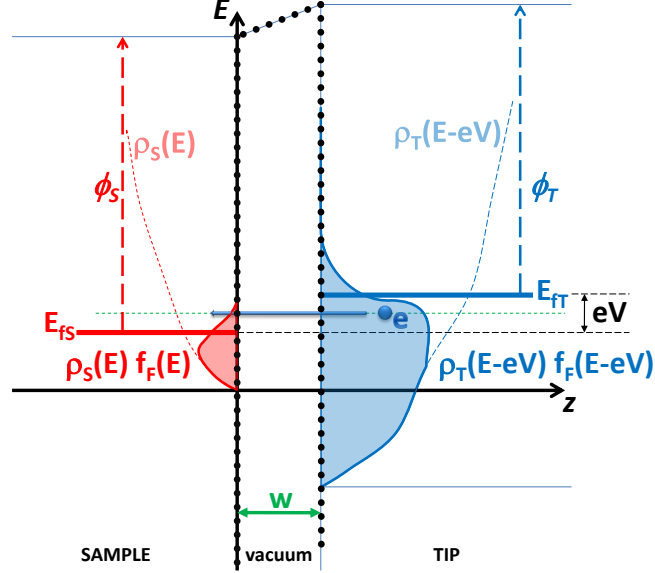


Figure 1.3: The energy diagram of the STM tunneling process with voltage  $V$  measured referenced to the tip potential

Equation 1.2 describes positive current flow from the tip to the sample as a consequence of electron tunneling in opposite direction (from the sample to the tip). Similarly equation 1.3 describes positive current flow from the sample to the tip as a consequence of electron tunneling in opposite direction (from the tip to the sample). At certain energy  $E$ , the tunnelling process depend on the the tip and the sample electronic properties, so that the tunnelling current is proportional to the product of the corresponding density of states ( $\rho_T(E)$  and  $\rho_S(E)$ ) and the Fermi-Dirac distribution function that describes occupancy of the available states at certain temperature  $T$  for fermions  $f(E)$  given by Eq. 1.4.

$$f(E, T) = \frac{1}{1 + e^{-\frac{E - E_f}{k_B T}}} \quad (1.4)$$

Here  $k_B$  is a Boltzmann constant and  $E_f$  is Fermi level of the material.

In this frame eq. 1.2 simply states that the tunneling current corresponding to transfer of electron (charge) from the sample to the tip, is proportional to the product of available electrons in the sample, the available unoccupied states in the tip, the area of the tunneling contact and the tunneling transmission probability  $T(E, V, w)$ . This probability is a function of the tip to sample separation  $w$  and for trapezoidal barrier in the WBK approximation

is given by the expression eq. 1.5:

$$T(E, V, w) \cong \exp \left\{ -2w \left( \frac{2m}{\hbar^2} \left[ \bar{\Phi} + \frac{eV}{2} - E \right] \right)^{\frac{1}{2}} \right\} \quad (1.5)$$

Here  $\bar{\Phi}$  represents the average work function of the tip and the sample (Eq. 1.6).

$$\bar{\Phi} = \frac{\phi_T + \phi_S}{2} \quad (1.6)$$

Conventionally, the total net current is represented in such a way that it has positive values when the majority of the electrons tunnel from the tip to the sample. This corresponds to a positively biased sample electrode respect to the tip. The total net current can be then expressed as:

$$\begin{aligned} dI(E, V, w) &= dI_{S \rightarrow T}^{TOT}(E, V, w) = dI_{S \rightarrow T}(E, V, w) - dI_{T \rightarrow S}(E, V, w) \\ dI(E, V, w) &\cong \\ &A \frac{2\pi e}{\hbar} \left( \frac{\hbar^2}{2m} \right)^2 T(E, V, w) \rho_S(E) \rho_T(E - eV) (f(E - eV) - f(E)) dE \end{aligned} \quad (1.7)$$

Or when integrated over all energies:

$$\begin{aligned} I(V, w) &\cong \\ &A \frac{2\pi e}{\hbar} \left( \frac{\hbar^2}{2m} \right)^2 \int_{-\infty}^{\infty} T(E, V, w) \rho_S(E) \rho_T(E - eV) (f(E - eV) - f(E)) dE \end{aligned} \quad (1.8)$$

In the equilibrium case, when no bias voltage is applied between the electrodes, the number of electrons that tunnel from the tip electrode to the sample electrodes is equal to the number of electrons tunneling from the sample to the tip electrode, resulting in a zero net current.

If a bias voltage is applied, however, depending on the local density of states of the sample and the tip, in general a non-zero tunneling current will exist, corresponding to electrons moving from the lower potential to the higher potential electrode.

The Eq. 1.8 can be simplified by assuming  $f_T(E)$  and  $f_S(E)$  to be Heaviside step functions with step at  $E_{fT}$  and  $E_{fS}$  for the tip and the sample respectively. At the room temperature the value of  $k_B T$  is  $\approx 26$  meV. This value introduces energy resolution limit when trying to determine  $\rho_S(E)$ . So for all the measurements, with a much lower energy resolution, the stated assumption can be used. The consequence of this is that instead of integral

## 1. Scanning Tunneling Microscopy

---

over all the energies, one can obtain the current only by integrating in the  $[0, eV]$  range, and Eq. 1.8 becomes:

$$I(V, w) \cong \tag{1.9}$$

$$A \frac{2\pi e}{\hbar} \left(\frac{\hbar^2}{2m}\right)^2 \int_0^{eV} T(E, V, w) \rho_S(E) \rho_T(E - eV) dE$$

Since the goal is to probe the density of states of the sample one should notice that the differential conductance  $dI/dV$  as a function of  $V$ , obtained by differentiating Eq. 1.9, is given by (Eq. 1.10):

$$\frac{dI(V, w)}{dV}(V, w) \cong \tag{1.10}$$

$$A \frac{2\pi e}{\hbar} \left(\frac{\hbar^2}{2m}\right)^2 T(E, V, w) \rho_T(E - eV) \rho_S(E) \Big|_{E=eV}$$

$$+ \int_0^{eV} \frac{dT(E, V, w)}{dV} \Big|_{E=eV} \rho_T(E - eV) \rho_S(E) dE$$

$$+ \int_0^{eV} T(E, V, w) \frac{d\rho_T(E - eV)}{dV} \Big|_{E=eV} \rho_S(E) dE$$

If few more assumptions are taken into consideration, the equation 1.10 can be simplified even further and can be used to determine the sample density of states function ( $\rho_S(E)$ ) from the bias voltage dependence of the current ( $I(V)$ ), obtained in the constant barrier width condition ( $w = const$ ). The assumption usually considered are:

- $\rho_T(E) = \rho_T(E_{gT}) = const.$ ; since the tip is usually made of a good conductor, electrons in it are behaving like free electrons with effective mass  $m^*$ . For the case of 3D electron gas the  $\rho_T(E)$  has a square like dependence and thus making it possible to consider  $\rho_T(E) = const$  if the Fermi level  $E_{fT}$  is deep inside the conduction band;
- $T(E, V, w) = T(E, w)$ ; this assumption states that the tunneling transmission probability does not change with the applied voltage. This is generally true only for small bias voltages, when one is observing states near the Fermi level. For higher voltages, though, the bias voltage does change the profile of the potential barrier and consequently also  $T(E, V, w)$ . In the chapter 2.2 the influence of bias voltage on the tunneling transmission probability will be discussed in more details;

When these assumptions are applied to Eq. 1.10 the second and the third term can be considered to be equal to zero, thus leading to the simple relation between the differential conductance and sample density of states :

$$\frac{dI(V, w)}{dV} \cong A \frac{2\pi e}{\hbar} \left(\frac{\hbar^2}{2m}\right)^2 T(eV, w) \rho_T(E_{fT}) \rho_S(eV) \quad (1.11)$$

Although a term  $T(eV, w)$  is present and depends on the bias voltage, since it is already assumed that  $eV$  is small and in particular  $eV \ll \bar{\Phi}$  we have:

$$T(eV, w) = T(w) = \exp \left\{ -2w \left( \frac{2m}{\hbar^2} \bar{\Phi} \right)^{\frac{1}{2}} \right\} \quad (1.12)$$

So the tunneling transmission probability is a function only of tip to sample distance  $w$  and for fixed  $eV$  it is responsible for the exponential like decrease of the tunneling current with barrier thickness, as mentioned in Eq. 1.1.

The barrier itself can be any kind of insulating material. In the STM implementation, the insulating medium is in general the vacuum.

In a planar configuration, the tunneling technique was used to measure the work function and density of states of materials by using one electrode with a known work function. As a barrier an insulating thin film layer was used (tunnel junction). This approach gave only the information averaged on a large area of the sample. On the contrary using a point probe (a tip) instead of a planar electrode, allowed to determine the surface properties locally. The major problem with tip electrode approach, that is the STM configuration, was how to maintain a fixed distance between the two electrodes separated by few tenths of nanometers. Therefore, technical limits made the realization of the first STM difficult. Once the problem of mechanically decoupling of the two electrodes from the external perturbations was solved, the road to the STM device was opened by means of introducing damping stages, and the utilization of the feedback concept and piezo motors, for fine approach of the tip to the surface.

### 1.1.2 Piezoelectric effect

In order to achieve tunneling conditions in STM, one must maintain the separation between the tip and sample small enough, i.e. of order of nanometers. Even more, at the nanoscale, the effects of thermal drift and vibrations is huge and require that either the tip or the sample vertical position ( $z$ -position) are regulated with extreme precision. Piezoelectric motors are, in this sense, the best solution. Apart from the movement in the vertical  $z$ -direction, a fine

subatomic scale movement is required also in the lateral  $x$  and  $y$  direction. Again piezoelectric motors represent the efficient solution to this problem.

The reverse piezoelectric effect, discovered by Pierre Curie in 1880, is the effect that drives piezoelectric motors. The piezoelectric effect is created by squeezing the sides of certain crystals, such as quartz, barium titanate and  $\text{Pb}_{1-x}\text{Zr}_x\text{TiO}_3$  (PZT). The result is the creation of opposite charges on both sides (potential difference arises between two opposite sides) and mechanical deformation. The effect can be reversed as well; by applying a voltage across a piezoelectric crystal, it will elongate or compress. By using inverse piezoelectric effect it is possible to control the elongation of the piezo crystals by simply applying a potential difference between the two faces of the crystal [Fig. 1.4].

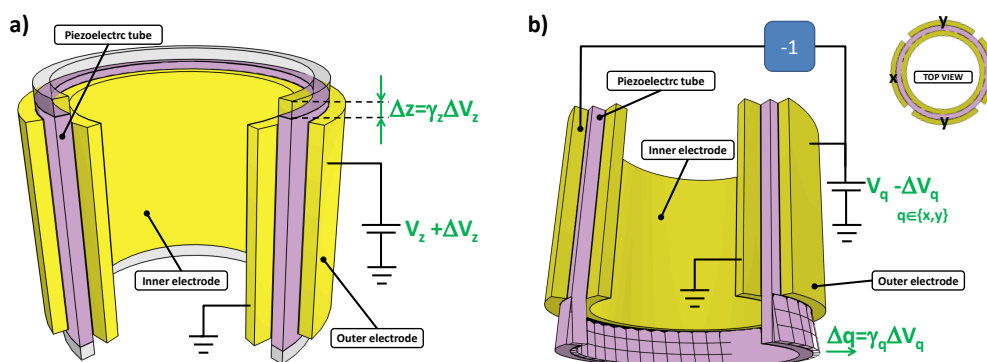


Figure 1.4: Typical construction of an a)  $z$  cylindrical motor; b)  $x,y$  scanner piezoelectric motor

Piezoelectric motors are used to scan the tip in an STM, and in the majority of other scanning probe microscopy (SPM) techniques. A typical piezoelectric material used in SPMs is the PZT.

### 1.1.3 Electronics and the Feedback Loop

In an STM, because of the effects mentioned in previous section (thermal drift and external vibration), Not only the tunneling barrier has to be small, but the barrier thickness, i.e. the distance between the tip and the sample, should be kept constant over time. This not easily achieved even when no lateral scanning is involved because of the external perturbations. To solve the problem of constant tip to sample separation, the concept of negative feedback is applied to piezo-motors, regulating their position so that the certain parameter (in the case of STM, the tunneling current) is kept constant.

In table 1.1, an overview of various SPM techniques and feedback controlling parameter are listed. The concept of negative feedback implementation in STM is shown in Fig. 1.5

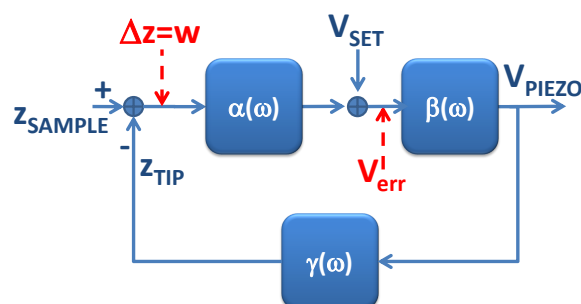


Figure 1.5: Block diagram of typical negative feedback realization in STM instruments.

Here  $Z_{SAMPLE}$  and  $Z_{TIP}$  represent the vertical position of the sample and the tip respectively,  $\Delta z$  or  $w$  is the vacuum barrier thickness,  $\alpha(\omega), \beta(\omega), \gamma(\omega)$  are transfer functions of amplifying, regulation and piezo stage respectively,  $V_{SET}$  is the voltage that corresponds to the desired set current and  $V_{err}$  is the error signal, a measure of difference between the measured and desired current, that needs to be regulated (minimized). The ratio between bias voltage  $V_{BIAS}$  (or more general the voltage across the insulating barrier) and a set current  $I_{SET}$  is called tunneling resistance and it is related to the tip to sample separation. Lower tunneling resistances correspond to smaller  $w$  (Eq.1.13).

$$R_T = \frac{I_{SET}}{V_{BIAS}} \quad (1.13)$$

Apart from the feedback, one needs an electronics to measure the current, scan the tip, and to translate this information into a form that can be used. In this regard a pre-amplifier stage, a current to voltage converting stage just after the tunneling junction, is of most importance for the function of STM and STS. In particular the gain and the dynamic properties of the pre-amplifier stage determine the noise level and thus the detection limit of the device. Also the dynamic properties, the bandwidth of the pre-amplifier, will limit the speed at which one can measure either topographic or spectroscopic images and maps. Later on will be shown what is the effect of the bandwidth on the acquisition of differential conductance by the lock-in approach in scanning tunneling spectroscopy measurements.

Since the tunneling currents are usually in  $10 - 10^5 pA$  range, the effect of external electromagnetic fields on the measurement must also be considered. A good shielding of the instrument and prevention of ground loops, in this regard, is of huge importance. Also, one of the ways to protect the acquisition process from the influence of external electromagnetic fields, is digitalization of the acquired signal as close as possible to the signal source, as in the case of our instrument. Digitalization also lowers the chance of crosstalk occurrences.

### 1.1.4 Mechanical decoupling

The last part of the STM 'puzzle' that had to be solved to successfully implement the idea of local probe in the scanning tunneling microscope, was the need to decouple the tunneling junction from the external vibration sources. Even with the concept of piezo-motors and feedback in place, due to the nm-distances barrier thickness, any external mechanical vibration could easily lead to the tip-sample contact, thus making the tunneling experiment unstable.

In the first STM by Binnig and Rohrer, magnetic levitation was used to keep the STM decoupled from external vibrations; now internal spring suspension system with eddy current damping is often used, as in the case of our instrument.

Eddy currents are generated in a conductor in a time-varying magnetic field. They are induced either by the movement of the conductor in the static field or by changing the strength of the magnetic field, initiating motional and transformer electromotive forces (emf). In the case of eddy current damping, in STM the magnetic field is usually produced by permanent magnets and the movement of the STM stage, usually coupled to the copper frame, is responsible for eddy current generation. The generated eddy currents create a repulsive force that is proportional to the velocity of the conductor such that the moving magnet and conductor behave like a viscous damper. The eddy current generation causes the vibration of the STM stage frame to dissipate through the Joule heating generated in the conductor part.

Very often, STM instruments are placed on the sand bases or concrete blocks that are decoupled from the foundation of the building they are in. Sometimes STM is put in special acoustic shield rooms and if UHV conditions are needed, pumps that produce vibrations (turbomolecular, mechanical) are located further away from the system, and if possible they are turned off during the experiment.

## 1.2 MODA system

The experimental results presented in this thesis are obtained on the Modular facility for Oxides Deposition and Analysis (MODA) shown in figure 1.6

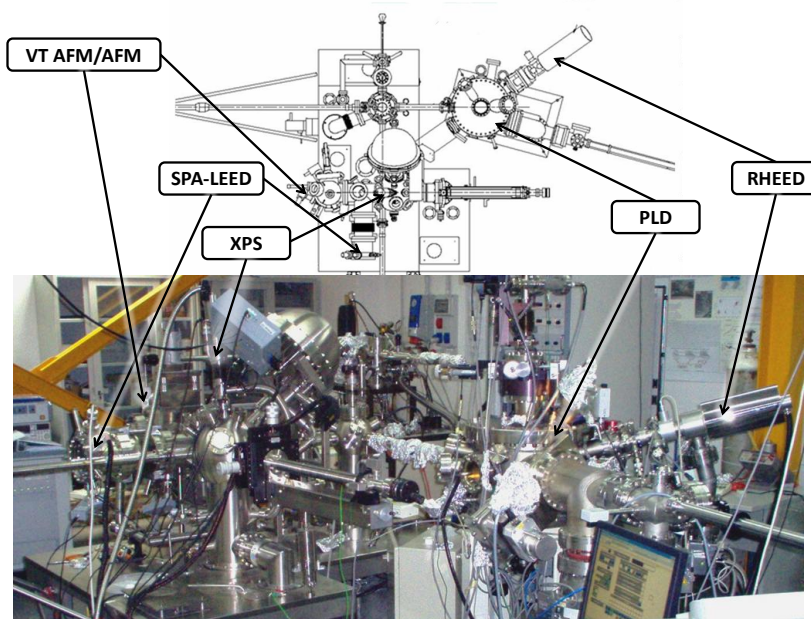


Figure 1.6: MODA facility(down) and schematic top view (up)

The facility is a system for pulsed laser deposition (PLD) of oxide thin films and for the *in-situ* analysis of their properties. As seen from Fig. 1.6, several surface sensitive techniques have been set up: Reflection high-energy electrons diffraction - RHEED, fast Intensified Charge Couple Device - ICCD camera, Spot Profile Analysis - Low energy electrons diffraction - SPA-LEED, X-ray Photo-emission Spectroscopy - XPS, Scanning Tunnel Microscopy - STM and Atomic Force Microscopy - AFM. There is also KrF excimer laser present for the ablation of stoichiometric targets.

The system consists of two major parts: thin film growth chamber and analysis chamber. More details about this two parts with the emphasis on Omicron variable temperature scanning probe microscope (VT-SPM) will be discussed in the following sections.

### 1.2.1 Growth chamber

Thin film growth takes place in a vacuum chamber devoted to the pulsed laser deposition process (PLD). The base pressure in the chamber is in the

range of  $10^{-9}$  mbar. UHV conditions are maintained by means of mechanical and turbo-molecular pumps. It is isolated from the other part of the UHV system by valves and long channels that are used for the transfer rods but at the same time they introduce high vacuum resistance, making it possible to keep different UHV conditions in different parts of the MODA system. A separated load-lock chamber for the target introduction is also present, making it possible to introduce new targets without influencing UHV conditions in the growth chamber.

When depositing oxide films, control of the oxygen pressure is of great importance. It influences the dynamics and shape of the plume but at the same time is of great importance for keeping the deposited films well oxygenated. The pulsed laser deposition of complex oxides is performed using 99.999% oxygen as a deposition gas. The deposition atmosphere was maintained by increasing a vacuum resistance between the turbo pump and the chamber (controlling the opening of the valve) and introducing flowing oxygen gas by means of a mass flow meter into the chamber to attain overall dynamic pressures between  $10^{-5}$  mbar up to 0.5 mbar  $O_2$ .

Once the substrate is introduced into the growth chamber, it is resistively heated using an heater based on wire made of a platinum alloy. The deposition temperature is read by a thermocouple (calibrated by pyrometer) and controlled by means of an electronic feedback system. The maximum deposition temperature is  $1000^\circ$  C. When growth substrate temperature is reached and the geometrical position of the substrate regarding the target is set by means of step-motor positioning system, the deposition process starts. The motion of the heater, the pressure, the laser, the temperature, the loading and motion of the carousel and a selection of the targets are fully software controlled.

The laser ablation is done by KrF excimer laser operating at  $\lambda = 248$  nm, with  $t_{PULSE} = 25$  ns FWHM. A mask is used to select the homogeneous part of the laser beam. The mask is projected at an inclination of  $45^\circ$  on the target by means of a focusing lens (the focal length is 50 mm). The energy density on the target is controlled by adjustment of both mask size and demagnification.

### **RHEED**

#### **Reflection high-energy electrons diffraction**

The film deposition process is monitored *in-situ* by a high pressure RHEED (Reflection High Energy Electron Diffraction) that operates also in the regime of high dynamic oxygen pressure due to the differential pumping mechanism allowing the filament, that produces electrons, as well as accelerated electron

optics, be at the low base pressure while the deposition is done in dynamic  $O_2$  pressure.

RHEED allows to determine *in-situ* the growth mechanism and to monitor the evolution of the surface structure with sub-monolayer sensitivity [3, 4]. It is based on the elastic diffraction of electrons (there is no energy transfer from the electron to the surface) with high kinetic energy (typically in the range of 5-50 keV) and low impact angle (typically less than 5) from the solid surface. The reflected electrons then impinge on the phosphorous screen revealing a pattern that depends on the structure, morphology and roughness of the sample surface. The pattern represents the intersection of the reciprocal lattice of the two dimensional surface layer (ideally a lattice of rods) and the equi-energetic sphere in k space (Ewald sphere).

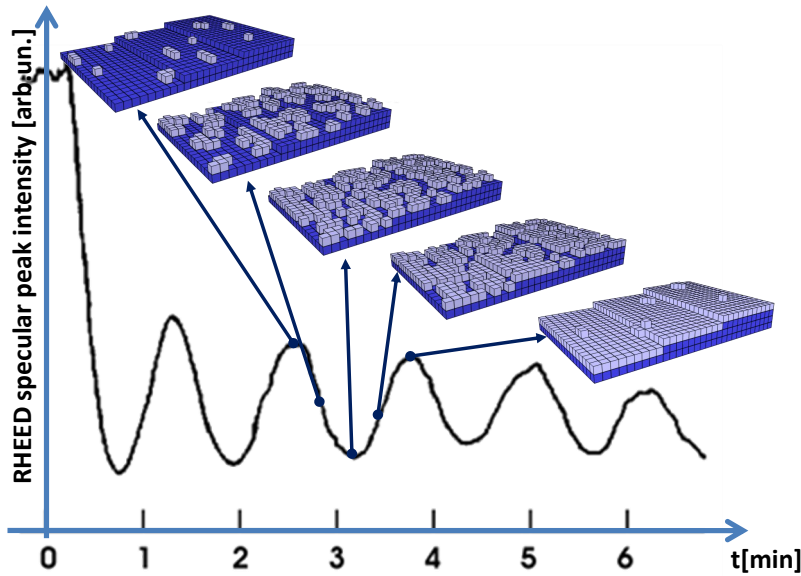


Figure 1.7: Layer by layer surface growth and corresponding RHEED oscillation

Apart from the structural analysis of the planar surface symmetries, the intensity of specular spot (rod), depends on the film roughness making it possible to monitor the film growth in the layer by layer growth regime by observing the oscillation of the intensity (Figure 1.7).

### 1.2.2 Analysis chamber

Once the sample is prepared in the growth chamber or introduced in the MODA system through the introduction chamber, it is first transferred to distribution chamber. The role of the chamber is not merely to collect and distribute samples and substrates, it also acts as a vacuum buffer between, in vacuum sense, 'dirty' growth chamber and analytic chamber that has to be in perfect vacuum condition (down to low  $10^{-11}$  mbar). The UHV in both distribution and analytic chamber is maintained in the same way by means of sequentially connected mechanical and turbo-molecular pump (enabling  $10^{-9}$  mbar base pressure) and ion and titanium sublimation pump that put the base pressure down to  $10^{-11}$  mbar. UHV conditions are very important if one is to investigate surface properties. If UHV conditions are not good, contamination of the surface takes place making the results unreliable.

There are several surface sensitive techniques implemented in the analytical part of MODA system:

- X-ray Photoemission spectroscopy - **XPS**
- Spot Profile Analysis - Low Energy Electrons Diffraction - **SPA-LEED**
- Variable Temperature Scanning Probe Microscopy - **VT-SPM**

#### XPS

In X-ray photo-emission spectroscopy, an x-ray source emits photons impinging on the investigated sample. This x-ray photon interacts with the electrons in the sample by transferring energy and momenta to them. If energy of the photon  $h\nu$  is sufficiently high that an electron can overcome its binding energy  $E_B$  and the work function of the sample  $\phi$  it will leave the sample with the kinetic energy  $E_K$  such that [Eq. 1.14]:

$$h\nu = E_B + \phi + E_K \quad (1.14)$$

This mechanism allow one to analyze the energy distribution of emitted electrons and reconstruct the electronic structure of the sample [Fig. 1.8] and from there the chemical composition and electronic states of elements present in the sample. This is possible since each element has different spectral signature in this respect and, even more, different ionic states of the same element also have different spectral signatures, so both type and the valence can be determined.

Non-destructive nature of the XPS technique makes it very popular in the chemical analysis of the surfaces.

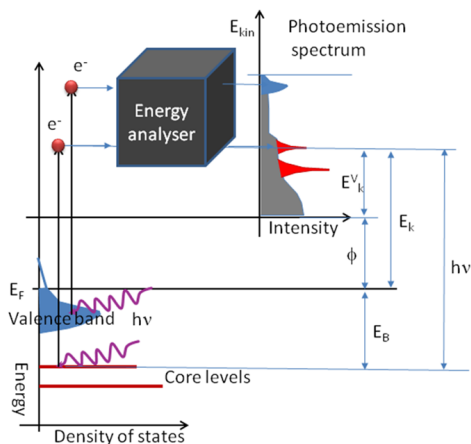


Figure 1.8: The principles of X-ray photoemission technique

Our XPS system is Omicron one with standard Omicron X-ray dual anode non-monochromatic sources that operate with two emitted lines:  $Al - K$  ( $h\nu = 1486.6$  eV) or  $Mg - K$  ( $h\nu = 1253.6$  eV). To obtain photoelectrons energy spectrum, hemispherical energy analyser is used in combination with 5 channeltrons as electron-multiplying detectors.

### SPA-LEED

Low Energy Electron Diffraction (LEED) is surface sensitive techniques for structure determination. This technique has been the dominant method to study the structure and morphology of two dimensional plane surfaces. The system installed in the analytic part of MODA is a commercial Omicron Spot Profile Analysis LEED instrument, a special type of LEED instrument that is able to record and analyze electron diffraction spots in finer detail due to the special electronic parts and geometry of the instrument.

In LEED technique, a beam of low energy electrons is directed perpendicular to the surface (parallel to the surface normal) and, interacting with the 2D periodic structure of the surface, electron diffraction takes place. Since electrons have wavelengths of few  $\text{\AA}$ , they are capable of interacting with surface lattice (that is of few  $\text{\AA}$  order) and also they are in an energy range in which penetration depth is of few atomic layers of the sample ( $nm$  range) making the technique highly surface sensitive. The diffracted electrons are projected into the phosphor screen revealing the 2D diffraction pattern of the surface.

In the case of SPA-LEED, electron-optics system of electrodes is able to scan this pattern by deflecting an electron with certain  $k_x$  and  $k_y$  coordinates

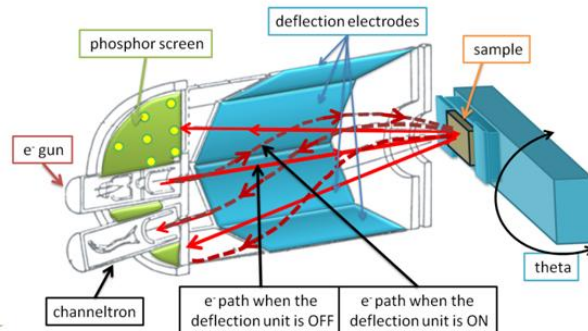


Figure 1.9: Schematic diagram of OMICRON Nanotechnology GmbH SPA-LEED installed on MODA system

onto the fixed channeltron detector, making it possible to do the fine scan of the spot structures in the diffraction pattern. The spot structure carries information not only on the 2D lattice configuration but also about the surface morphology.

### 1.2.3 Omicron VT-AFM Variable Temperature Atomic Force Microscope

The STM system used to obtain STM and STS data in this thesis is a variable temperature ultra high vacuum scanning probe microscope produced by Omicron nanotechnology GmbH (VT-SPM). In our implementation the device is operating at room temperature. The Omicron VT-AFM can be divided into several parts:

- STM/AFM UHV stage
- Preamplifier electronics
- MATRIX system control rack
- PC with MATRIX software for operating MATRIX electronics

The schematic dependence between these parts is shown in figure 1.10:

#### VT-AFM stage and UHV chamber

The schematics of the interior of the device are presented in figure 1.11. Since it is a part of the larger system, there are transfer rods and a carousel stage are

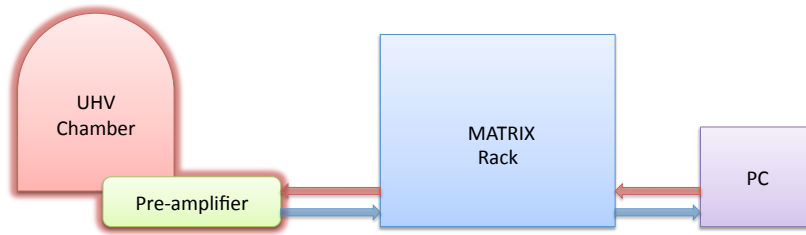


Figure 1.10: Block diagram of Omicron VT-AFM

visible. The presence of the carousel enables stacking up to 12 sample and tip holders making it easy to quickly change either the sample or the tip (technique). To move the holders inside the UHV chamber a wobble stick is used.

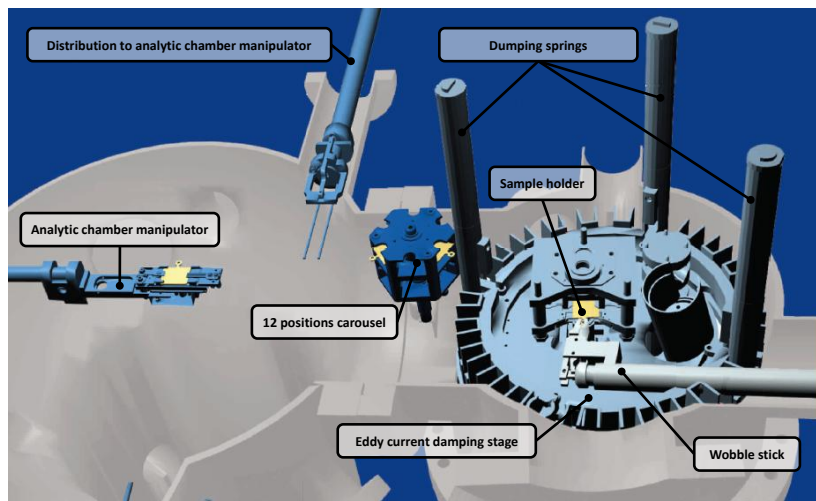


Figure 1.11: 3D model of the Omicron VT-SPM

The whole device is mounted on a stage with a copper frame that can be mechanically decoupled from the rest of the system by means of an eddy current damping stage. During the process of sample and tip exchange, the stage is blocked so that no damage of the damping system can be done. Once experiment has to start, the stage is released and levitates on springs in magnetic field as described in 1.1.4.

### Preamplifier stage

From the electronics side point of view, the pre-amplifier stage strongly determines the operation limit of the STM device since it is the first amplification stage for the tunneling current signal. As mentioned, it is important to have this first stage as close as possible to the signal source. In the case of our device, an SPM PRE 4 amplifier is used with the I/V converter (the first and most important part of pre-amplifier stage) built inside the UHV chamber close to the STM head. It is important to notice that in this system it is the tip that is virtually biased at the  $V_{BIAS}$ , while the sample is kept grounded. However, following the convention mentioned in chapter 1.1.1, all the results in this theses will refer to the bias voltage as to the voltage applied to the surface and all the measurements will be presented in this manner.

There are two possible amplification regimes:

- 300 nA range has the  $3 \cdot 10^9$  V/A linearity constant and the dynamic range of 80 kHz if no additional filtering is selected and 3 kHz with enabled low pass filter for better signal to noise ratio.
- 3 nA range has  $3 \cdot 10^{11}$  V/A linearity constant and the dynamic range of 800 Hz if no additional filtering is selected and 200 Hz with enabled low pass filter for better signal to noise ratio. With low-pass filter applied in this range (200 Hz) the noise is of the 50 fA order, making it possible to obtain tunneling conditions and measurements in sub-picoampere range. We routinely made measurements with 250 fA set point in this configuration.

Although 3 nA offers much better sensitivity and is more suitable for the investigation of semiconducting or even insulating materials, the very low bandwidth limits it's usefulness for the lock-in based STS measurements at room temperature (see chapter 1.3.2).

As an example, in the best case scenario, working at 800 Hz modulation frequency ( $\tau_{OSC}=1.3$  ms oscillation period) and the acquisition period ( $\tau_{AQ}$  integration time of the preamplifier) of 5 times the oscillation period ( $\tau_{AQ} = 5 * \tau_{OSC}$ ) 6 ms are necessary for acquiring a single point lock-in signal. For typical 256 px x 64 px image with 101 px spectra at each point, the acquisition time can be estimated to be around 3 h. This value is not very critical for a room temperature measurement, but in practical implementation much lower frequencies had to be used because very strong crosstalk is present when working with small currents in the picoampere range, and the use of low-pass filter is needed to increase the signal to noise ratio. Usual, times for the acquisition can than be orders of magnitude higher due to prolonged

integration times, making any high energy or spatial resolution measurements impossible at room temperature. To use the power of high sensitivity the numerical approach to get STS is needed as described in chapter 2.1.

### MATRIX control system

MATRIX SPM control system is a fully digital control system with separate digital boards within the MATRIX control housing, tailored for different tasks within the experimental routine. Measurement routines are distributed among these boards.

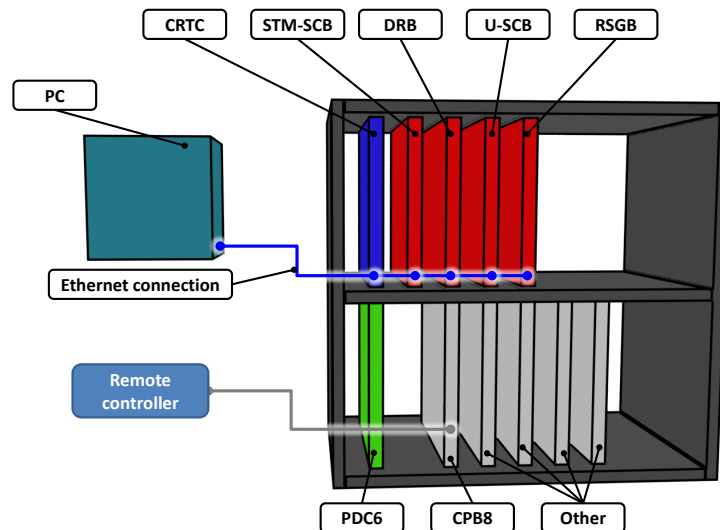


Figure 1.12: Schematics of MATRIX system architecture for the basic STM experiment

As shown in figure 1.12 there is one master board, called Central Real-Time Controller, that controls all the other function specific boards in the rack over PCI bus. The basic STM configuration includes 4 slave boards with different functions as follows:

- STM-SCB - Scanning tunneling Microscopy - Signal Conversion Board is responsible for providing bias to the tip and for measuring and converting tunneling current signal. It is the MATRIX interface to the pre-amplifier stage.
- DRB - Digital Regulator Board - main function of this board is to provide the feedback signal to the Z piezoelectric and additionally in-

## 1. Scanning Tunneling Microscopy

---

roduces two input channels AUX1 and AUX2 that can be used for measuring optional signals (like for example the output of the lock-in)

- U-SCB - Universal Signal Conversion Board is used if AFM is implemented (like it is in our case) for acquiring additional signals (dumping, frequency difference,...)
- RSGB - Raster Scan Generator Board is responsible for generating reference voltages for lateral scanner movement

Basic STM implementation also requires one driver, 6 channels, Piezo Driver Board - PDC6 , that amplifies the signals obtain from DRB and RSGB so that they can be used for driving Z and X/Y piezo-motors respectively and a Coarse positioning Board - CPB8, that is responsible for a coarse approach of the tip stage to the sample one.

If AFM or other SPM techniques are implemented, additional function specific boards can be also included.

Communications between the host PC and the control electronics is based on Ethernet connection. The host PC acts as user interface for definition of experiments and measurement parameters, the measurement routine, however, runs fully independent from PC hardware.

### **PC control and analysis software**

To control the MATRIX system, any PC with Ethernet port can be used, provided that it has MATRIX software installed. The software has modular organization in accordance with the hardware design. During the experiment, only the required software modules are activated and additional freedom to activate or deactivate certain acquisitions and controls is given to the user.

To analyze experimentally obtained data, a commercial Image Metrology Scanning Probe Image Processor - SPIP<sup>TM</sup> is provided. Although equipped with useful routines, there are a lot of limitation of SPIP<sup>TM</sup> especially when working with spectroscopic data. For the purpose of post acquisition analysis, apart from SPIP<sup>TM</sup>, the MathWorks<sup>TM</sup> software MATLAB<sup>®</sup> software package is also used. MATLAB<sup>®</sup> is especially useful because it provides easy manipulation with matrix organized data and also provides multi-thread support that significantly speeds up the numerical calculation on large data sets, as is the case in the STS map experiments. More on SPIP<sup>TM</sup> and MATLAB<sup>®</sup> utilization will be said in the chapter 2.

### 1.2.4 STM and AFM tip preparation

To obtain good STM/STS measurements it is of great importance to have atomically sharp tips. In our measurements two type of wires are used: Ir and Pt/Ir. To prepare them for the experiment, an electrochemical etching in  $CaCl_2 + HCl + H_2O$  solution is used. Although optimized for preparation of Ir tips, it also give good results with Pt/Ir alloy. After the etching the tip is gently rinsed in ethanol and checked with the optical microscope for the sharpness. It is then mounted on the Omicron tip holder (fig . 1.13 ) by clamping the wire inside the holder tube. Electrical contact between the tip wire and the corresponding tip holder pin is checked and if everything is regular it is than introduced into the UHV system.



Figure 1.13: Omicron VT-AFM STM (left) and AFM(right)tip holder

Mounting of the AFM tips is very delicate process, since one has to make sure that the position of the tip, that is placed at the top of the cantilever, is aligned with the AFM infrared laser optical path. To be able to do so a mounting device with marked, desired position of the tip is supplied by Omicron.

Once the AFM chip is placed on the device the tip position is made to match the marked one by applying small adjustments of the AFM chip position with the help of optical microscope. When in place, a UHV epoxy is applied, securing the AFM chip position in respect to the AFM tip holder. After a curing procedure, that in our case means baking the whole mounting stage to  $150^{\circ}$  C for 1 hour, the position of the AFM tip in respect to the desired one should be checked again due to the possible thermally induced movements. In the case of non-contact AFM and conductive contact AFM tips, another step is needed. It is necessary to apply the conducting UHV epoxy between the conducting lower side of the AFM chip and the one of the AFM tip holder pins. Once conductive epoxy is applied, a short curing procedure is needed. Finally the AFM tip holder is introduced into the UHV system after assuring that all electrical contacts on AFM tip holder are good.

## 1.3 SPM modes

### 1.3.1 STM - Topography

When measuring topographic images with scanning tunneling microscopy, there are two working regimes:

- Constant current mode
- Constant height mode

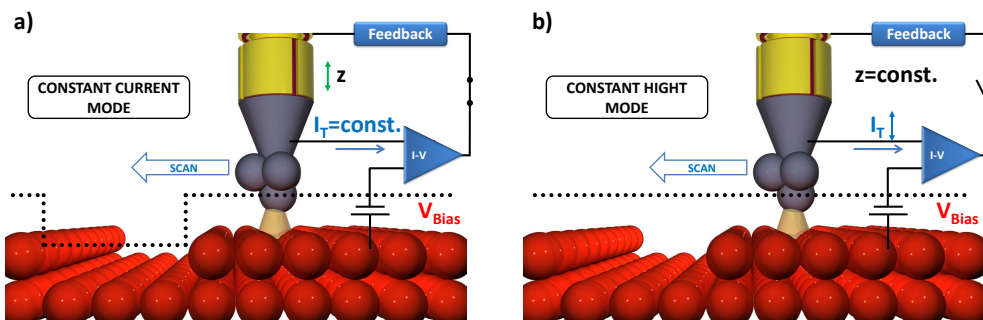


Figure 1.14: Two operational modes of STM a) constant current mode b) constant height mode

The constant current regime is the one already described as the principal working STM regime. The feedback is regulating the  $z$ -piezo elongation in order to maintain the constant tunneling current or more generally constant barrier width (tip to sample separation). This is the safest mode of STM operations, since the feedback mechanism is regulating the tip position, preventing eventual crash with the surface.

When talking about constant height mode, one should notice that it is the absolute position (height) of the point probe that is maintained constant and not the tip to sample separation (barrier width). To be more precise it is the elongation of the  $z$ -piezo motor that is maintained constant or even, more precisely, it is the  $V_{\text{PIEZO}}$ , a voltage applied to the  $z$ -motor. that is kept constant. To be able to work in this mode, one has to be certain that in the whole spatial range to be scanned, the roughness and the sample tilt are such that there is no interaction between the tip and the sample, in other words only atomically flat surfaces and usually very small lateral scanning limits (few nanometers). This is usually achieved by first acquiring the topographic

image in constant current mode and if previous conditions are fulfilled, the feedback is disabled and measurement is done in constant height mode.

Since there is no  $z$ -movement of the piezo, the information about surface topography as well as the surface electronic states is contained in the tunneling current image. The interpretation of the obtained data is not as straightforward as it is in the constant current case.

### 1.3.2 STM - Spectroscopy

Spectroscopic regime of the STM means that at certain moment the regularization of the tunneling barrier width is turned off, a voltage ramp is then applied to the sample or the tip and the tunneling current or the differential conductivity dependence as a function of the applied bias voltage is measured. In this way it is possible to directly and locally probe the electronic properties of the surface not only at the voltages where the tunneling is easily achieved, but also in the range of energies close to the Fermi level or in the gap of the semiconducting materials, where tunneling conditions, in general, could not be established.

As mentioned earlier,  $dI/dV$  is proportional to the local density of states of the sample at the lateral tip position. Although the  $I(V)$  spectra has in itself the information in the total conductivity  $dI/dV$ , the numerical differentiation is not straightforward, as will be shown in the next chapter. Therefore, whenever possible, the lock-in technique is implemented to directly obtain the  $dI/dV$  curve during the STS measurements.

In the lock-in based STS measurement of  $dI/dV$ , the bias voltage  $V_{BIAS} = V_{DC}$  is modulated by a small amplitude signal as shown in Eq. 1.15:

$$V_{BIAS} = V_{DC} + V_{AC}^0 \sin(2\pi ft + \phi_1) \quad (1.15)$$

The values of modulation amplitude  $V_{AC}^0$ , frequency  $f$  and phase  $\phi_1$  are regulated by the lock-in amplifier. As a result, also the tunneling current will be modulated as shown in Fig. 1.15.

If the feedback is applied and the modulation is slow enough, the feedback will compensate the bias change and will keep the tunneling resistance  $R_T$  constant. If, on the other hand, the feedback is disabled and the oscillations have small enough amplitude, the current will follow the modulation of the bias having the same harmonic component at frequency  $f$ . The small amplitude assumption is needed to secure that the oscillation will occur in a linear manner, with the linearity coefficient equal to differential conductance of  $dI(V)/dV$  at the  $V_{BIAS}$ . If the linearity condition is fulfilled, one can also measure the phase change  $\Delta\phi = \Delta\phi_2 - \Delta\phi_1$ . The role of the lock-in amplifier

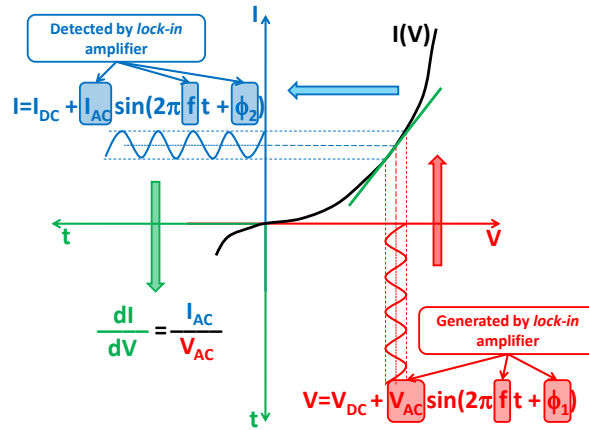


Figure 1.15: The measurement of differential conductance by *lock-in* technique

is to measure and to amplify the amplitude of the current at the modulation frequency during the spectroscopic measurements, which is proportional to the conductance  $dI/dV$ .

### 1.3.3 AFM - Topography

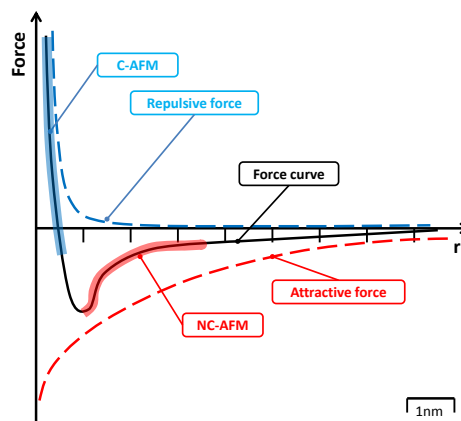


Figure 1.16: The force-distance curve between the tip and the sample material in atomic force microscopy measurements.

Apart the STM mode, the Omicron VT-SPM system allow atomic force microscopy (AFM) measurements. In the AFM based techniques, the tip is

placed at the end of a cantilever and brought in the close proximity of the sample material. If close enough, inter-atomic forces arise between the tip atoms and the sample atoms, as shown in figure 1.16. Depending on the tip-sample distance, these forces can be attractive or repulsive. There are two AFM modes of operation implemented:

- Contact atomic force microscopy C-AFM
- Non-contact atomic force microscopy NC-AFM

### Contact AFM

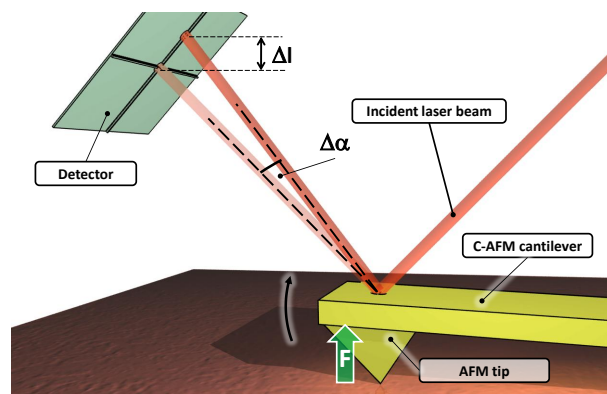


Figure 1.17: Contact AFM functioning principle

In contact AFM mode the tip to sample distance is such that a strong repulsive force comes into action (tip and sample are in contact). This repulsive force, of order of nano-Newton, bends the cantilever. The bending is detected by means of laser light beam deflection. A constant force, corresponding to a stable tip to sample interaction, is maintained by the feedback mechanism that uses as input signal the bending of the cantilever (equivalently the force or the light deflection) measured by the deflection of a laser beam impinging on the cantilever and reflected toward a four quadrant detector. Hence, by lateral scanning the tip it is possible to obtain topographic images of the investigated surface.

The advantage of the AFM respect STM is that the sample surface can be also insulating. Disadvantages lie in somewhat lower resolution and the complexity of the implementation.

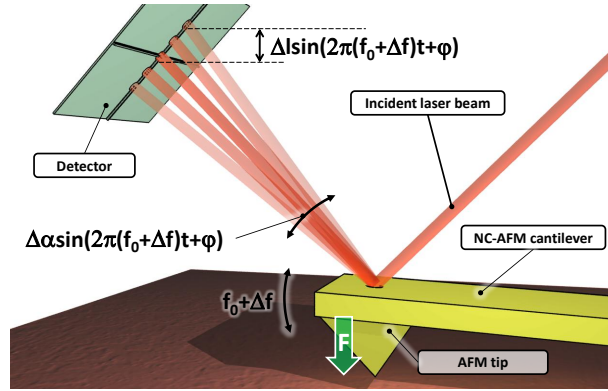


Figure 1.18: Non contact AFM functioning principle

### Non-contact AFM

In non-contact AFM mode, the cantilever is forced to oscillate with a given amplitude at its resonant frequency  $f_0$ . A separate feedback maintains the amplitude of the oscillation  $A_0$  fixed, while the signal used to establish the measurement conditions, is the frequency shift, which depends on the tip to sample interaction and therefore on the average distance. The latter depends on the material of which composing the tip (it's Young elasticity modulus-  $E_Y$ ) and by its geometry. Once the tip is close enough to the sample and attractive forces start acting on the tip, the oscillating conditions changes, having for a consequence a change of the resonant frequency. In the case of our device, the feedback regulation system is maintaining constant the frequency difference  $df$ . This is the difference between initial resonant frequency and resonant frequency of the cantilever at small tip-sample separation. Similar to C-AFM, by lateral scanning and maintaining  $df$  constant one can obtain topographic image of the surface investigated.

# Chapter 2

## Numerical methods

In this chapter the numerical methods implemented to analyze experimental data are discussed in details. As mentioned earlier, the output of the STS map experiment is a set of  $I(V)$  curves or set of both  $I(V)$  and experimental  $dI/dV$  curves obtained by the *lock-in* technique. In the former case, the first challenge is to obtain numerically the  $dI/dV$  curve from the  $I(V)$  curve.

Once differential conductance is determined, an implementation of the normalization procedure to get a quantity proportional to the local density of states (LDOS) is needed, unless the STS spectra are measured in a region very close the Fermi level. In all the other cases, one has to take into account the fact that assumption of bias invariant tunneling probability is not valid, as it is in all the STS measurements presented in this thesis. Unfortunately, there are no numerical methods for the normalization, proposed in the literature, that can be considered both quantitative and experimentally feasible. However the normalization process itself does improve LDOS recovery from the measured data.

Finally, the amount of data obtained during STS spectroscopic map usually consists of tens of thousands of spectra that need to be analyzed. Classifying the spectra can be done by parameters connected with the existence of certain reproducible features (gap width, coherence peaks), but in cases where such features are absent, or not obvious, classification represents a non trivial problem. An unbiased, K-means classification algorithm is discussed in this frame.

## 2.1 Differentiating noisy curves- total variation regularization

Spectroscopic imaging measurements done at room temperature are very sensitive to temperature stability. Lock-in approach enables simultaneous measurement of both current-voltage ( $I(V)$ ) and differential conductance ( $dI/dV$ ). There are several drawbacks of this approach that limit or disables its application when obtaining STS maps. Depending on a pre-amplifier regime, the bandwidth of the pre-amplifier stage limits the speed of lock-in by introducing long integration times and thus making the single point and overall measurement slow enough for the thermal drift to influence the STS map acquisition. This speed limit can be overcome either by stabilizing the temperature or by sacrificing the energy resolution of the STS spectra. Even when speed condition is not a problem, there is a possibility of crosstalk between the modulating signal and the pre-amplifier stage in cases of high gain and very small measured currents, close to the sensitivity limit of the pre-amplifier. This is especially the case when insulating surfaces and buried interfaces are observed. The solution to obtain differential tunneling conductance in this case lies in application of post-acquisition numerical calculation of the  $dI/dV$  from the obtained  $I(V)$  data at each point.

One of the main challenges in numerical calculation of differential tunneling conductance approach is the differentiation of noisy data obtained during the scanning tunneling spectroscopy measurements. Since the quick acquisition of  $I(V)$  spectra is of interest, the acquisition time per single  $I(V)$  point are short thus leading to noisy data.

To address this problem there are several possible approaches. Classical finite-difference approximations amplify greatly any noise present in the data. Data de-noising, before or after differentiating, does not generally give satisfactory results. A method that leads to good results consists in the regularization of the differentiation process itself.

A common framework for the regularization corresponds to the formulation of the inverse problem [5, 6]. An inverse problem is the task that often occurs in many branches of science and mathematics where the values of some model parameter(s) must be obtained from the observed data. In this respect  $u(x)$ , the differentiation of an observed (measured) function  $f(x)$  on an interval  $x \in [0, L]$ , is the minimizer of the functional given by equation 2.1:

$$\begin{aligned}
 F(u) &= \alpha R \{u(x)\} + DS \{A[u(x)] - f(x)\} \\
 A[u(x)] &= \int_0^x u(x) dx
 \end{aligned}
 \tag{2.1}$$

This is the most general form of the functional  $F(u)$  consisting of two parts: regularization part that penalizes the irregularities ( $R \{u(x)\}$ ) and a data similarity term that penalizes discrepancy between  $A[u(x)]$  (the operator of anti-differentiation acting on  $u(x)$ ) and  $f(x)$  ( $DS \{A[u(x)] - f\}$ ). The  $\alpha$  parameter is a regularization parameter that controls the balance between the two terms ( $\alpha \in \mathfrak{R}^+$ ). The choice of the regularization operator in the form of squared  $L^2$  norm (Eq. 2.2) is a common choice but as a consequence the minimizer (derivative) is forced to be continuous, making this choice inappropriate for the functions that have singular points.

$$R \{u(x)\} = \int_0^L |u(x)'|^2 dx
 \tag{2.2}$$

More robust choice for the regularization term is total regularization norm (Eq. 2.3) as proposed by Chartrand [5]:

$$R \{u(x)\} = \int_0^L |u(x)'| dx
 \tag{2.3}$$

With this choice of  $R \{u(x)\}$  and  $DS \{A[u(x)] - f\}$  the functional to be minimized obtains the form (Eq. 2.4):

$$F(u) = \alpha \int_0^L |u(x)'| dx + \int_0^L |Au - f|^2 dx
 \tag{2.4}$$

To find the minimizer of the functional mentioned above the lagged diffusivity method of Vogel and Oman [7] was used, with numerical implementation algorithm proposed by Chatrand [5] and Vogel [8].

In our case the observed data  $\mathbf{f}$  is the measured spectroscopic function ( $I(V)$  or  $\ln |I(V)|$ ) on  $\mathbf{x}$  and the  $\mathbf{u}$  is corresponding numerical derivative ( $dI(V)/dV$  or  $d \ln |I(V)|/dV$ ). Without breaking of generality we can assume that  $f_0 = 0$  and  $x_0 = 0$  (Eq. 2.5):

$$\mathbf{x} = \mathbf{V} = \begin{bmatrix} V_0 \\ V_1 \\ \vdots \\ V_{N_V-1} \end{bmatrix} = \begin{bmatrix} 0 \\ \Delta x \\ \vdots \\ (N_V - 1)\Delta x \end{bmatrix}_{N_V \times 1} ; \mathbf{f} = \begin{bmatrix} f_0 = 0 \\ f_1 \\ \vdots \\ f_{N_V} \end{bmatrix}_{N_V \times 1}
 \tag{2.5}$$

## 2. Numerical methods

---

The differentiation operator in the case of numeric function is the matrix  $\mathbf{D}$ . When differentiating  $\mathbf{f}$  with respect to  $\mathbf{x}$  the  $\mathbf{D}^f$  has the form (Eq. 2.6) :

$$\mathbf{D}^f = \frac{1}{\Delta x} \begin{bmatrix} -1 & 1 & 0 & \cdots & 0 \\ 0 & -1 & 1 & \cdots & 0 \\ & & \vdots & \ddots & \vdots \\ 0 & 0 & 0 & \cdots & 1 \end{bmatrix}_{(N_V-1) \times N_V} \quad (2.6)$$

In the first iteration the non-regularized derivative  $\mathbf{u}^0$  is given by Eq. 2.7:

$$\mathbf{u}^0 = \mathbf{D}^f \mathbf{f} = \begin{bmatrix} u_1 \\ u_2 \\ \vdots \\ u_{N_V-1} \end{bmatrix}_{(N_V-1) \times 1} \quad (2.7)$$

For the process of regularization several matrix operators have to be constructed. The first two are differentiation operator and anti-differentiation operator that act on  $\mathbf{u}$  and producing it's derivative and it's integral, respectively:

$$\mathbf{D} = \frac{1}{\Delta x} \begin{bmatrix} -1 & 1 & 0 & \cdots & 0 \\ 0 & -1 & 1 & \cdots & 0 \\ & & \vdots & \ddots & \vdots \\ 0 & 0 & 0 & \cdots & 1 \end{bmatrix}_{(N_V-2) \times (N_V-1)} \quad (2.8)$$

$$\mathbf{K} = \Delta x \begin{bmatrix} 0.5 & 0 & 0 & \cdots & 0 \\ 1 & 0.5 & 0 & \cdots & 0 \\ & & \vdots & \ddots & \vdots \\ 1 & 1 & 1 & \cdots & 0.5 \end{bmatrix}_{(N_V-1) \times (N_V-1)}$$

This two operators does not change during iterative lagged diffusivity regularization method. For each iteration based on the previously obtained  $\mathbf{u}^i$  (where  $i$  is the iteration step  $i \geq 0; i \in N_0$ ) we define next matrix operators:

$$\mathbf{E}^i = \begin{bmatrix} E_1 & 0 & 0 & \cdots & 0 \\ 0 & E_2 & 0 & \cdots & 0 \\ & \vdots & & \ddots & \vdots \\ 0 & 0 & 0 & \cdots & E_{N_V-2} \end{bmatrix}_{(N_V-2) \times (N_V-2)} \quad ; \quad E_n^i = \frac{1}{\sqrt{(u_n^i - u_{n-1}^i)^2 + \epsilon}}$$

$$\begin{aligned} \mathbf{L}_{(N_V-1) \times (N_V-1)}^i &= \Delta x \mathbf{D}^T \mathbf{E}^i \mathbf{D}; \\ \mathbf{H}_{(N_V-1) \times (N_V-1)}^i &= \mathbf{K}^T \mathbf{K} + \alpha \mathbf{L}^i; \\ \mathbf{g}_{(N_V-1) \times 1}^i &= \mathbf{K}^T (\mathbf{K} \mathbf{u}^i - \mathbf{f}) + \alpha \mathbf{L}^i \mathbf{u}^i; \end{aligned} \quad (2.9)$$

The idea of the regularization process is to update the existing  $\mathbf{u}^i$  with  $\mathbf{s}^i$  in each iteration to obtain new  $\mathbf{u}^{i+1}$  that produces lower value of  $F(u)$  functional. Having above defined matrix operators, one can calculate the update  $\mathbf{s}^i$  according to lagged diffusivity regularization method using the formula:

$$\begin{aligned} \mathbf{H}^i \mathbf{s}^i &= -\mathbf{g}^i \\ \mathbf{s}^i &= -\mathbf{H}^{i-1} \mathbf{g}^i \end{aligned} \quad (2.10)$$

so that finally:

$$\mathbf{u}^{i+1} = \mathbf{u}^i - \mathbf{H}^{i-1} \mathbf{g}^i \quad (2.11)$$

This method is proven to converge to the minimizer of  $F(u)$  giving a solution for derivative of  $f$ . The regularization parameter  $\alpha$  was chosen as the mean squared difference between  $f$  and the smoothed value of  $f$ .

### 2.1.1 Numerical example

In this section the benefits of TVR differentiating method over smoothing will be demonstrated on example of known function superimposed with noise of normal distribution with different standard variations  $\sigma$ .

The starting curve has a gap like shape with different onset slopes at negative and positive side (red curve in figure 2.1 a) and b)). The normal noise is added with two different standard variations  $\sigma_1 = 0.1$  and  $\sigma_2 = 0.5$  presented as blue curve (star markers) in the figure 2.1 a) and b) respectively. The numerical values are sampled equidistantly with resolution of 0.01V in both cases. For the sake of comparison between TVR differentiating method and smoothing and finite differences differentiation method a smoothed curves were also presented - green curves with + markers in figure 2.1 a) and b).

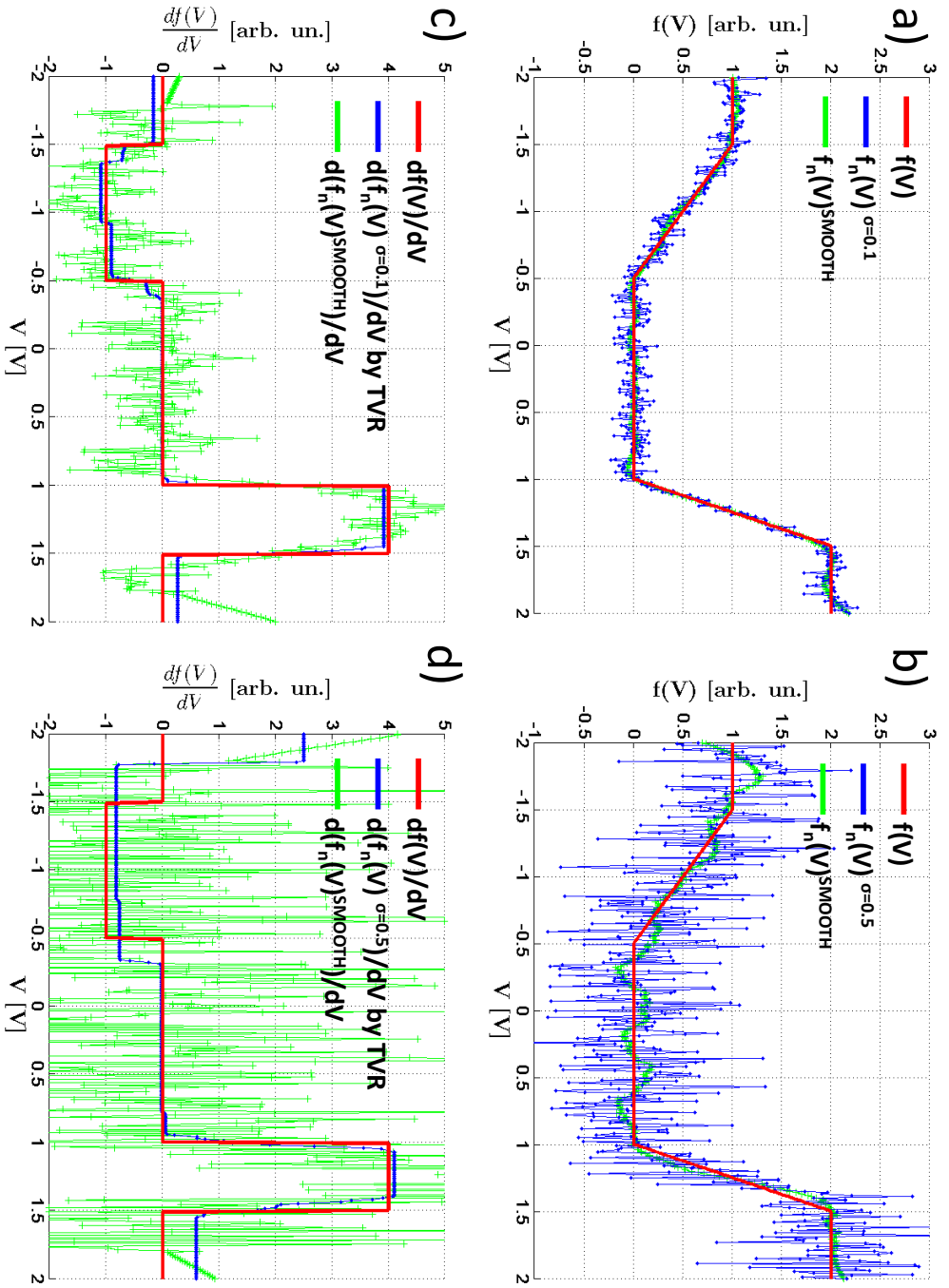


Figure 2.1: The comparison of TVR differentiation method to finite differences differentiation of smoothing curve method as a function of present noise

Smoothing is done by binomial Savitzky-Golay filter with 41 point span (41 point corresponds to 0.41V in this case).

The results of deriving each of this curves is presented in figure 2.1 c) and d). In both cases TVR gives much better results than a smoothing method and apart from being less noisy, it reproduces all the features present in the derivative of original function. The question of quantitative goodness of the derivative can be raised, but it is clear that even from this point of few TVR is in better agreement with the original data.

### 2.1.2 TVR applied on experimental curves: example

Here is presented an application of TVR on spectroscopic data obtained in course of this thesis.

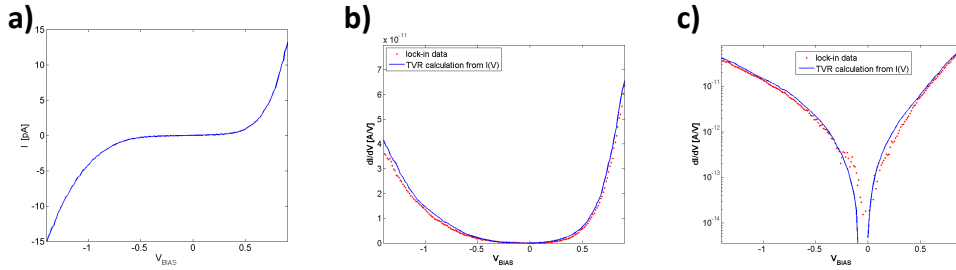


Figure 2.2: a) average  $I(V)$  curve of the spectral set; b-c)  $dI/dV(V)$  obtained with lock-in (red marks) and TVR (blue line) were obtained for each curve in spectra set separately, and the average on whole set is shown in linear (b) and log scale (c)

First, the TVR obtained differential conductance to that obtained while implementing lock-in technique are compared. In figure 2.2  $I(V)$  curve (blue) and  $dI/dV(V)$  curves obtained with TVR (blue line) and by applying lock-in-technique (red marks) are shown. As seen from the log-scaled curve, the match is very good and only slightly differs in the band region, probably due to the enhanced noise levels compared to that of the signal.

We also present here the comparison between  $dI/dV(V)$  curves numerically obtained by TVR and commercially available program for scanning probe image processing - SPIP. We compare this two numerical methods when applied on a single spectral curve as well as on the average on all spectroscopic set. The comparison between the single curves clearly favors TVR since the level of noise in SPIP image completely screens the  $dI/dV(V)$  form. When observing effect on the average  $dI/dV(V)$  curve, SPIP data still

## 2. Numerical methods

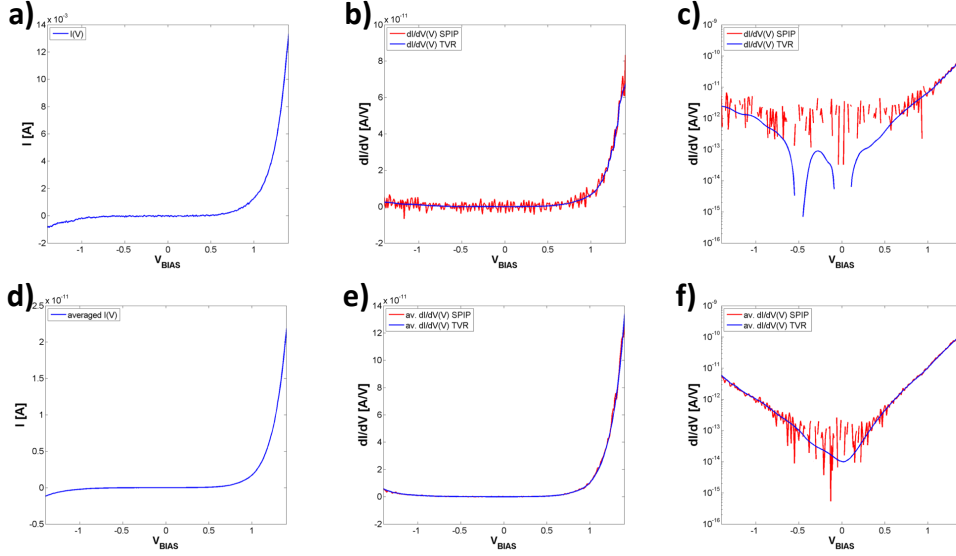


Figure 2.3: Calculation of a single  $I(V)$  curve differential (a) by TVR (blue) and SPIP (red) and average of single  $I(V)$  curves differentials calculated by TVR (blue) and SPIP (red) (c,d,e)

possesses the noise but much less pronounced due to the averaging. Nevertheless as seen on an average spectra TVR and SPIP are similar in form, but the SPIP one is noisier, thus we favor TVR when dealing with our data. One should notice that in neither case we used any kind of smoothing algorithm.

## 2.2 Normalization of differential tunneling conductance

Starting from the equation for the tunneling current and the approximation considered (see eq. 1.9 in ch. 1.1.1) it is obvious that the correlation between differential conductance and the local density of states is generally valid only at small bias voltages around the Fermi level (and more generally only at the temperatures close to 0 K). By biasing either the tip or the sample with voltages comparable to the values of work function potential, the induced electric field significantly changes the shape of the potential barrier between the tip and the sample electrode, having as consequence change (increase) of the tunneling probability matrix element. When inspecting the local density of states on conductors and superconductors around Fermi level, this change is of no significant importance since the examined energies are in the

mV range. Dealing with semiconducting or insulating materials, one with the Fermi level inside the eV wide band gap, the role of the tunneling matrix coefficient increase and has to be taken into account. This is done by normalizing the measured or calculated differential conductivity. There are several ways to approach normalization. One is to use the current-voltage  $I(V)$  characteristic at higher bias voltages (energies) as a measure of  $T(V)$  and the other, more analytical approach proposed by Ukraintsev [9] is to estimate the  $T(V)$  by fitting proposed analytical model to the measured differential conductance hence obtaining the value for  $T(V)$  to be used in normalization process. The normalized curves, however, are not yet suitable for a direct quantitative analysis in order to recover the true LDOS.

### 2.2.1 Total conductivity normalization

The total conductivity normalization is the simplest method to be implemented and very often used as method of normalization. The idea behind this normalization, lies in the fact that the total conductivity is a good measure of the tunneling probability dependence with the applied voltage. The normalized conductance obtained by dividing measured or calculated differential conductance  $dI/dV$ , at certain bias voltage (energy)  $V$ , by the corresponding total conductance at the same energies,  $I/V$  (Eq. 2.12) is:

$$NDC_{TCN} = \frac{\frac{dI}{dV}}{\frac{I}{V}} \quad (2.12)$$

Regardless of the sample type (metal, semiconductor, superconductor.. ) there is a problem of singularity of  $NDC_{TCN}$  at Fermi level that is always present. This can easily be avoided in the case of metallic samples by not including the Fermi level in the calculation. The problem still remains though in the presence of gap in the spectra, where currents are very small (or zero) in a wide range of bias voltage values around the Fermi level. To overcome this, there are several approaches in calculating  $NDC_{TCN}$ . The first one is to add a certain relatively small constant  $\epsilon$  to the current in the total conductivity term, eliminating in this way the problematic division by 0 (Eq. 2.13):

$$NDC_{TCN} = \frac{\frac{dI}{dV}}{\frac{|I + \epsilon|}{|V|}} \quad (2.13)$$

The second approach proposed by Mårtensson and Feenstra [10] is to use

broadened version of  $I(V)$  curve done by one-pole Fourier low-pass filtering with the pole frequency given by  $\Delta^{-1}$ , where  $\Delta$  represents the value comparable to the width of the band gap. This makes the resulting broadened  $I(V)$  having non-zero values in the whole range of interest, thus making the normalization possible.

$$NDC_{TCN} = \frac{\frac{dI}{dV}}{\frac{|I_{FILTERED}|}{|V|}} \quad (2.14)$$

The last approach, that gives the best results, easy to implement and not computational demanding, is to calculate normalized conductance as a derivative of  $\ln(I)$  with respect to  $d\ln(V)$  (Eq. 2.15):

$$NDC_{TCN} = \frac{d\ln(I)}{d\ln(V)} \quad (2.15)$$

The practical implementation of this normalization however can be described with the next formula:

$$NDC_{TCN} = V \frac{d\ln(|I| + \epsilon)}{dV} \quad (2.16)$$

Where  $\epsilon$  is a small current value compared to  $I$  (usually in the order of current noise) introduced to eliminate calculation of zero current logarithm.

### 2.2.2 Ukraintsev normalization

The approach of Ukraintsev [9] to the normalization problem is to recover the sample and/or tip DOS, by normalizing the differential conductivity by its fit to the tunneling probability function. To model electron tunneling between the STM tip and the sample, Ukraintsev used one-dimensional and semi-classical WKB approximation. The proposed asymmetric tunneling probability function has the form (Eq. 2.17):

$$F(S, V) = A_T T'(S, eV/2) + A_S T'(S, -eV/2) \quad (2.17)$$

Where  $A_T$  and  $A_S$  represent proportionality coefficients related to the tip-surface effective contact area and proportional to the tip and the sample densities of states at the Fermi level respectively,  $S$  is tip-surface separation,  $V$  is the bias voltage applied on the sample.  $T'(S, eV/2)$  and  $T'(S, -eV/2)$  are probability of tunneling to or from the tip or the sample Fermi level (respectively) and are given by (Eq. 2.18) [9, 11]:

$$T'(S, \xi) = \exp \left[ -2S \left( \frac{2m}{\hbar^2} (\bar{\Phi} - \xi) \right)^{1/2} \right] \quad (2.18)$$

Here  $\bar{\Phi}$  represents the average work function of the tip and the sample. By fitting Eq. 2.17 and 2.18 to the experimentally obtained differential tunneling conductivity ( $dI/dV$ ), two important physical parameters can be extracted: local average work function  $\bar{\Phi}$  and tip sample distance  $S$ . These parameters are used in the proposed fitting of the differential conductivity by the tunneling probability function. Although this method provides a better recovery of LDOS from the experimental data compared to the total conductivity normalization one, it can not be considered a quantitative procedure as noted by Ukraintsev himself [9].

As noted by Koslowski et al. ([12]), the assumption of an asymmetric tunneling probability function in Ukraintsev method is physically difficult to justify and the LDOS may also specifically contribute to the background of a  $dI/dV$ . Consequently he proposed more refined model that takes into account the tip to sample separation experimentally obtained during spectroscopic measurements. Although more quantitative, Koslowski approach requires rather complex approach to STS map measurements requiring acquisition of not only  $dI/dV$  but also of  $dI/dz$  spectra at each spatial point.

Although not suitable for STS map measurement the Ukraintsev normalizations can be useful in a single point spectroscopy measurements.

### 2.2.3 Normalization comparison

Here we'll present the application of normalization procedures on our data. Before comparing them we'll show the influence of small parameter  $\epsilon$  on  $NDC_{TCN}$  and  $NDC_{TCN}$ . as shown in Fig. 2.4 the  $\epsilon$  was varied in a huge range from  $10^{-17}$  A to  $10^{-13}$  A. The influence on  $NDC_{TCN}$  is enormous especially at the onset values where conduction peak is greatly suppressed by decreasing  $\epsilon$ . The effect of  $\epsilon$  is less pronounced in  $NDC_{TCNln}$  indicating that the conducting peak at the onset is algorithm driven rather than real feature. For that reason we'll use  $NDC_{TCNln}$  in the rest of the thesis if not suggested differently.

Finally we compare the proposed normalizations in Fig. 2.5. While  $NDC_{TCN}$  and  $NDC_{TCNln}$  (marked as  $NDC_{ln}$  at the image ) are comparable and are almost identical. The  $NDC_{SMOOTH}$  obtained by normalizing the  $I(V)$  characteristic by total conductance based on smoothed version of  $I(V)$  curve, although showing a similar gap value, differs from the previous curves but exhibits an artificial singularity at zero indicating either that there is an small offset in the  $I(V)$  curve or that the smoothing is not sufficient. In either

## 2. Numerical methods

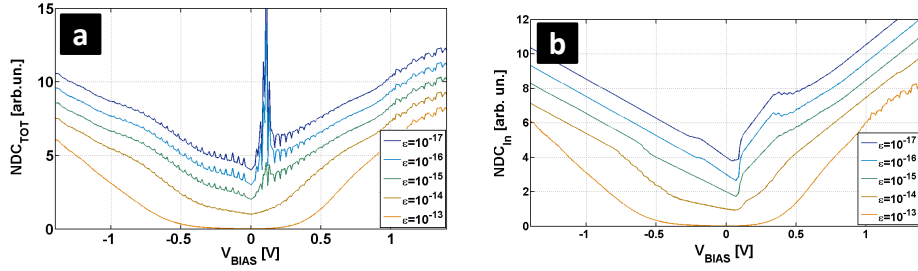


Figure 2.4: Influence of small parameter  $\epsilon$  on NDC curves a) Total conductance normalization b)  $d\ln I/d\ln V$  normalization

case it would require significant change of smoothing parameter without any physical justification.

The Ukraintsev normalization is very different from each total conductance based normalization, at least in regions of high bias voltage. Although predicted to give better estimation of LDOS curves, the method are qualitative, and due to demanding calculation time needed for Ukraintsev normalization, and the fact that it is not as used in publication as TCN, in this thesis Ukraintsev normalization will be used only to extract some interesting parameters from the fitted data, rather than used as the normalization method of choice.

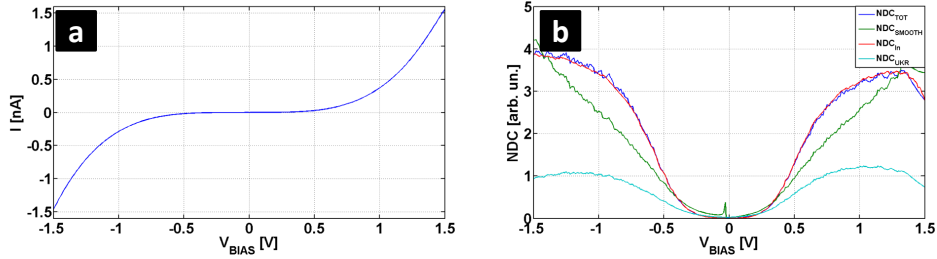


Figure 2.5: a)  $I(V)$  characteristic (obtained by averaging a spectroscopic set) and b) different normalization done for the optimized parameters ( $\epsilon$  being of the order of noise current )

## 2.3 K-means classification method

One of the challenges when analyzing the spectroscopic map data, is the classification of obtained spectra by certain criteria. In the case of spectroscopic maps, the number of obtained spectra is huge and corresponds to the overall number of image points (pixels) and is usually in a range of tens of

thousands. If there is a known feature in the spectra (a coherent peak, a gap, asymmetry parameter...), one of the possible approaches is to quantify these features in post-acquisition process for each spectra and use it as a classification parameter.

A more general and unbiased approach, in some way, is to classify the spectra into classes by comparing them in the whole (or partial) range of energy values and, by introducing certain distance, divide them in several classes. This approach is more general and unbiased than the parameter classification methods (although by selecting certain energy windows in STS data to be used in classification one can bias the process). One of such unbiased techniques is the K-means clustering algorithm. It is commonly used in computer vision as a form of image segmentation resulting in border detection and object recognition.

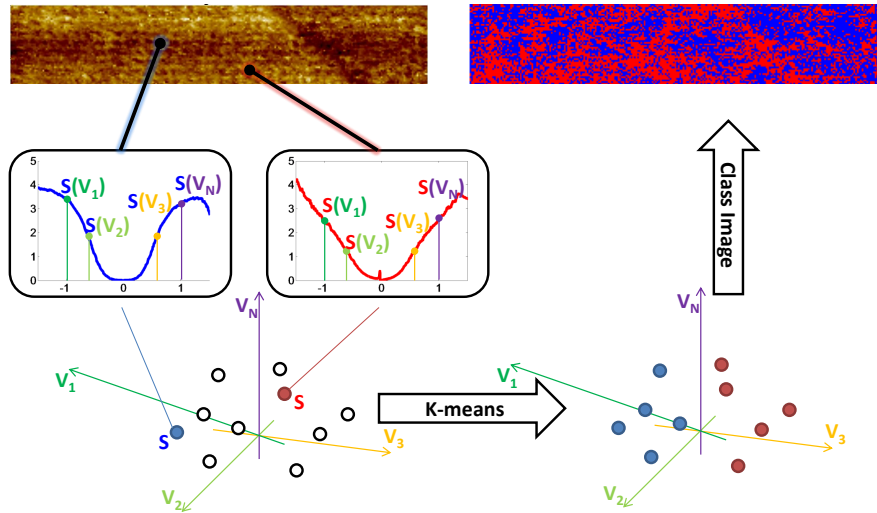


Figure 2.6: The schematic diagram of the application of the K-means algorithm on STS data.

Before formal language is introduced to describe the K-means algorithm, here it is shown how it applies on the STS map measurements. As seen in Fig. 2.6, when doing STS mapping to each spatial point in the topographic image corresponds a spectral curve. The origin of this curve is, from the point of view of the algorithm, not important; it can be  $I(V)$  curve itself or differential conductance curve or normalized differential conductance. The important thing is that the values of voltages (energy) at which they are obtained, are the same for each curve (indicated as  $V_1, V_2, V_3$  and  $V_N$  on the figure 2.6); also the sampling points at which the spectra are obtained do not have to be equidistant. What K-means algorithm does is to consider each

sampling point as an axis and a value that spectra have in that sampling point as a coordinate on that axis ( $S(V_1), S(V_2), S(V_3)$  and  $S(V_N)$ ). In this frame single spectrum is mapped into a single point in this hyperspace (blue, red and black dots). What K-means do is to just separate this points into K classes by using the criteria of distance between them (in analogy with euclidean space). The classes are than mapped back into real space image, giving the distribution of spectra by classes they belong. Later the two dimensional example will be introduced to clarify more the classification process. In the frame of formal language that follows, spectra are observations  $\mathbf{s}$ .

Let there be  $n$  observations  $\mathbf{s}_i; 1 \leq i \leq n$  and let  $\mathbf{S}$  be a set of all observations. Next, let  $k$  be the number of classes. Classification, in most general sense, is the process of constructing  $k$  sets  $\mathbf{C}_j; 1 \leq j \leq k$  by assigning each  $\mathbf{s}_i$  only to one  $\mathbf{C}_j$  set and making sure that no  $\mathbf{C}_j$  is left empty. Let the  $\mathbf{C}$  be the set of all classification sets. This can be written as:

$$\begin{aligned}\mathbf{S} &= \{\mathbf{s}_1, \mathbf{s}_2, \dots, \mathbf{s}_i, \dots, \mathbf{s}_n\} \\ \mathbf{C} &= \{\mathbf{C}_1, \mathbf{C}_2, \dots, \mathbf{C}_j, \dots, \mathbf{C}_k\}\end{aligned}\tag{2.19}$$

$$\begin{aligned}\bigcup_{j=1}^k \mathbf{C}_j &= \mathbf{S} \\ \bigcap_{j=1}^k \mathbf{C}_j &= \emptyset \\ \emptyset &\subset \mathbf{C}_j \subset \mathbf{S}\end{aligned}\tag{2.20}$$

In the K-means approach a centroid  $\mathbf{m}_j$  is assigning to each class  $\mathbf{C}_j$ . Let  $\mathbf{M}$  be the set of all centroids.

$$\mathbf{M} = \{\mathbf{m}_1, \mathbf{m}_2, \dots, \mathbf{m}_j, \dots, \mathbf{m}_k\}\tag{2.21}$$

The objective function can now be defined:

$$F(\mathbf{C}, \mathbf{M}) = \sum_{j=1}^k \sum_{\mathbf{s}_i \in \mathbf{C}_j} \|\mathbf{s}_i - \mathbf{m}_j\|^2\tag{2.22}$$

From (2.22) a rule for classification can be derived if  $\mathbf{M}$  is known. To determine to which of the  $K$  classes in  $\mathbf{C}$  belongs the observation  $\mathbf{s}_i$  a distance between  $\mathbf{s}_i$  and each centroid  $\mathbf{m}_j$  is calculated and  $\mathbf{s}_i$  is assigned to the nearest class in this absolute distance sense.

The role of K-means algorithm is to, for a given  $\mathbf{S}$ , determines  $\mathbf{M}$  that minimizes  $F(\mathbf{C}, \mathbf{M})$ . Finding a global minima of  $F(\mathbf{C}, \mathbf{M})$  is generally not possible due to a huge number of parameters but K-means does converge to a local minima. The K-means is iterative algorithm that is consisted of few steps:

1. Randomly or in some other way initial guess for the  $\mathbf{M}^{(0)}$  is obtained
2. For  $\mathbf{M}^{(t)}$ , where  $t$  is the current iteration, each observation from  $\mathbf{S}$  is classified in such a way that  $\mathbf{s}_i$  belongs to the class  $K$  for which absolute value of distance between  $\mathbf{m}_k^{(t)}$  and  $\mathbf{s}_i$  is the smallest one. As a result  $\mathbf{C}^{(t)}$  is obtained
3. New values for  $\mathbf{m}_k^{(t+1)}$  are calculated for each class  $K$  in a way that they represent mean values of all  $\mathbf{s}_n$  of the class  $\mathbf{C}_k^{(t)}$ .
4. If there is no change between  $\mathbf{M}^{(t)}$  and  $\mathbf{M}^{(t+1)}$  or if change of objective function is smaller than some threshold value the procedure ends. In all other cases algorithm goes back to step 2.

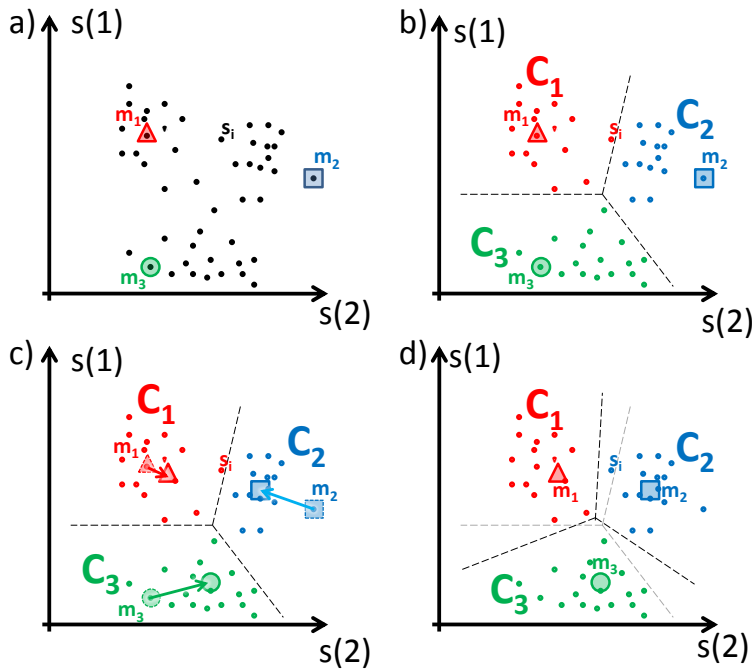


Figure 2.7: Illustration of k-means algorithm in two-dimensional space with  $n = 47$ ,  $k = 3$ .

### 2.3.1 Two-dimensional observation example

To easily illustrate K-means a two dimensional example is often used since it allows easy visualization of classification process [Fig. 2.7].

In Fig. 2.7.a all observations were presented  $\mathbf{s}$  (black dots) and some of them were randomly chosen to represent centroids  $\mathbf{M}$  represented by different shape (triangle, square, circle) and color (red, blue, green). After this step in Fig. 2.7.b,  $\mathbf{C}$  is determined as well as the boundaries between classes (dashed lines). Boundaries are geometrical places of points equally distanced from two (or more) centroids. In Fig. 2.7.c the re-estimation of the  $\mathbf{M}$  is done so that they represent mean value of class elements. Finally on 2.7.d re-classification is done and new boundaries determined. The algorithm then repeats from 2.7.c.

## 2.4 Summary

In this chapter three problems arising when dealing with spectroscopic data that need to be treated numerically were proposed. First the problem of numerical derivation was addressed and a tool was proposed in form of total variation regularization (TVR) algorithm to solve this problem. Then overview of existing normalization techniques was made, used when semi-conducting and insulating materials are studied, emphasizing their limits and also putting them in context of proposed TVR algorithm. Lastly, a method to identify electronic inhomogeneities from the huge amount of data (spectra) acquired in the spectroscopy STS maps was introduced. K-means classification algorithm was successfully implemented to the STS data analysis for getting clear information about the connection between electronic and morphologic properties of the materials.

# Chapter 3

## $\text{Pr}_{1-x}\text{Ca}_x\text{MnO}_3$ : general considerations

### 3.1 Strongly correlated materials

The properties of metals (Au, Cu, Ag ..) can be satisfactorily described by a non interacting tight-binding model. In this frame discrete energy levels of a constituent atoms are transformed into energy bands populated by electrons in the process of crystal formation. Band formation from a single energy level is the consequence of overlapping of corresponding wave functions of atoms at different lattice sites (usually just neighbor sites are considered). This overlap is mathematically represented as a 'hopping integral' or 'transfer integral' between neighboring atoms -  $t$ . Generally, the stronger the overlap  $t$  the greater is the bandwidth of the formed bands  $W$ . Ultimately conduction electrons in this frame can be treated as quasi-particles that behave as free electrons with effective mass tuned by the periodic potential of the crystal lattice.

The filling of the highest populated energy band - valence band, at zero temperature defines the electronic behavior of the material in this model. If the valence band is fully populated, than the material behaves either as an insulator or a semiconductor (depending on position of the first unoccupied band- the conduction band). If the valence band is not completely filled than the material acts as conductor and electrons are de-localized and behave like a free electron gas.

In some systems, however, one cannot ignore the Coulomb interaction between electrons and the effect of exchange on their motion that lead to correlations between particles. This is best exemplified by the class of transition metal oxide compounds (TMO) which are predicted to be conductors

by a non-interacting electrons tight-binding model, but instead are in some cases insulators, and in particular Mott insulators. This is due to the on-site Coulomb energy  $U$  (the cost of putting two electrons on the same lattice site) is so huge that it localizes the electrons on each lattice site, leading to a vanishing the electrical conductivity.

The simplest model to describe the behavior of correlated materials is the Hubbard model that in addition to kinetic term allowing for tunnelling ('hopping') of particles between sites of the lattice, introduces a potential term consisting of an on-site Coulomb interaction. As a consequence, if the on-site Coulomb repulsion  $U$  is greater than the bandwidth  $W$ , the conduction band splits in an upper Hubbard band (UHB) and a lower Hubbard band (LHB) (figure 3.1 left). In this sense apart from band-filling, knowing  $U/W$  or  $U/t$  ratio is important for determining the crystal electronic properties.

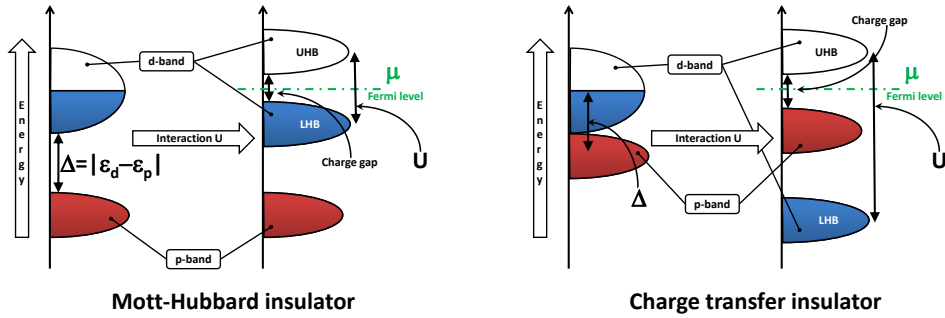


Figure 3.1: Energy diagram of two types of strongly correlated insulators

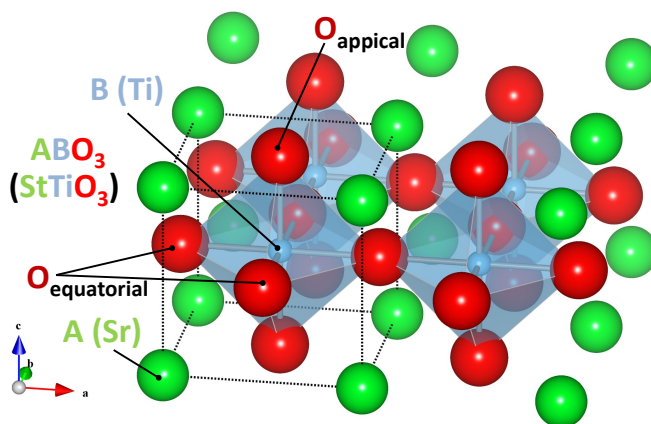
### 3.1.1 Transition metal oxides

The correlations become very important when the overlapping of highest energy orbitals between neighboring atoms is very small as is the case of transition elements in transition metal oxides.

Transition element is defined as element whose atom has an incomplete d sub-shell, or which can give rise to cations with an incomplete d sub-shell [13]. They are key ingredient in forming transition metal oxides.

The structure of transition metal oxides is that of perovskite type with cubic  $P_{m\bar{3}m}$  symmetry and general formula of  $ABO_3$ . Here A and B are cations with B usually being the transition element. One of the best known examples of ideal cubic perovskite material is  $\text{SrTiO}_3$  represented in Fig. 3.2.

As shown in figure 3.2, the transition element B is surrounded by 6 ligand oxygen atoms forming corner sharing octahedra. The ligand atoms have a

Figure 3.2: Perovskite structure;  $\text{SrTiO}_3$  example

very important role on the electronic properties of the transition metal oxides through several different mechanisms.

Since 3d orbitals are highly localized, in transition metal oxides they overlap very little with the 3d-orbital of neighbor transition element, leading to the formation of very narrow bands. In transition-metal compounds, the overlap is often determined by indirect transfer between 3d orbitals through ligand 2p orbitals [14]. This indirect coupling lowers the bandwidth even more and increases  $U/W$ .

In general, the relevant electronic states for low energy excitations transition metal compounds with light transition metal elements are different from those with heavy ones. With increase of ionic radius of transition element, the chemical potential of d electrons becomes lower, mainly because the positive nuclear charge increases with this change, and closer to the oxygen  $2p_\sigma$  orbitals leading to hybridization of the two [14]. The difference between the center of the 3d band and the hybridized  $2p_\sigma$  band,  $\Delta = \epsilon_d - \epsilon_p$ , is another parameter one has to take into consideration when discussing electronic properties of transition metal oxides. If  $\Delta$  is small enough comparing to  $U$  a new type of insulating state, called charge transfer insulator, different from a Mott-Hubbard one, arises as shown in figure 3.1 right. Very often the term Mott insulator is used to mark both kind of insulator types.

Ligands also act as points of negative charge surrounding the metal center, and as a consequence they tend to destabilize the d-shell orbitals pointing in their direction, making them energetically less favorable. As a result, a splitting of degenerate energy levels ('crystal field splitting') occurs because the orientation of the d orbital wave functions will increase an electron's energy when the orbital is located in a region of high electron density, and

### 3. $\text{Pr}_{1-x}\text{Ca}_x\text{MnO}_3$ : general considerations

lower it when the reverse is true. In crystals with cubic symmetry, the degeneracy of the d-band is lifted and it splits into two bands: three-fold degenerate  $t_{2g}$  and two-fold degenerate  $e_g$  state [Fig. 3.3 and 3.4 ].

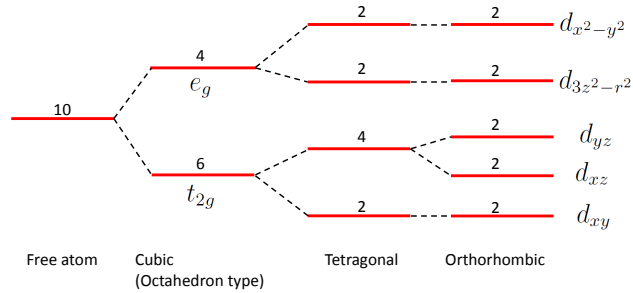


Figure 3.3: Crystal field lifting of 3d level degeneracy

In reality, a perfect cubic structure is rarely present at room temperature and more often rhomboidal or orthorhombic symmetries are present lifting the degeneracy even more [Fig. 3.3 and 3.4 ].

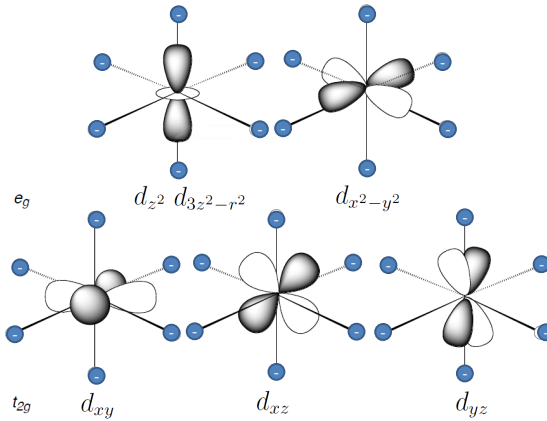


Figure 3.4: The shape of d-orbitals

The orbital configuration is clearly strongly connected with the structural distortion of the ligand octahedra. In real crystals, the  $\text{BO}_6$  octahedra can be buckled in cases when the A site element has small ionic radius. In perovskite  $\text{ABO}_3$ , the degree of buckling of  $\text{BO}_6$  octahedra is expressed by the tolerance factor:

$$t = \frac{1}{\sqrt{2}} \frac{\langle r_A \rangle + \langle r_O \rangle}{\langle r_B \rangle + \langle r_O \rangle} \quad (3.1)$$

Here  $\langle r_A \rangle, \langle r_B \rangle$  and  $\langle r_O \rangle$  represents the ionic radius of A, B and oxygen ions respectively. In general if the tolerance factor is 1 the crystal has a cubic symmetry, for  $t$  less than one, the symmetry is reduced first to rhombohedral ( $0.93 < t < 1$ ) and then to orthorhombic ( $t < 0.93$ ) [15]. The consequence of buckling is that the ideal cubic  $180^\circ$  B-O-B angle becomes smaller, hence making the electron transfer through double-exchange mechanism<sup>1</sup> between two next neighbor B ions less probable [16].

The other type of  $\text{BO}_6$  structural distortion taking place is the Jahn-Teller. It is most pronounced when an odd number of electrons occupy the  $e_g$  orbitals and a doubly-degenerate ground state is present. The Jahn-Teller theorem essentially states that the high-symmetry state with an orbital degeneracy is unstable with respect to a spontaneous decrease of symmetry, hence lifting this degeneracy [17]. This spontaneous lifting of symmetry leads to an occupation of particular orbitals and simultaneously to a structural phase transition with the reduction of symmetry. In the  $e_g$  orbital case, orbitals involved in the degeneracy, point directly to the ligands, so a distortion can result in a large energetic stabilization. As a consequence, the structural distortion in form of compressed or elongated  $\text{BO}_6$  octahedra occurs, lifting the degeneracy of  $e_g$  states. When the long range orbital order exists the JT distortion is always present [16].

In general A site in the  $\text{ABO}_3$  crystal can be occupied by different cations (as can be also done with the B site transition element). Usually a mixture of divalent alkaline and trivalent rare earth is leading to more general compound  $\text{Re}_{1-x}\text{Ae}_x\text{BO}_3$ . In this way the filling of the bands can be controlled by means of doping, making it possible to change the ground state of the parent compound by introducing additional carriers (holes or electrons) into the system.

Also, when the degeneracy is lifted, the  $e_g$  and  $t_{2g}$  levels may be coupled by Hund's rules (so called high spin state) leading to spin correlations that also influence electronic and, additionally, the magnetic properties of the crystal.

The most important difference from the usual band insulator is that the internal degrees of freedom, spin and orbital one, still survive in the Mott insulator [16]. The interplay and competition between spin, orbital, and charge degrees of freedom in this materials was shown to lead to a rich variety

---

<sup>1</sup>The double-exchange mechanism is the one which is invoked to explain the ferromagnetic-metallic state in the large bandwidth manganites like  $\text{La}_{1-x}\text{Sr}_x\text{MnO}_3$

of behaviors including colossal magneto-resistance (CMR), where enormous variations in the resistance are produced by small magnetic field changes, and high temperature superconductivity (HTSC). So the existence of several competing states is an important characteristic of these materials [18].

### 3.1.2 Manganites

During the 1990s a group of transition metal oxides, called manganites, was given special attention due to the discovery of colossal magneto-resistance effect by von Helmholt in 1993 [19]. He observed a change as high as 60% of the resistivity of  $\text{La}_{2/3}\text{Ba}_{1/3}\text{MnO}_x$  thin film with application of external magnetic field.

Manganites are transition metal oxides that are represented with general formula  $\text{Re}_{1-x}\text{D}_x\text{MnO}_3$ , with  $T$  a trivalent rare earth, and  $D$  a divalent alkaline. Oxygen is in a  $\text{O}^{2-}$  state, and the relative fraction of  $\text{Mn}^{4+}$  and  $\text{Mn}^{3+}$  is regulated by  $x$ . The electronic configuration of the topmost 3d band in manganites is shown in figure 3.5.

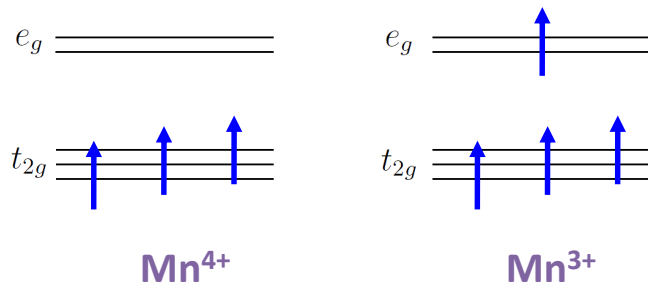


Figure 3.5: Occupation of 3d sub-shells for two different Mn valences

The valence of the Mn-ions in this context is either four ( $\text{Mn}^{4+}$ ) or three ( $\text{Mn}^{3+}$ ), and their relative fraction is controlled through chemical doping. The large Hund-coupling favours the population of the  $t_{2g}$  levels with three electrons forming a spin 3/2 state, and the  $e_g$  level either containing one electron or none. Sometimes these ions, characterized by different charges, order in charged ordered phases.

The prevailing ideas to explain the magnetotransport behavior of manganites include a picture where a large Jahn-Teller (JT) effect, which occurs in the  $\text{Mn}^{3+}$  ions, produces a strong electron-phonon coupling. This local distortion of the lattice around the charge, sometimes together with a magnetic cloud or region with ferromagnetic correlations, is called polaron and

is thought to lead to insulating behavior in paramagnetic phase above  $T_C$ . Charge ordering, on the other hand, leads to the insulating behavior because of localization of charge on the manganite site.

There are, however, evidence that, apart from a possible site-centering of the charge at the Mn site, also a bond-centered models can be invoked, together with the existence of Zener-polarons, to explain charge-ordering at non-integer  $\text{Mn}^{3+} / \text{Mn}^{4+}$  ratios [20].

The phase diagram of manganites shows richness of different phases, depending on doping content  $x$  and temperature. Even more, there are experimental evidence of intrinsic inhomogeneities in the form of coexisting competing phases in manganites [21]. This inhomogeneities strongly influence the overall physics of manganites and being able to detect them is one of the goals of this thesis.

## 3.2 $\text{Pr}_{1-x}\text{Ca}_x\text{MnO}_3$

In this work the focus will be on the narrow bandwidth  $\text{Pr}_{1-x}\text{Ca}_x\text{MnO}_3$  manganite thin films, where the correlations are extremely important. For example, this systems never show a metallic state in the whole phase diagram, at odds with the better known  $\text{La}_{1-x}\text{Sr}_x\text{MnO}_3$ .

### 3.2.1 Structure

At room temperature undoped  $\text{PrMnO}_3$  has an orthorhombic distorted structure that belongs to the  $P_{bnm}$  space group as shown in figure 3.6 a)<sup>2</sup>. To obtain  $\text{Pr}_{1-x}\text{Ca}_x\text{MnO}_3$  from  $\text{PrMnO}_3$ , trivalent  $\text{Pr}^{3+}$  is substituted with divalent  $\text{Ca}^{2+}$  ions.

As shown in the figure, a buckling of  $\text{MnO}_6$  octahedra is significant and the Mn-O-Mn angles deviate largely from the ideal  $180^\circ$ , lowering the role of double exchange as mentioned in chapter 3.1.1 . In the case of undoped PCMO, Mn-O-Mn angles are  $155^\circ$  and  $165^\circ$  for the apex and equatorial O respectively.

Although orthorhombic, if the distortion from cubic is not big, the symmetry at elevated temperatures may be considered cubic. When dealing with growth of thin films (about thin film growth see chapter 1.2.1) one can operate with appropriate pseudocubic parameters instead of orthorhombic ones as illustrated in figure 3.6 b) and equation 3.2:

---

<sup>2</sup>Image obtained using VESTA software package [22]

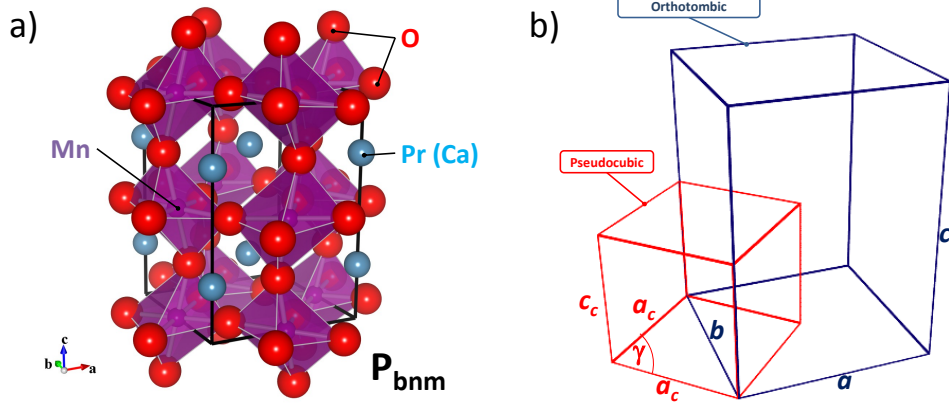


Figure 3.6: a) PCMO structure; b) Correspondence between orthorhombic and pseudo-cubic unit cell parameters.

$$a_c = \frac{\sqrt{a^2 + b^2}}{2}; \quad \gamma = \arccos\left(\frac{b^2 - a^2}{b^2 + a^2}\right); \quad c_c = \frac{c}{2} \quad (3.2)$$

### 3.2.2 Phase diagram

$\text{Pr}_{1-x}\text{Ca}_x\text{MnO}_3$  belongs to a class of narrow band manganites due to the strong correlations taking place between Mn 3d-shell electrons. In figure 3.7 a fraction of the  $\text{Pr}_{1-x}\text{Ca}_x\text{MnO}_3$  phase diagram is shown, as presented by Tomioka [23]. While intermediate and large bandwidth manganites exhibits a ferromagnetic-metallic behavior at  $x = 0.5$ , a charge-orbital ordering insulating phase (COI) is present in  $\text{Pr}_{1-x}\text{Ca}_x\text{MnO}_3$ . This phase (COI) is present in a broad range of doping from  $x = 0.3$  to  $x = 0.75$  [24].

In the range of  $0.3 < x < 0.5$  of  $Ca$  doping, the  $\text{Pr}_{1-x}\text{Ca}_x\text{MnO}_3$  exhibits antiferromagnetic insulating behavior at the temperatures below  $150K$ . There is also a canted antiferromagnetic insulating region present for the  $0.3 < x < 0.4$  doping at low temperatures. For low doping values  $x < 0.15$  a spin-canted insulating phase exists.

There is no metallic ground state present in the  $\text{Pr}_{1-x}\text{Ca}_x\text{MnO}_3$  phase diagram, even the ferromagnetic phase present for the  $0.15 < x < 0.3$  shows insulating behavior. This is the consequence of small ionic radius of  $Ca$ , that as a result has an orthorhombic distortion favouring charge localization at  $Mn$  site.

With the application of magnetic fields or large pressures, however, the insulator to metal (I-M) transition takes place, especially in the doping range

### 3. $\text{Pr}_{1-x}\text{Ca}_x\text{MnO}_3$ : general considerations

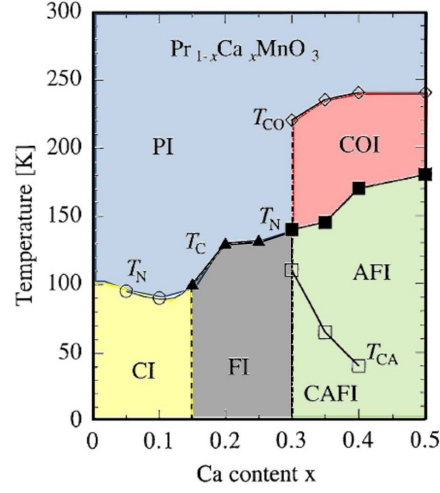


Figure 3.7: Phase diagram for  $\text{Pr}_{1-x}\text{Ca}_x\text{MnO}_3$  showing insulating character for all the doping values. PI - paramagnetic insulating phase; COI - charge-orbital ordered insulating phase; AFI - anti ferromagnetic insulating phase; CFI - canted anti ferromagnetic insulating phase; FI - ferromagnetic insulating phase; CI - spin-canted insulating phase

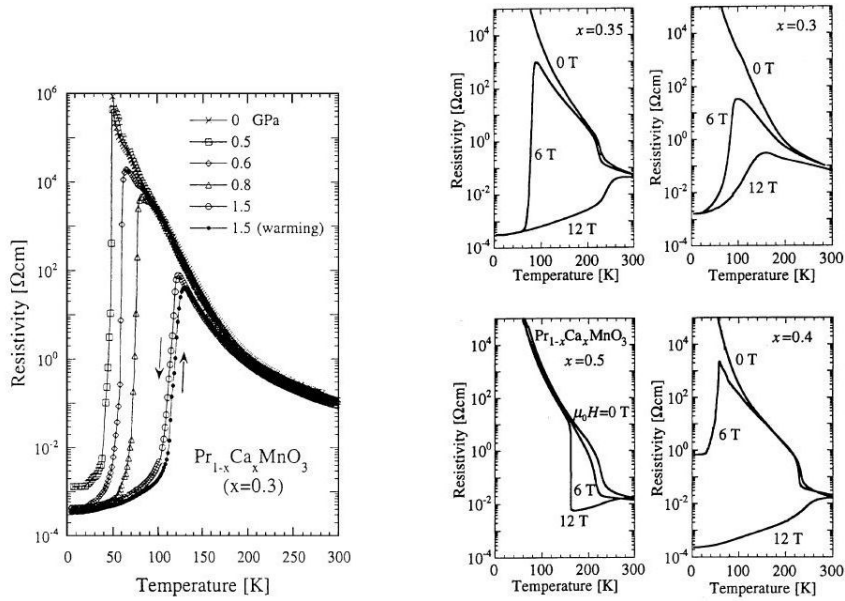


Figure 3.8: Effect of applied a) pressure [23] and b) magnetic field [25] on  $\text{Pr}_{1-x}\text{Ca}_x\text{MnO}_3$  resistivity

where COI is present [23, 25] as shown in figure 3.8. As seen from the measurements in magnetic field, the I-M transition is obtained at lower magnetic fields for the lower values of  $x$  as opposed to  $x = 0.5$ , where the transition does not take place even for very high magnetic fields. The metallic state has a ferromagnetic nature (ferromagnetic metallic phase) [26]. The change of resistivity of several order of magnitude leads to large magneto-resistance effect for the values of  $x$  around 0.3. This is a consequence of possible percolation between the charge ordered and ferromagnetic phase with COI phase being fully present at half doping, making it necessary to apply larger magnetic fields to destabilize it. In addition to the application of a magnetic field and high pressure, other perturbations can melt the insulating state: application of static electric fields [27], photo-excitation [28], X-ray irradiation [29] and electron irradiation [30].

In the COI phase of the bulk  $\text{Pr}_{0.5}\text{Ca}_{0.5}\text{MnO}_3$  ( $T_{CO} = 250$  K and  $T_N = 170$  K) apart from the check-board like site-centred arrangement of  $\text{Mn}^{4+}$  and  $\text{Mn}^{3+}$  ions, there is also an orbital and CE-type magnetic arrangement present (figure 3.9). In the  $ab$  plane the ferromagnetic zigzag lines are antiferromagnetically coupled and the coupling is AF also in the  $c$ -direction. Along the zigzag lines the charged sequence  $\text{Mn}^{3+} - \text{Mn}^{4+} - \text{Mn}^{3+} - \text{Mn}^{4+}$  is followed by orbital ordering sequence  $e_g(3x^2 - r^2) - t_{2g}^3 - e_g(3y^2 - r^2) - t_{2g}^3$ .

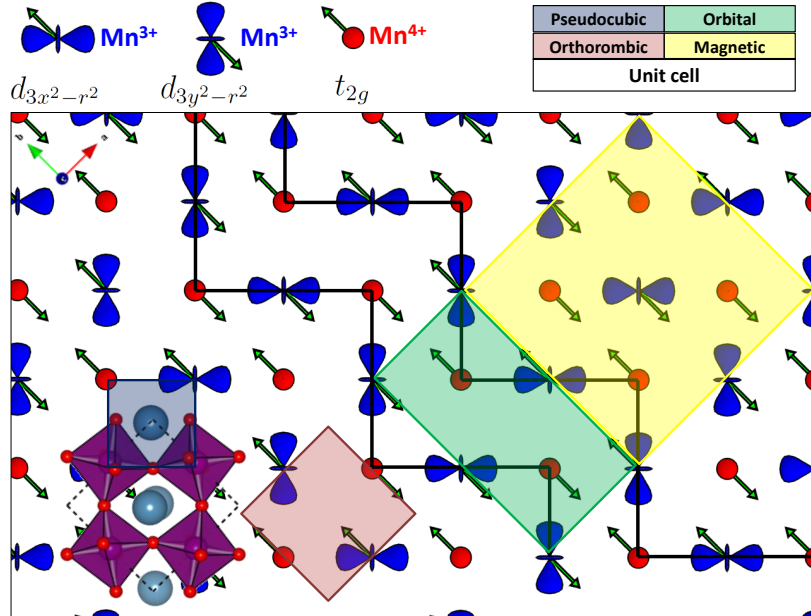


Figure 3.9: The CE-type magnetic structure present in  $x=0.5$  PCMO at low temperatures.

For the lower values of  $x < 0.5$  a bond-centred model is proposed [20, 31]. In this view metal sites remain valence equivalent and the charge is located in the bond forming so called magnetic Zener polaron - a ferromagnetically linked JT distorted octahedra with enhanced double exchange. Efremov and al. also discussed the coexistence of site and bond-centred mechanism leading to ferroelectricity [20] opening the possible path to multiferroic behavior.

### 3.3 STM on manganites

The ordered phases in manganites are usually observed by synchrotron x-ray diffraction techniques, for electronic and charge orders, and neutron scattering experiments for magnetic and structural ordering, through the inspection of the reciprocal space. The real-space approach to identify the presence of ordering is by STM and STS.

There have been several studies of manganites by STM and STS techniques [32–38]

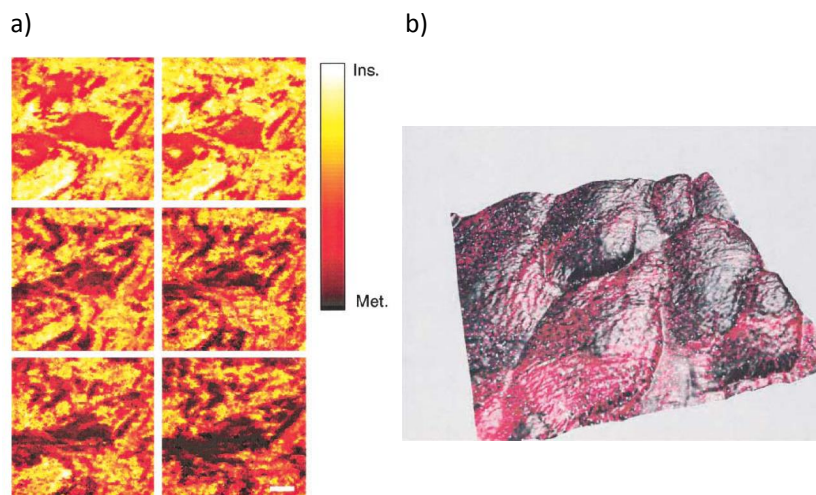


Figure 3.10: a) Evolution of insulating and metallic domains just below  $T_C$  with magnetic field (0, 0.3, 1, 3, 5, and 9 T - from left to right and top to bottom) in  $0.61 \times 0.61 \mu\text{m}^2$  of  $\text{La}_{0.7}\text{Ca}_{0.3}\text{MnO}_3$  thin film reproduced from Fäth et al [32]. b) Three-dimensional image of LCMO,  $170 \times 170 \text{ nm}^2$ , at 186 K, with topographic STM image shown with the coloring of the conductance map: black: insulating regions; red: conductive regions reproduced from Backer et al. [33].

Most of the initial STM and STS measurements on manganites had for a

goal the identification of phase separation in the temperature regions around and below the Curie temperature  $T_C$  and thus the role intrinsic inhomogeneities in manganites [32, 33]. Fäth et al. performed a series of STS measurements on intermediate-bandwidth manganite  $\text{La}_{0.7}\text{Ca}_{0.3}\text{MnO}_3$  thin film sample below  $T_C$  at different values of external magnetic field applied [32]. They identified metallic and insulating regions by observing the value of the differential conductance at certain bias voltage ( $V=3$  V) and were able to monitor the evolution of this regions with magnetic field change [Fig. 3.10 a)]. Similarly Backer et al. were able to identify phase separation in large-bandwidth manganite  $\text{La}_{0.7}\text{Sr}_{0.3}\text{MnO}_3$  thin film on MgO substrate [Fig. 3.10 b)] [33].

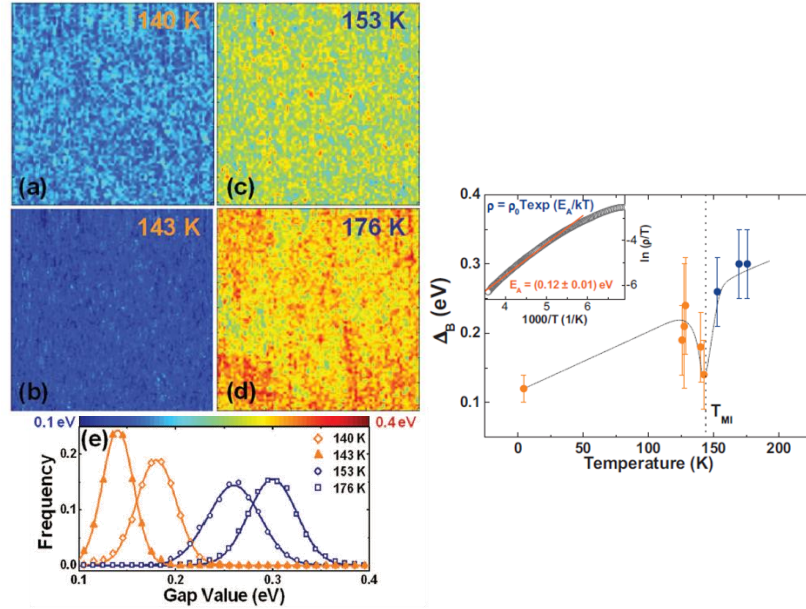


Figure 3.11: On the left the maps of conductance peak separation  $\Delta_B$  at different temperatures (a-140 K; b-143 K; c-153 K; d-176 K) and corresponding distribution on (e); On the right more detailed temperature dependence of average  $\Delta_B$  is presented. Reproduced from Seiro et al. [34].

In more recent exploration of intermediate-bandwidth  $\text{La}_{0.7}\text{Ca}_{0.3}\text{MnO}_3$  manganite thin film, Seiro et al. [34] were able to track the existence of polaronic signature in STS spectral maps even in metallic region, down to temperatures of 4.4 K [Fig. 3.11 left]. The variation of the STS gap, associated with the polaron binding energy, is also reported [Fig. 3.11 right];

The observation of insulating and metallic stripes above and below the Curie temperature  $T_C$  by a STM and STS measurement on  $\text{La}_{0.75}\text{Ca}_{0.25}\text{MnO}_3$

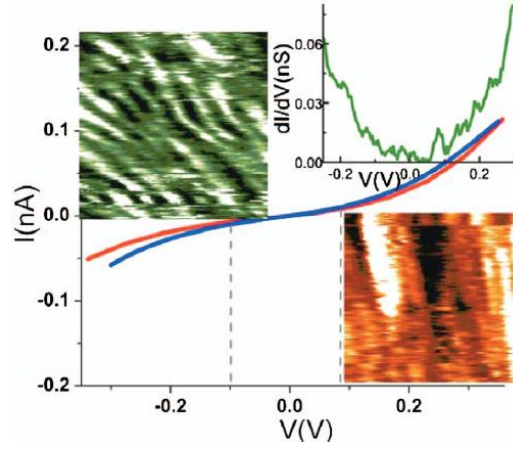


Figure 3.12: I-V curves obtained 115 K on a bond stripe ( $50 \times 50 \text{ \AA}^2$  lower right inset - red) and overall average curve ( $500 \times 500 \text{ nm}^2$  - blue). Upper insets show diagonal stripes at room temperature (upper left inset) and corresponding  $dI/dV$ -V curve on the area (upper right inset - green) - reproduced from Sudheendra et al. [35].

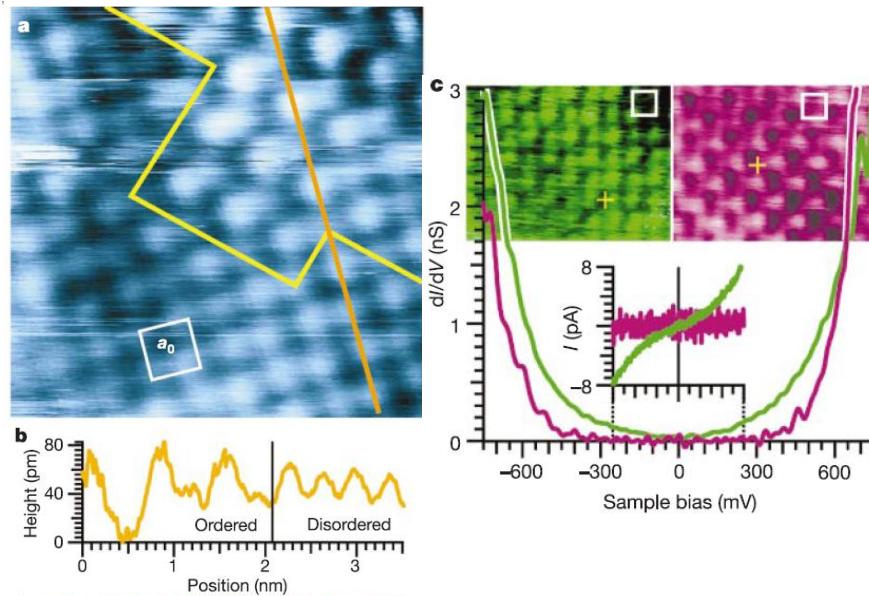


Figure 3.13: Topographic (left) and spectroscopic atomic-scale signatures (right) of phase separation into metallic and insulating regions in the paramagnetic phase of  $\text{Bi}_{0.24}\text{Ca}_{0.76}\text{MnO}_3$  at 299 K. Reproduced from Renner et al. [39].

### 3. $\text{Pr}_{1-x}\text{Ca}_x\text{MnO}_3$ : general considerations

were reported by Sudheendra et al. [35]. The formation of these stripes is an outcome of an overlapping of electron wave functions mediated by the intrinsic lattice strain and involves competing charge, orbital, and lattice orders [Fig. 3.12].

Phase separation was also observed in paramagnetic phase of narrow-bandwidth  $\text{Bi}_{1-x}\text{Ca}_x\text{MnO}_3$  compound. Renner et al. identified two structural phases on atomic scale [39]: homogeneous cubic region ( $a_0 \times a_0$ ) and charged ordered  $\sqrt{2}a_0 \times \sqrt{2}a_0$  one [Fig. 3.13 left]. STS was also performed showing more insulating nature of the charged ordered region, as expected [Fig. 3.13 right].

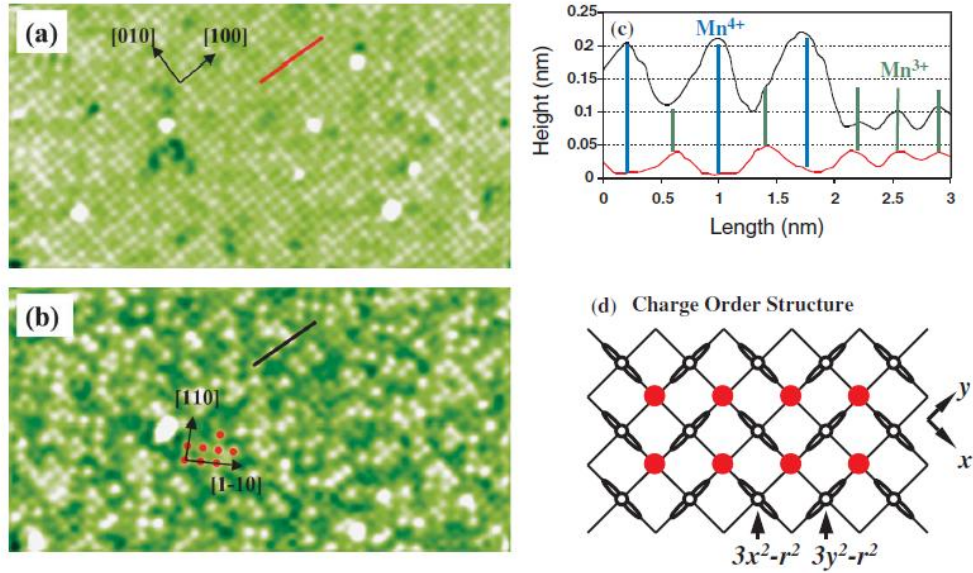


Figure 3.14: Topographic atomic-scale images probing occupied states (a) and unoccupied states (b) with corresponding profiles (c) on  $\text{La}_{5/8-0.3}\text{Pr}_{0.3}\text{Ca}_{3/8}\text{MnO}_3$  thin film grown on Nb-doped (001)-oriented  $\text{SrTiO}_3$  and CE-type model for explaining charge ordering phase. Reproduced from Ma. et al. [37]

Another direct observation of charge ordering was presented by Ma. et al. on narrow-bandwidth  $\text{La}_{5/8-0.3}\text{Pr}_{0.3}\text{Ca}_{3/8}\text{MnO}_3$  thin film grown on Nb-doped (001)-oriented  $\text{SrTiO}_3$  [Fig. 3.14] [37]. The measurements were done in the COI range of temperatures and showed again the existence of two phases, charge ordered and disordered one. The CE-model shown earlier on 3.9 (page 56) is also considered here to explain the ordering type.

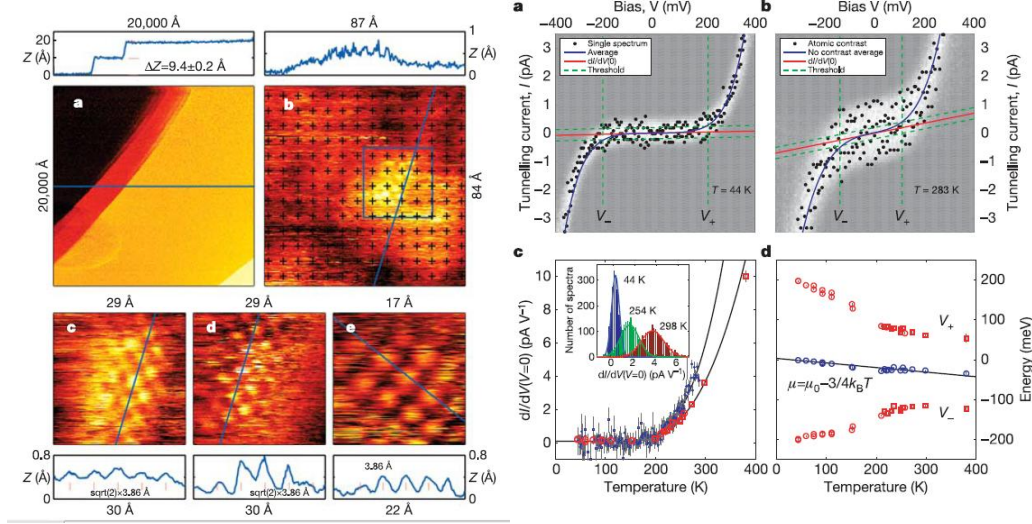


Figure 3.15: The topographic images obtained on *in situ* cleaved  $\text{La}_{1.4}\text{Sr}_{1.6}\text{Mn}_2\text{O}_7$  showing the island areas with atomic resolution (left); STS measurements of I-V curves on 44K (right a) and 283 K (right b) reveal the zero bias conductance change (right c) as well as change in chemical potential (right d) with temperature. Reproduced from Rønnow et al. [38].

In a work on layered  $\text{La}_{2-2x}\text{Sr}_{1+2x}\text{Mn}_2\text{O}_7$  manganite Rønnow et al. were able to obtain atomic resolution on only small areas on the atomically flat surfaces [38]. The size of this tiny areas matched approximately 30 unit cells with the expected 3.86 Å Mn ion spacing lattice parameter. These areas however were not regarded as phase separation, but as a local perturbation by some atomic-scale defect in the homogeneous system. They speculate that a sufficiently strong defect may bind (trap) a quasiparticle, in this case a polaron, resulting in a non-dispersive real-space STM image reflecting the internal structure of the polaron, seen as areas with atomic resolution.

### 3.4 Summary

In summary the inhomogeneities seem to be intrinsic for manganites, thus determining their electronic properties. STM together with STS is able to identify different existing phases: structural one by STM and electronic ones by STS. Also, in paramagnetic phase the polaronic mechanism of conducting can be identified by comparing the pseudo-gap value obtained by STS to that of the activation energy in polaron conduction model obtained by transport

### 3. $\text{Pr}_{1-x}\text{Ca}_x\text{MnO}_3$ : general considerations

---

measurements. Finally STM and STS open a real-space view into COI state of manganites surfaces.

# Chapter 4

## Scanning tunneling spectroscopy on $\text{Pr}_{1-x}\text{Ca}_x\text{MnO}_3$ thin films

In this chapter scanning tunnelling microscopy and spectroscopy (STM and STS) results will be presented for two doping levels of  $\text{Pr}_{1-x}\text{Ca}_x\text{MnO}_3$  thin films –  $x = 0.5$  and  $x = 0.3$  – that correspond to the boundary values of COI state in the PCMO phase diagram. Both film types were prepared in situ in the deposition chamber of the MODA system by pulsed laser deposition in controlled  $\text{O}_2$  atmosphere. The samples were analyzed *in-situ* and all the measurements were done in UHV conditions ( $10^{-11}$  up to low  $10^{-10}$  mbar), thus minimizing the role of surface contamination.

### 4.1 $\text{Pr}_{0.5}\text{Ca}_{0.5}\text{MnO}_3$

The first STM/STS measurement were done on 10 nm  $\text{Pr}_{0.5}\text{Ca}_{0.5}\text{MnO}_3$  thin film deposited on A-site terminated  $\text{NdGaO}_3$  (110) (NGO) single crystal. The choice of this termination, should lead to B terminated manganite film, thus making the ligand octahedra around Mn ions complete. Although  $\text{SrTiO}_3$  is the usual substrate of choice when transition metal oxides films are grown, it is difficult to obtain A-site terminated  $\text{SrTiO}_3$  substrate, thus  $\text{NdGaO}_3$  is the best solution for achieving A-site termination.

As PCMO, the NGO crystal belongs to the  $P_{bnm}$  space group with an orthorhombic unit cell. The lattice parameters are

- $a=5.3949(1)$  Å,  $b=5.4042(2)$  Å: and  $c=7.6064(2)$  Å for the  $\text{Pr}_{0.5}\text{Ca}_{0.5}\text{MnO}_3$  [24, 40];

#### 4. Scanning tunneling spectroscopy on $\text{Pr}_{1-x}\text{Ca}_x\text{MnO}_3$ thin films

---

and

- $a=5.4276 \text{ \AA}$ ,  $b=5.4979 \text{ \AA}$ : and  $c=7.7078 \text{ \AA}$   
for the case of  $\text{NdGaO}_3$  [41].

According to equation (3.2) the corresponding pseudocubic lattice parameters are:

- $a_c=3.818 \text{ \AA}$ ,  $\gamma=89.95^\circ$  and  $c_c=3.803 \text{ \AA}$ : for PCMO
- $a_c=3.863 \text{ \AA}$ ,  $\gamma=89.26^\circ$  and  $c_c=3.854 \text{ \AA}$ : on NGO

Comparing the pseudocubic parameters one can see that tensile strain would be applied to PCMO thin film grown on an NGO (110) substrate. Adopting the mismatch definition referred to the thin film in-plane lattice parameter:

$$\delta_m = \frac{a_{\text{substrate}} - a_{\text{film}}}{a_{\text{film}}} \quad (4.1)$$

we can calculate that in the best case scenario:

$$\begin{aligned} \delta_m &= \frac{3.863 \text{ \AA} - 3.818 \text{ \AA}}{3.818 \text{ \AA}} = 1.18\% \\ \delta_m &= \frac{3.854 \text{ \AA} - 3.803 \text{ \AA}}{3.803 \text{ \AA}} = 1.34\% \end{aligned} \quad (4.2)$$

resulting in slightly strained film with a c-axis a bit lower due to the tensile nature of the strain.

The 10 nm thin  $\text{Pr}_{0.5}\text{Ca}_{0.5}\text{MnO}_3$  film was grown on A site terminated NGO in the growth chamber of MODA system. The deposition was performed at  $800^\circ \text{ C}$  in a dynamic oxygen pressure of  $p_{\text{O}_2}=0.1 \text{ mbar}$ . The growth was monitored by RHEED. During the measurement, the RHEED pattern always indicated a 2D structure [Fig. 4.1 right] and by observing RHEED oscillations the film thickness was calculated to be 10 nm [Fig. 4.1 left].

To confirm this findings x-ray diffraction measurements were done, showing fully strained PCMO film. The tensile nature of the strain applied to the sample, is confirmed by a lower  $c_{\text{film}}$  parameter compared to the bulk value (figure 4.2 a). The rocking curve shows film of good quality with small dislocations density (figure 4.2 a).

X-ray reflectivity measurements show that the film is 10 nm thick (figure 4.3), as expected and is very smooth.

#### 4. Scanning tunneling spectroscopy on $\text{Pr}_{1-x}\text{Ca}_x\text{MnO}_3$ thin films

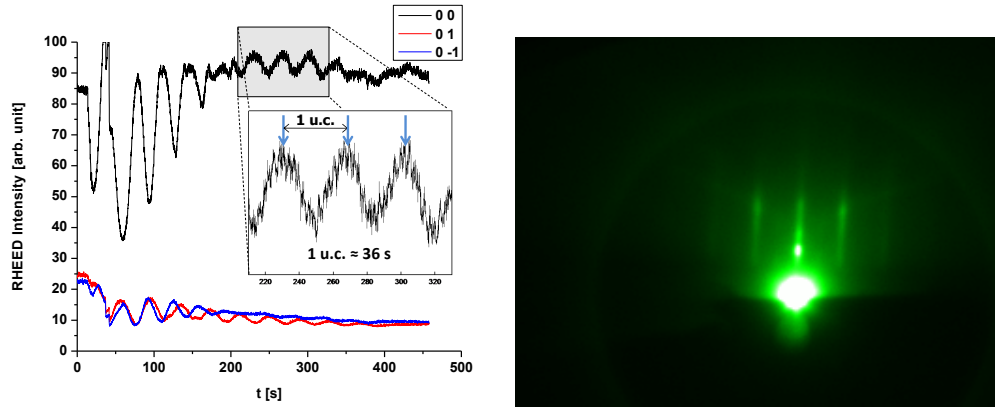


Figure 4.1: RHEED oscillation during the growth of PCMO( $x=0.5$ ) (left) and RHEED pattern after the deposition (right)

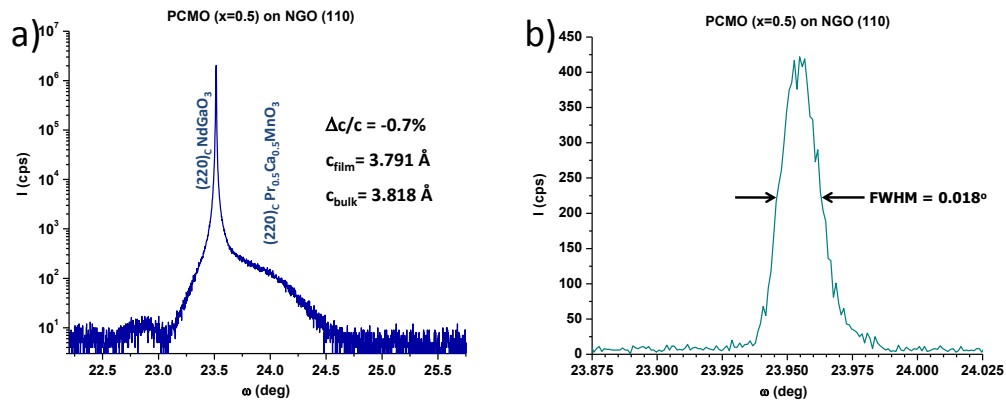


Figure 4.2: a) XRD around  $[220]$  NGO pick with corresponding PCMO( $x=0.5$ ) pick; b) Rocking curve.

#### 4. Scanning tunneling spectroscopy on $\text{Pr}_{1-x}\text{Ca}_x\text{MnO}_3$ thin films

---

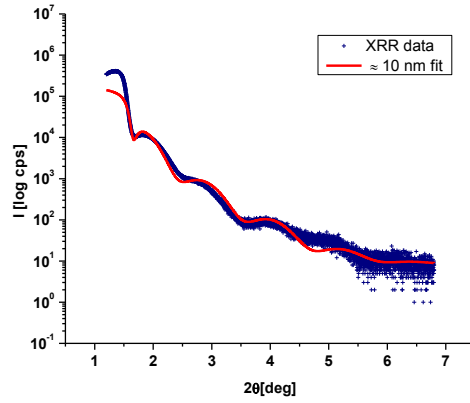


Figure 4.3: X-ray reflectivity measurements and the fit for the 10 nm thickness

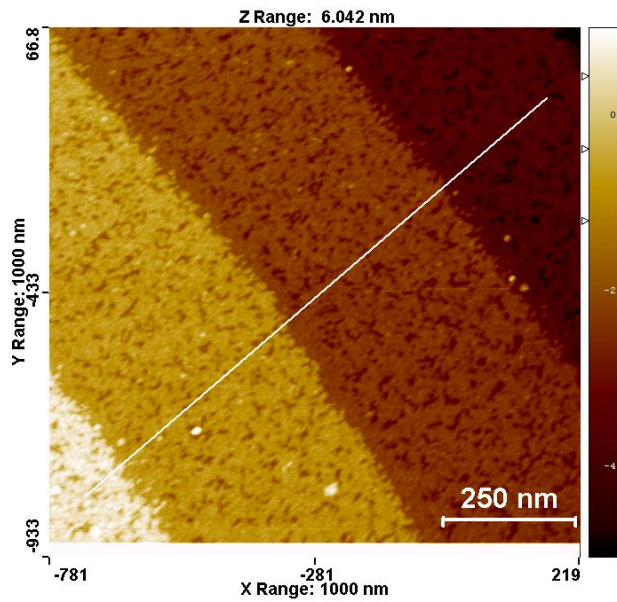


Figure 4.4: NC-AFM image of  $\text{PCMO}(x=0.5)$  thin film surface

The first SPM technique implemented was non-contact atomic force microscopy. A typical topographic image is shown in figure 4.4.

Here  $1 \times 1 \mu\text{m}^2$  area is shown. Terraces are around 400 nm wide and show a root mean square roughness of  $1.308 \text{ \AA}$ . The coverage is less than 1. This is in accordance with the RHEED measurement that indicate a layer by layer growth. The coverage close to the step edges and in the middle of the terraces are not the same. One can observe that the coverage is complete within 20 nm from the terrace edges. In some places of the step edge, a nucleation of the next layer can be noticed in shape of 2D islands.

The height of the step edge is  $3.9 \pm 0.2 \text{ \AA}$  indicating single termination and perfect cube on cube growth, following the pseudocubic lattice parameters. The expected termination of the film is that of  $\text{Pr}_{1-x}\text{Ca}_x\text{O}$ , in agreement with the stacking sequence imposed by the A-site terminated NGO [Fig. reffig:AFMPMC05profiles].

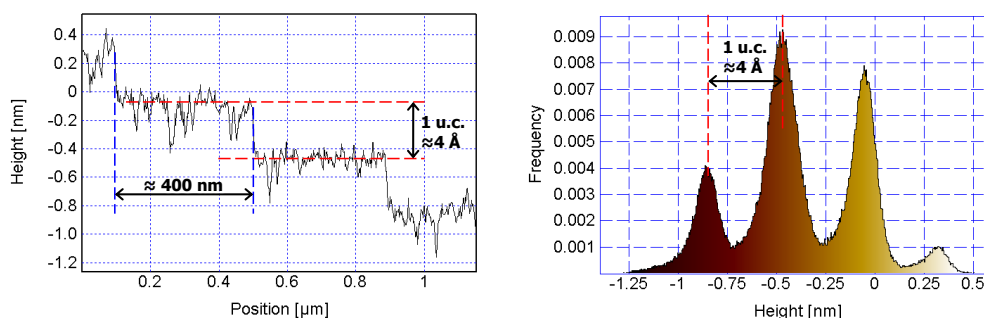


Figure 4.5: Step edge profile (left) and corresponding height histogram distribution (right) for the NC-AFM measurement presented in Fig. 4.4

Topographic measurements were redone with the STM technique. The PCMO film exhibit a clear insulating character demonstrated by an exponential increase of the resistivity decreasing the temperature, measured ex situ after the in situ analysis. Nevertheless, at room temperature the conductivity is low enough to allow STM measurements. To obtain STM images, the use of positive bias<sup>1</sup> was necessary. All attempts to obtain images with negative bias voltages resulted in charge like behavior - the tip to sample distance would decrease leading to eventual tip crash.

A large scale image obtained in the STM is shown in figure 4.6 together

<sup>1</sup>although Omicron VT-SPM is tip biased device with grounded sample (as mentioned in 1.2.3) the positive bias in the rest of the work refers to sample electrode being on higher potential than the tip electrode

#### 4. Scanning tunneling spectroscopy on $\text{Pr}_{1-x}\text{Ca}_x\text{MnO}_3$ thin films

---

with the edge profile and corresponding histogram in 4.7. The data are in complete agreement with previously obtained NC-AFM measurement.

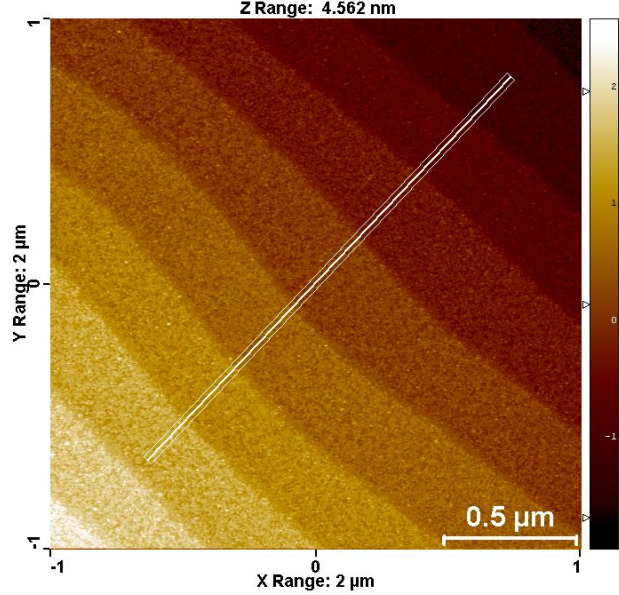


Figure 4.6: STM image of  $\text{PCMO}(x=0.5)$  thin film surface,  $I_{SET}=500$  pA;  $V_{BIAS}=1$  V

The difference between NC-AFM and STM measurement are on smallest scale, where superior STM resolution reveals more details, allowing the estimation of the coverage of the terraces through use of the pore identification technique [Fig. 4.8]. In this case the coverage is estimated to be 71.0%.

To improve the surface morphology, annealing procedure are often applied. To this purpose we performed a 1 hour re-annealing of this film in the same condition as the deposition ( annealed at  $800^\circ\text{C}$  and dynamic oxygen pressure of  $p_{\text{O}_2}=0.1$  mbar). After cooling the sample to room temperature ( $20^\circ\text{C}$  per minute), the film was again introduced into STM chamber. It is important to underline that all the SPM measurements were done *in-situ* and in UHV conditions with  $10^{-10}$  mbar pressure in the analysis and distribution chamber.

The STM measurements after the re-annealing revealed a different topography. First we notice that a reorganization of the material at the surface, with an increase of the average perimeter of single valleys from 33 nm to 83 nm, while maintaining the overall coverage (69.6% compared to 71% before the annealing ). Even more, there is the preferential orientation of the edges of the valleys and of the islands- which result to be either perpendicular or parallel to the step edges.

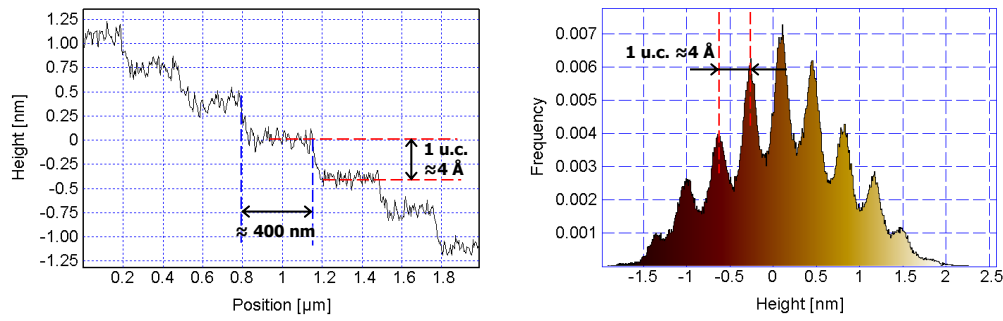


Figure 4.7: Step edge profile (left) and corresponding height histogram distribution (right) for the STM measurement presented on Fig. 4.6

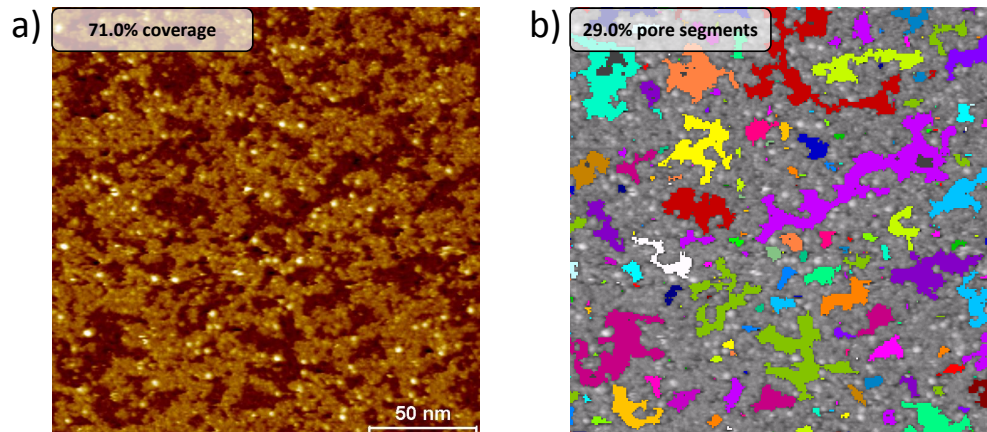


Figure 4.8: a) Terrace details, showing that the layer is incomplete, and b) corresponding segment image identifying valleys (uncovered parts) of the surface

#### 4. Scanning tunneling spectroscopy on $\text{Pr}_{1-x}\text{Ca}_x\text{MnO}_3$ thin films

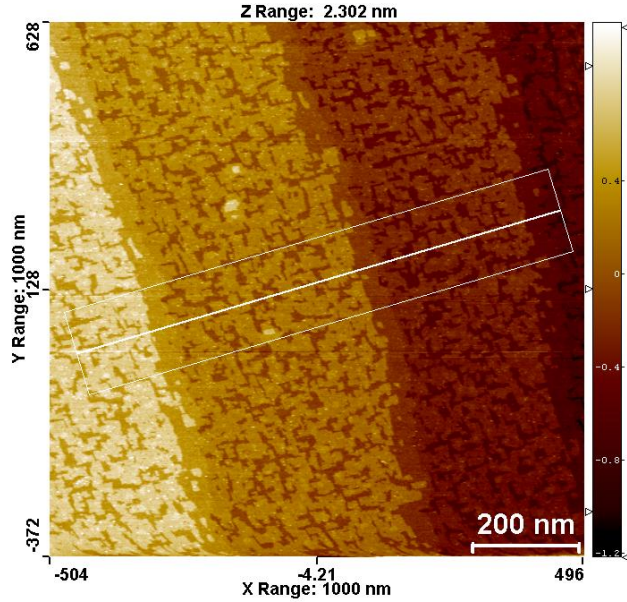


Figure 4.9: STM image of re-annealed PCMO( $x=0.5$ ) thin film surface,  $I_{SET}=2$  nA;  $V_{BIAS}=1.25$  V

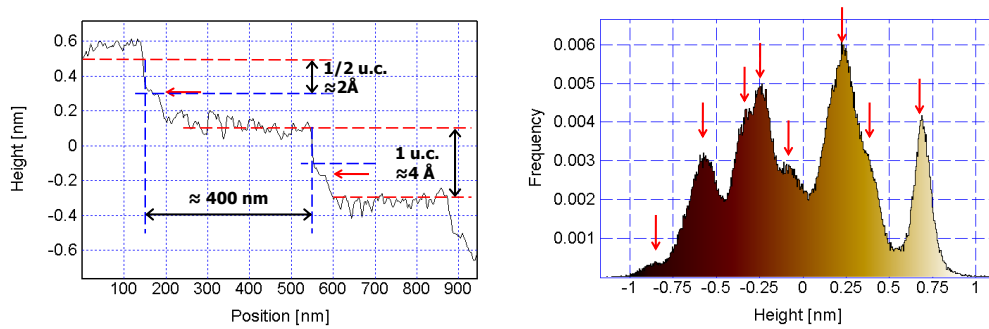


Figure 4.10: Step edge profile (left) and corresponding height histogram distribution (right) for the STM measurement presented in Fig. 4.9

When observing the average step profile it also seems that only a single termination is present with characteristic  $\approx 3.9 \text{ \AA}$  step height. However, a closer inspection of the edge region show that, close to the edge, different terminations are present. This is demonstrated by the height histogram, which exhibits peaks separated by values different from an integer number of pseudocubic unit cell [Fig. 4.10]. Similar double terminated areas close to the step edges were already reported in  $\text{La}_{5/8-0.3}\text{Pr}_{0.3}\text{Ca}_{3/8}\text{MnO}_3$  thin films by Ma [42]. The only difference is that there the film was deposited on Nb-doped (001)-oriented  $\text{TiO}_2$  terminated (B-site)  $\text{SrTiO}_3$  (STO).

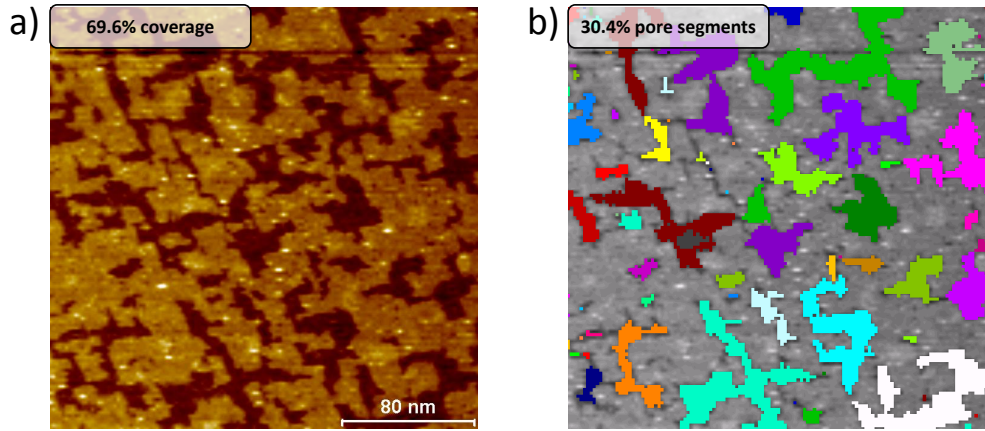


Figure 4.11: The terrace detail showing not fully covered layer a) and the corresponding segment image identifying holes (uncovered parts) of the surface. Two perpendicular preferential directions for pore edges are observed.

Further investigation on the sample showed that, near the sample corner, topographically rich areas are present, showing different terminations also in the middle of a single terrace [Fig. 4.12]. These differences are probably due to non-uniform temperature of the sample during deposition and annealing, leading to different distribution of the target material.

According to the general discussion on the strongly correlated material, as opposed to the band semiconductors, these structural differences should also give rise to different electronic signatures. For this reason, scanning tunnelling spectroscopy mapping was chosen for probing the electronic properties of  $\text{PCMO}(x=0.5)$  at different spatial coordinates of the surface. STS of  $\text{PCMO}$  at room temperature were quite challenging. As mentioned before, the negative bias measurements led to charging of the surface making the measurement unstable and unreliable. So probing of the occupied states was very difficult. The second challenge comes from the idea to use the lock in technique at room temperature and with no temperature regulation in place.

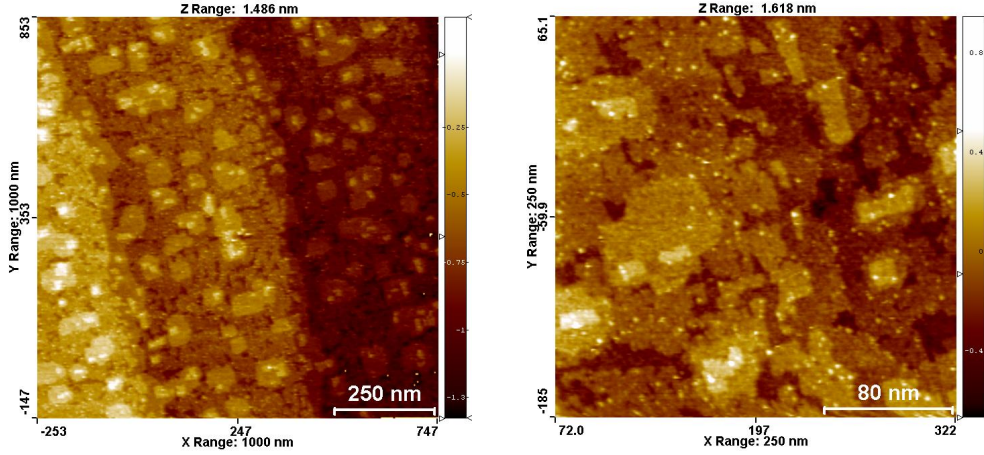


Figure 4.12: Parts of the sample characterized by a topography consisting of double terminated islands present also on a single terrace away from the edges

At the same time, it was important not to sacrifice the spatial resolution in the acquisition of the surface map, because the primary goal was to investigate the spatial inhomogeneities, if any, of the spectral response. As a consequence low energy resolution spectra were obtained with resolution of only 100 mV in the 0 - 1.5 eV range.

For obtaining the differential conductance, the lock-in technique was used with optimized lock-in frequency  $f_0 = 2017$  Hz. Higher frequencies led to the increase of the crosstalk. Modulation voltage amplitude was kept at  $V_m = 30$  mV, which took into account the thermally limited resolution. Although the resolution was only 100 mV, higher amplitudes of modulation voltage were not used due to the concern of nonlinear response due to, expected, non linear current-voltage characteristic (see chapter 1.3.2). Bias voltage was determined by the maximum of the spectral range and was kept at  $V_{BIAS} = 1.5$  V and set current was optimized to 1 nA, giving a strong spectroscopic signal yet not being too big to make the tunneling unstable. The value of the tunnelling current and differential conductance were measured simultaneously, resulting in two sets of spatially spread spectra - I vs V and  $dI/dV$  conductance one.

To get the DOS, the total conductivity normalization was used. A 10 pA current offset was chosen from the estimated level of noise of our setup.

Being a system where electronic phase inhomogeneities could be present we have used the K-means algorithm to look for possible phase separation of this system at room temperature. In figure 4.13 the result of the K-means

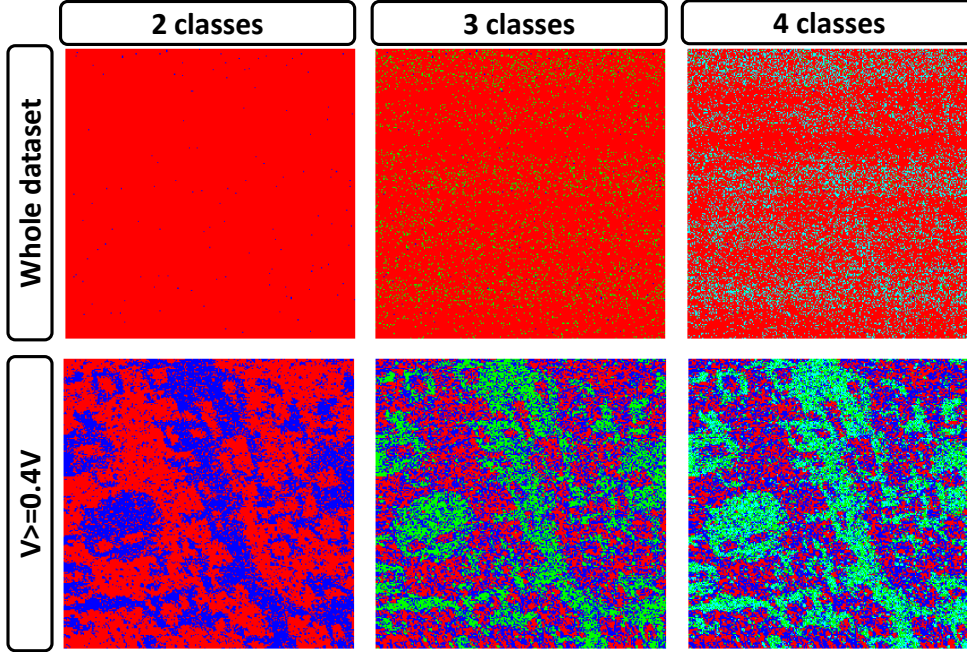


Figure 4.13: K-means classification applied on the normalized conductivity data with different number of classes assumed. Upper row: the whole voltage range is included during classification process; lower: only values outside the gap were used ( $V_{BIAS} \geq 0.4$ )

classification is shown for different conditions.

In the upper row, the classification is done using the whole spectral range from 0 V to 1.5 V, and in lower row only the out of gap values (0.4 V to 1.5 V) were used. Each column corresponds to the assumed number of classes. The classification based on the whole spectral range did not show any kind of spectra separation. The explanation for this is the low signal to noise ratio in the gap, leading to noise dominated classification rather than signal dominated one, and resulting in an uniform classification maps. On the other hand, the classification based on the data outside the gap region, produced images that separate the spectra into spatially more or less homogeneous groups correlated to the thin film termination. The 2,3 and 4 class cases show more details of each single termination.

The 2 class classification [fig. 4.14] clearly shows that different spectral signatures correspond to different terminations. The difference is mainly in the normalized conductivity (or LDOS) value. Having in mind that  $\text{Pr}_{1-x}\text{Ca}_x\text{O}$  termination is expected (corresponding to the red color in this

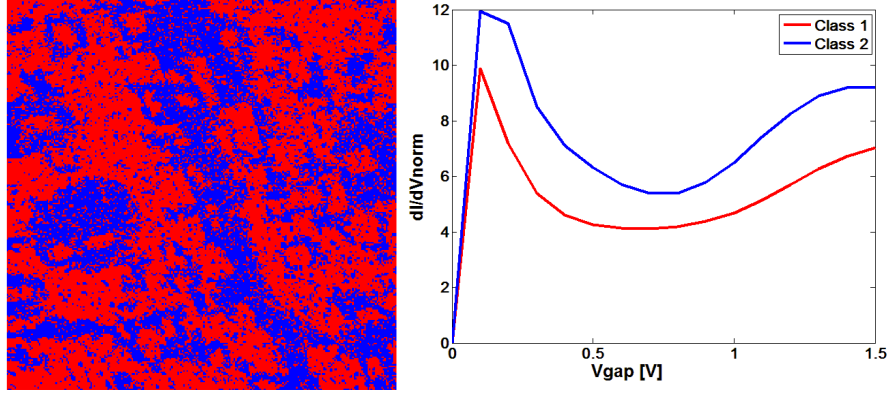


Figure 4.14: K-means classification image for the 2 classes (left) and corresponding medians of the spectra by class (right).

image) the figure 4.14 suggests that the density of states is generally lower for  $\text{Pr}_{1-x}\text{Ca}_x\text{O}$  as compared to the  $\text{MnO}_2$  termination. One of the possible reasons for the different response lies, as mentioned, in a strong connection between the structural deformations and electronic properties in strongly correlated systems, especially in narrow band manganites as PCMO. A simple absence of apex oxygen probably breaks the polaronic mechanism of conduction, known to be the major transport mechanism in high temperature narrow band manganites. This favours de-localization of the electron making this configuration exhibiting a more conductive like behavior.

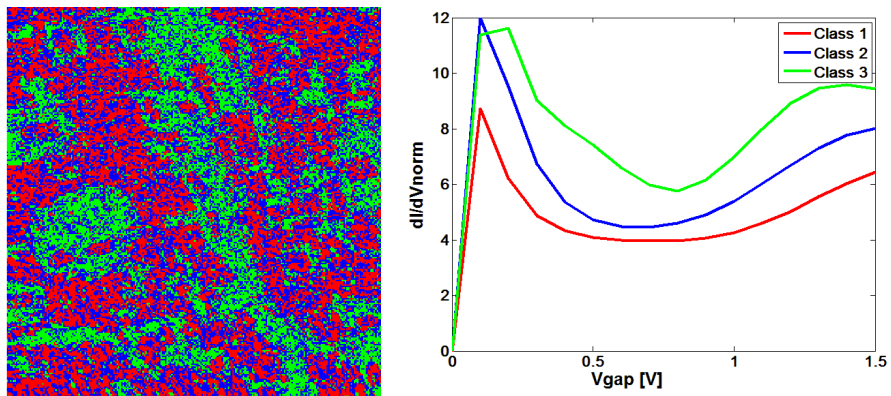


Figure 4.15: K-means classification image for the 3 classes (left) and corresponding medians of the spectra by class (right).

The 3 class classification [Fig. 4.15] is in a way very similar to 2 class

one with only difference being introduction of intermediate class (blue one) present in both termination region. So we can observe this intermediate class simply as a algorithm induced one.

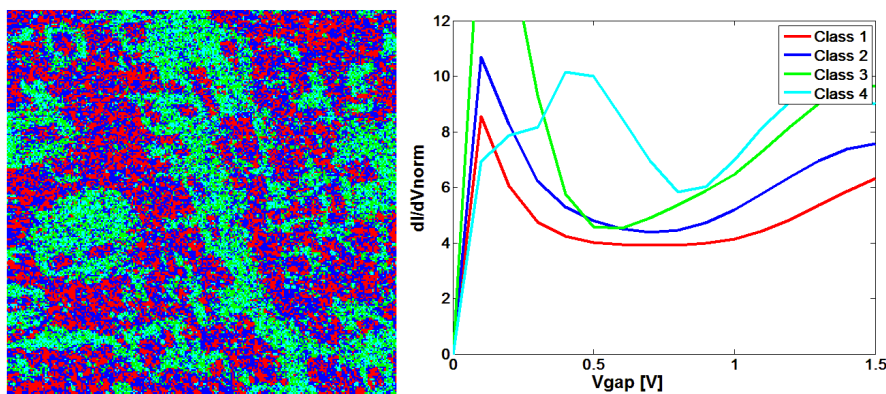


Figure 4.16: K-means classification image for the 2 classes (left) and corresponding medians of the spectra by class (right).

The 4 class classification [Fig. 4.16], on the other hand, does not introduce just another intermediate class but rather shows the inhomogeneities of spectral response on each of the two termination separately. This is manifested in grouping the classes into one that corresponds to  $\text{Pr}_{1-x}\text{Ca}_x\text{O}$  termination (red and dark blue) and one that are corresponding to the  $\text{MnO}_2$  termination (light blue and green). Unfortunately the spatial, and even more, the energy resolution do not allow us to give any conclusions on the nature of this termination inhomogeneities. They can be related to the Ca or Pr content, the presence of short-range charge ordering [43] or polaron like signatures [44].

## 4.2 $\text{Pr}_{0.7}\text{Ca}_{0.3}\text{MnO}_3$

The other set of measurements was performed on the very thin film of  $\text{Pr}_{0.7}\text{Ca}_{0.3}\text{MnO}_3$  grown on B-terminated  $\text{SrTiO}_3$ . In this case the expected termination is that of  $\text{MnO}_2$  layer.

The  $\text{Pr}_{0.7}\text{Ca}_{0.3}\text{MnO}_3$  has the  $P_{bnm}$  lattice structure at room temperature with:  $a=5.462(1)$  Å,  $b=5.478(2)$  Å: and  $c=7.679(2)$  Å: [24]. Pseudo-cubic parameters according to equation (3.2) are  $a_c=3.868$  Å,  $\gamma=89.92^\circ$  and  $c_c=3.840$  Å:. On the other hand  $\text{SrTiO}_3$  has cubic structure of  $P_{m\bar{3}m}$  space group symmetry and the cubic lattice parameter  $a_c=3.905$  Å

The growth was done at optimized parameters for PCMO :  $800^\circ$  C and dynamic oxygen pressure of  $p_{\text{O}_2}=0.1$  mbar. The growth was monitored by

RHEED and from the oscillation period and the deposition time the thickness is estimated. A sample composed by only 5 u.c. ( $\approx 2$  nm) was studied. The RHEED pattern indicated flat, crystalline and non-reconstructed 2D surface 4.17.

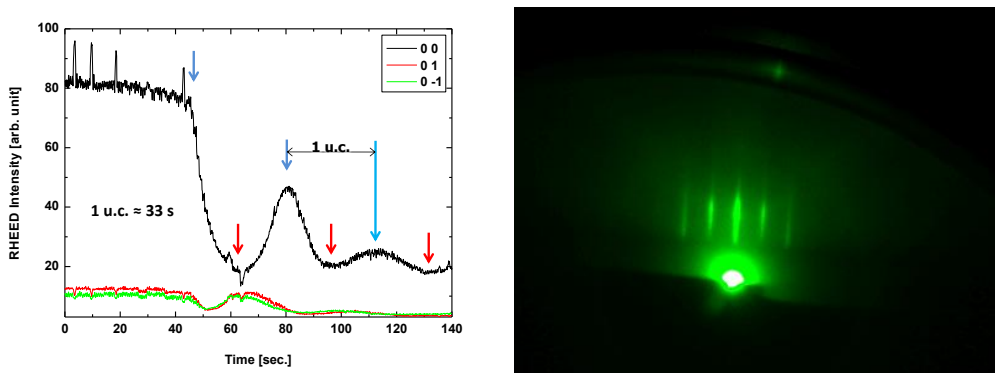


Figure 4.17: RHEED oscillation during the growth of PCMO( $x=0.3$ ) (left) and RHEED pattern after the deposition (right)

The the large scale STM image of the film shown in figure 4.18, reveals very interesting topographic features. In general two regions can be identified: atomically flat parts and parts that have stripe like structures.

Atomically flat terraces are one unit cell separated in height as expected [Fig. 4.19]. The regions of the stripe like features are present only close to the step-edges or close to islands regions and they are always oriented parallel or perpendicular to these edges. Although it is usually assumed that during the deposition at elevated temperatures, PCMO (and , in general, perovskite materials) grows as having a pseudo-cubic structure, there are evidence of the orthorhombic growth with the  $c$ -axis lying in the plane. Fujimoto at al. identified two different domain orientations of  $\text{Pr}_{0.7}\text{Ca}_{0.3}\text{MnO}_3$  on a (001)  $\text{SrTiO}_3$  single crystal substrate from the X-ray diffraction result as shown in figure 4.20 right [45]. This can explain the two perpendicular orientation of the stripes. Profile on the smaller scale image shows that distance between stripes is 4 nm [Fig. 4.20 left]. This could be explained with known preferential stripe growth in the direction of shorter axes (in this case PCMO pseudocubic one) and not in the orthorhombic  $c$ -axis direction. Having this in mind each stripe is 3 u.c. wide in the  $c$ -axis direction.

It seems that the initial growth favours stripe formation in the layer by layer growth mode, and than, after 2 or 3 u.c. the dynamics of the growth changes and becomes more step-flow like. This is in accordance with disappearance of RHEED oscillations while the diffraction pattern as well

4. Scanning tunneling spectroscopy on  $\text{Pr}_{1-x}\text{Ca}_x\text{MnO}_3$  thin films

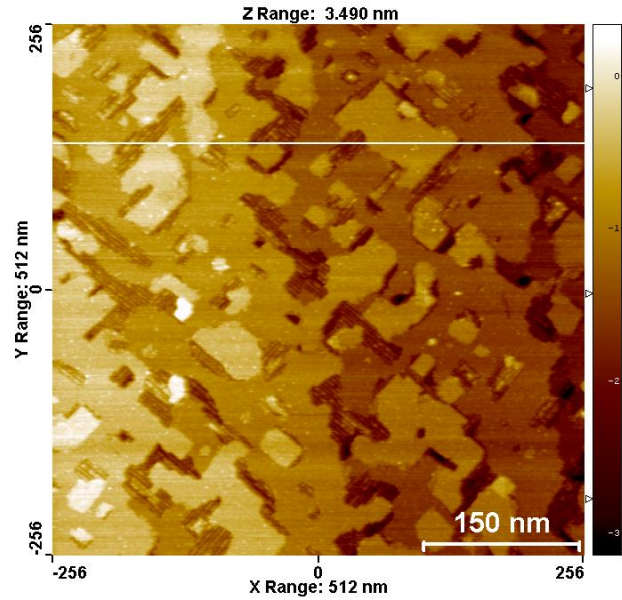


Figure 4.18: STM image of re-annealed  $\text{PCMO}(x=0.5)$  thin film surface,  $I_{SET}=2$  nA;  $V_{BIAS}=1.25$  V

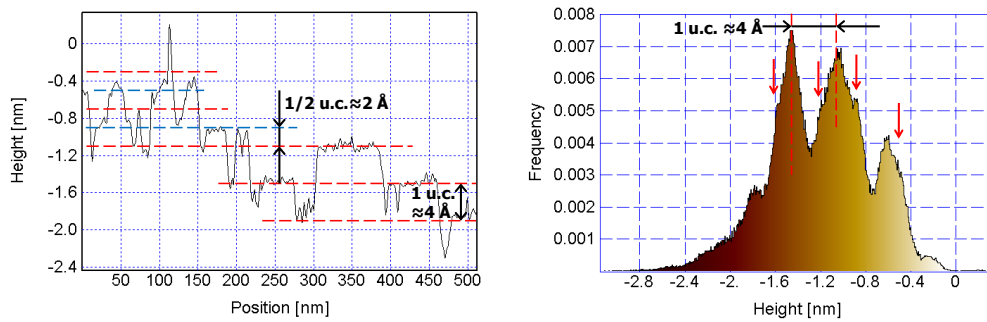


Figure 4.19: Step edge profile (left) and corresponding height histogram distribution (right) for the STM measurement presented in Fig. 4.18

#### 4. Scanning tunneling spectroscopy on $\text{Pr}_{1-x}\text{Ca}_x\text{MnO}_3$ thin films

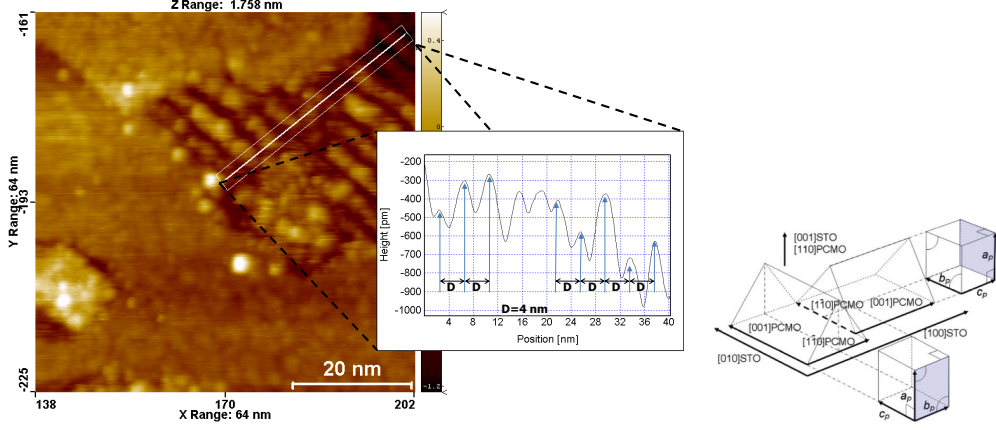


Figure 4.20: The stripe region and corresponding profile reveal 4 nm distance between stripes on  $\text{PCMO}(x=0.3)$  thin film on B-terminated STO

as our measurements indicate crystalline and atomically flat surface without formation of small islands, characteristic for a layer by layer growth.

Like  $\text{Pr}_{0.5}\text{Ca}_{0.5}\text{MnO}_3$ , STS measurements were done on  $\text{Pr}_{0.7}\text{Ca}_{0.3}\text{MnO}_3$  with the difference that in order to have a good resolution in terms of energy, no lock-in technique has been used. So just the acquisition of the  $I(V)$  curves in each spatial point was performed. The optimized parameters of the measurements were set to  $I_{SET}=1$  nA and  $V_{BIAS}=1.75$  V. Here the voltage bias was set a little above the energy region of interest (-1.5 V to 1.5V) just to avoid the always present artifacts associated with the cancellation of regulation and the start of the voltage ramp. The voltage ramp started at 1.75 V and ended at -1.75 V in 351 points leading to nominal resolution of 10 mV. The usual acquisition time that enables fast but relatively good signal to noise ratio was set to 1 ms per point leading to total acquisition time of more than 3 hours for  $256 \times 128$  px<sup>2</sup> image size. The area presented here was  $256 \times 128$  nm<sup>2</sup> in size, and was sampled in  $256 \times 128$  px<sup>2</sup> leading to nominal spacial resolution of 1 nm. The topographic image obtained during one of the STS measurements is shown in figure 4.21.

To calculate both  $dI/dV$  and  $d \ln I / d \ln V$ , the TVR algorithm is applied to the whole set of data. For further analysis we used  $d \ln I / d \ln V$  based normalization as well as Ukraitsev normalization function to extract interesting parameters such as average work function spatial dependence as well as tip to sample separation spatial dependence. Some of the results are presented below.

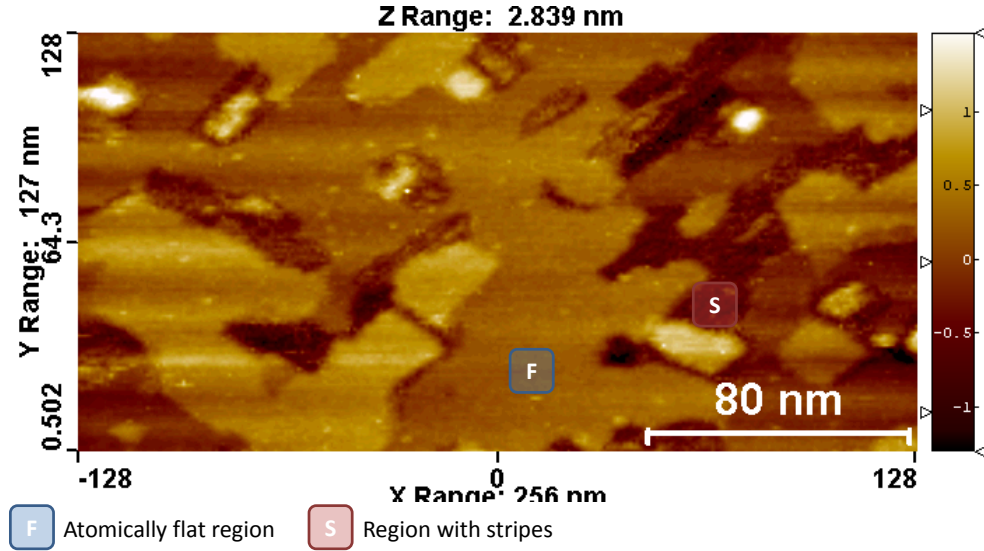


Figure 4.21: The topographic image obtained during STS measurement on PCMO[x=0.3] thin film on STO

The K-means is applied to the  $dI/dV$  normalized data taking into consideration different spectral ranges and assuming different class numbers as shown in figures 4.22 a) and 4.23 a). The ranges indicated on the first image are : the whole spectral range (all), only occupied states (negative) and only unoccupied states (positive). In the second image the same data sets were used, but with the exclusion of the gap region (-0.5 V to 0.5 V). The 2, 3 and 4 class assumption correspond to assigned columns. Corresponding average spectra for each class are also represented in figures 4.22 b) and 4.23 b).

The first thing that can be noticed is that regardless of the data range used for classification, the K-means algorithm for 2 classes always produces more or less the same classification image, the one that is in correlation with the atomically flat (red area in 2 class image) and stripe like areas (blue area in 2 class image). The flat areas are characterized by normalized differential conductance (NDC) that shows conduction peaks at the gap onset and also with the gap value somewhat smaller than that measured on the striped region. The origin of the conductance peaks is often associated with polarons [44] but, as shown in chapter 4.3, their effective presence can be altered or suppressed by the choice of small offset parameter when numerically calculating the NDC. The position of the peaks, on the other hand, is

4. Scanning tunneling spectroscopy on  $\text{Pr}_{1-x}\text{Ca}_x\text{MnO}_3$  thin films

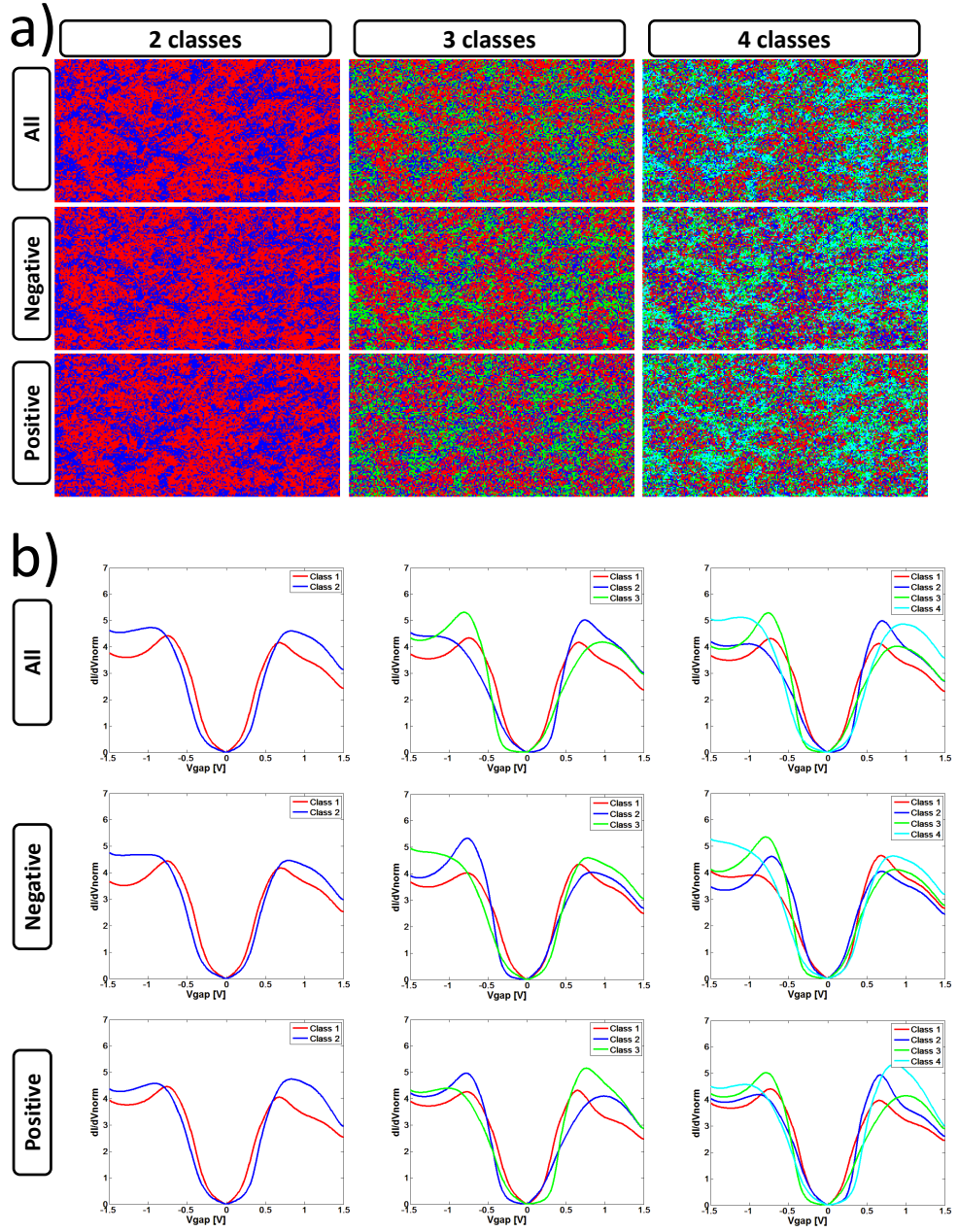


Figure 4.22: a) The result of the k-means classification for 2,3 and 4 assumed classes taking into account whole spectra, only negative voltages and only positive voltages; b) corresponding average spectra for each class shown on a) (the curves and classes are appropriately color coded)

4. Scanning tunneling spectroscopy on  $\text{Pr}_{1-x}\text{Ca}_x\text{MnO}_3$  thin films

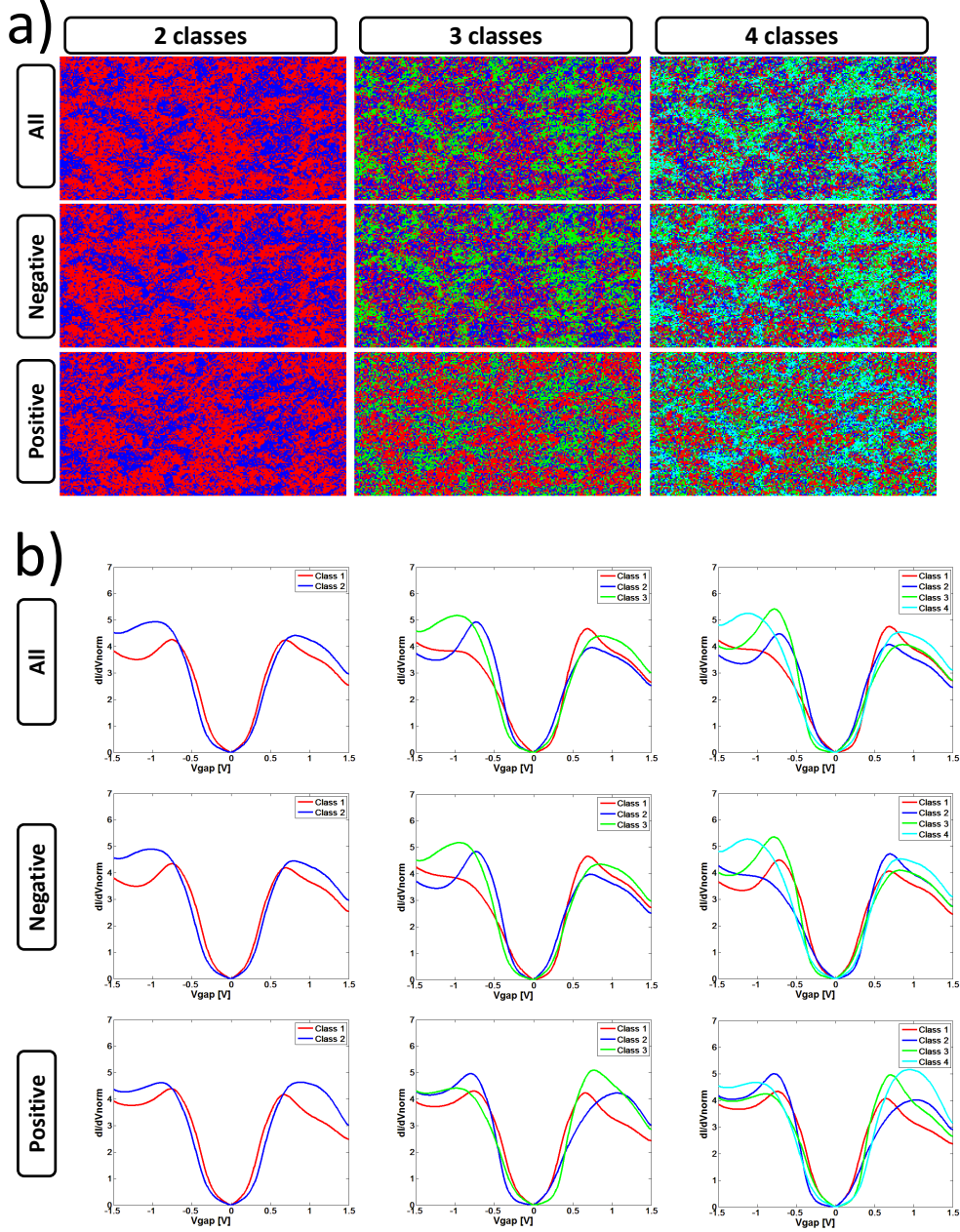


Figure 4.23: a) The result of the k-means classification for 2,3 and 4 assumed classes taking into account whole spectra, only negative voltages and only positive voltages excluding the gap states in each b) corresponding average spectra for each class shown on a) (the curves and classes are appropriately color coded)

not strongly influenced by normalization. One should take care about this if more quantitative conclusions have to be extracted. However, altered or suppressed, their qualitative presence is clearly demonstrated.

The next, more technical, result to be noticed is that, although the whole range spectra classification was able to identify regions of different spectral response and while this was not the case with our  $\text{Pr}_{0.5}\text{Ca}_{0.5}\text{MnO}_3$  measurements (shown on Fig. 4.13), there is similar conclusion emerging from both data sets : excluding the in gap values improves the classification image contrast. The reason for this remains the same, signal to noise ratio in the gap influences the decision making in K-means by moving the spectral point in spectra space away from the corresponding centroid leading to a wrong classification (for details on K-means see chapter 2.3). In the rest of the chapter we will consider only data shown in figure 4.23. Of course if one expects some in-gap features, the gap region should be taken into consideration.

The 3 and 4 classes images and corresponding averaged NDC are still correlated to the topography, but they also allow to identify inhomogeneities in each of the topographical classes (flat and striped one). The flat area predominantly has symmetric conduction peak response<sup>2</sup> while the striped one is slightly asymmetric with more occupied states present. The origin of the asymmetry in STS measurements in strongly correlated systems is often ascribed to the opening of  $d_{z^2}$  conduction channels when applying negative bias voltages to the sample [46]. Unfortunately the spatial resolution in the stripe region does not allow us closer inspection of the asymmetry in this region and it's eventual correlation with the stripes.

To confirm the presence of regions characterized by different gap, a gap-map, obtained from the  $d\ln I/d\ln V$ -V curve (using 0.5 threshold) is presented in 4.24, with corresponding histogram. This map is in agreement with previous 2 class average NDC measurements, showing also the a larger gap (lighter areas) is present in the striped region.

We also used Ukraitsev normalization method but only to extract certain parameters from the fit of normalization function to our experimental data. The average workfunction distribution as well as the tip to sample separation maps and distribution histograms are presented in figures 4.25 and 4.26. A lowering of a work function and slight increase of the tip to sample separation is observed in the striped region.

---

<sup>2</sup>one is advise to pay attention to color code since the same colors do not always represent the same spectral response

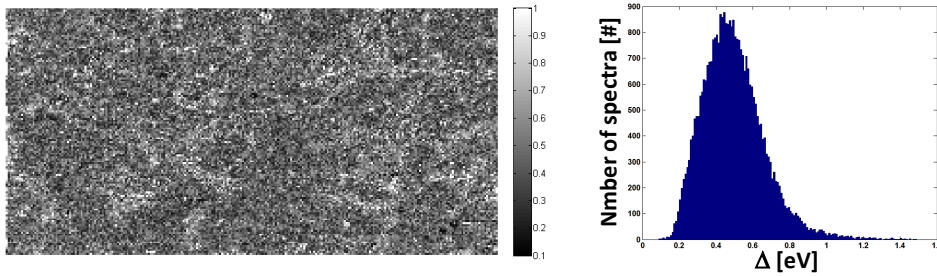


Figure 4.24: Gap map obtained from STS data on PCMO( $x=0.3$ ) (left) and corresponding gap histogram of the gap value distribution.

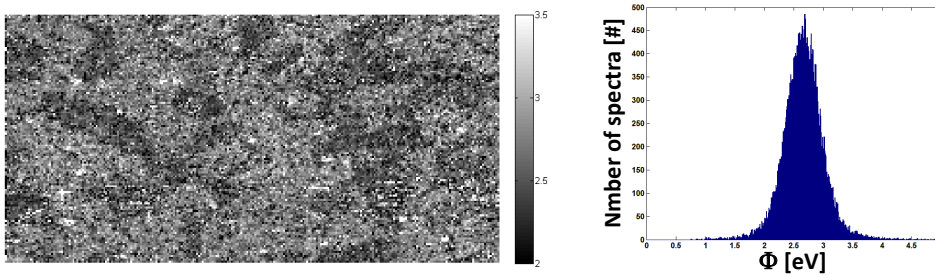


Figure 4.25: Map of average surface potential obtained from STS data on PCMO( $x=0.3$ ) using Ukraitsev tunneling probability function(left) and corresponding  $\Phi$  histogram.

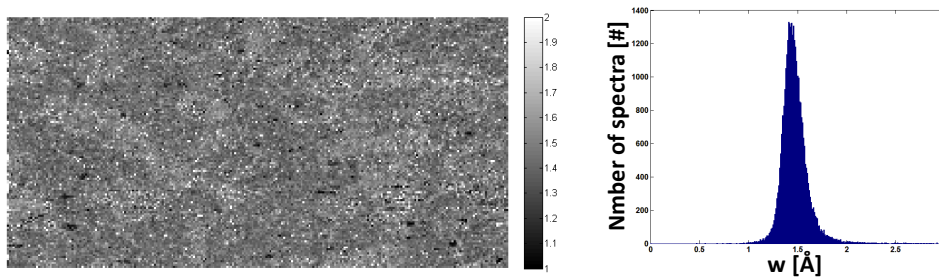


Figure 4.26: Map of tip to surface separation obtained from STS data on PCMO( $x=0.3$ ) using Ukraitsev tunneling probability function(left) and corresponding  $w$  histogram.

### 4.3 Summary

The STM-STS results obtained on  $\text{Pr}_{0.5}\text{Ca}_{0.5}\text{MnO}_3$  and  $\text{Pr}_{0.7}\text{Ca}_{0.3}\text{MnO}_3$ , showed a clear correlation between topographic and electronic properties, but for quite different reasons. In the case of  $\text{Pr}_{0.5}\text{Ca}_{0.5}\text{MnO}_3$  the inhomogeneous response can be associated to different atomic terminations, while in  $\text{Pr}_{0.7}\text{Ca}_{0.3}\text{MnO}_3$  the presence of areas with nano-structured domains (stripes) gives rise to an electronically inhomogeneous response. Also our measurements are, at least judging by the 2 class classification, at odds with the previously mentioned measurements done on manganites (see chapter 3.3). There, the phase separation images and the topographic images were not correlated, at least not on the large scale and not in intermediate-bandwidth manganites. On the other side the measurements done on narrow-bandwidth manganites at the atomic-scale, showed a correlation between the structural (topographical) image and conductance measurements. What we presented here, is the existence of a strong connection between the structure and electronic properties in narrow-bandwidth PCMO manganites on a relatively large scale. This does not exclude the existence of additional phases since we also showed that within topographically determined phases, areas with different spectral responses exist. Both measurements are also in agreement with the polaronic picture: more conducting response associated with termination when no apex oxygen is present (thus no formed octahedra) in the case of  $\text{Pr}_{0.5}\text{Ca}_{0.5}\text{MnO}_3$  and polaron spectroscopic signature in form of conductance peak in flat areas of  $\text{Pr}_{0.7}\text{Ca}_{0.3}\text{MnO}_3$  thin film.

# Chapter 5

## LaAlO<sub>3</sub> on SrTiO<sub>3</sub> 2D electron gas at the interface: Overview

In this chapter the main characteristic of the LaAlO<sub>3</sub>/SrTiO<sub>3</sub> system, more precisely the interface between them, will be discussed. First of all, the two building block elements will be introduced and their general characteristics (structure, electronic properties) presented. In the following section the formation and nature of 2D electron gas at the LaAlO<sub>3</sub>/SrTiO<sub>3</sub> interface will be discussed in the theoretical and experimental framework. Finally a short overview of the results obtained by the application of the SPM techniques on this system will be presented.

### 5.1 LaAlO<sub>3</sub>

LaAlO<sub>3</sub> is a distorted perovskite oxide. At room temperature it's structure is that of a rhombohedral distorted perovskite (space group  $R\bar{3}c$ ) which undergoes a transition to the ideal perovskite structure (space group  $Pm\bar{3}m$ ) at high temperatures above  $\approx 800K$  [47, 48]. The rhombohedral parameters of LaAlO<sub>3</sub> at room temperature are  $a=b=5.36540 \text{ \AA}$ ,  $c=13.11260 \text{ \AA}$  [Fig. 5.1] and the corresponding pseudocubic lattice constant is  $a_{PC}=3.791 \text{ \AA}$ .

The relatively large mismatch of LaAlO<sub>3</sub> pseudocubic lattice parameter to the cubic lattice parameter of SrTiO<sub>3</sub> of 2.92%<sup>1</sup> is thermally sustained by the similar thermal expansion coefficients, making the growth on SrTiO<sub>3</sub> hetero-epitaxial [49, 50].

---

<sup>1</sup>referred to SrTiO<sub>3</sub>

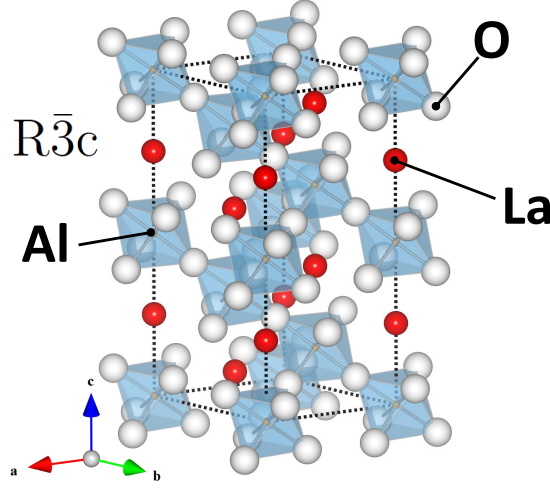


Figure 5.1: Structure of LaAlO<sub>3</sub> -  $R\bar{3}c$  space group at room temperature

Electronically, LaAlO<sub>3</sub> is a band insulator having a wide electronic band gap ( $E_{gap}^{LAO} = 5.6$  eV) [51, 52] and high dielectric constant typical for aluminates ( $\kappa \approx 23.3$ ) [53, 54]. Its electronic structure (as well as the electronic structure of SrTiO<sub>3</sub>) is consistent with the proposed universal band structure for transition metal/rare earth oxide dielectrics [Fig. 5.2 a)] [51, 55], in framework of which the atomic 3d states of La are relatively high in energy, and close to the La atom s-states, while the valence band has main contribution from O 2p states [Fig. 5.2 b)] [51, 52].

Concerning the structural and dielectric properties of LaAlO<sub>3</sub>, it is also interesting to mention that LaAlO<sub>3</sub> lattice is matched to Si(110) [52] and to the lattice of many transition metal oxide compounds, so it is often used as gate material in devices [56]. LaAlO<sub>3</sub> single crystals are also used in oxide electronics as substrate material but not to same extent as SrTiO<sub>3</sub>, due to the presence of twinning domains [53].

## 5.2 SrTiO<sub>3</sub>

SrTiO<sub>3</sub> is a transition metal perovskite oxide with cubic structure at room temperature (space group  $Pm\bar{3}m$ ) and a lattice constant of 3.905 Å (the TiO<sub>6</sub> octahedra have perfect 90° angles [Fig. 5.3.a]). The cubic symmetry is lowered to tetragonal ( $I4/mcm$  space group) when the temperature decreases below 105 K [57].

SrTiO<sub>3</sub> plays an important role as a standard substrate for many oxide materials due to its perfect cubic structure well matched to most of the

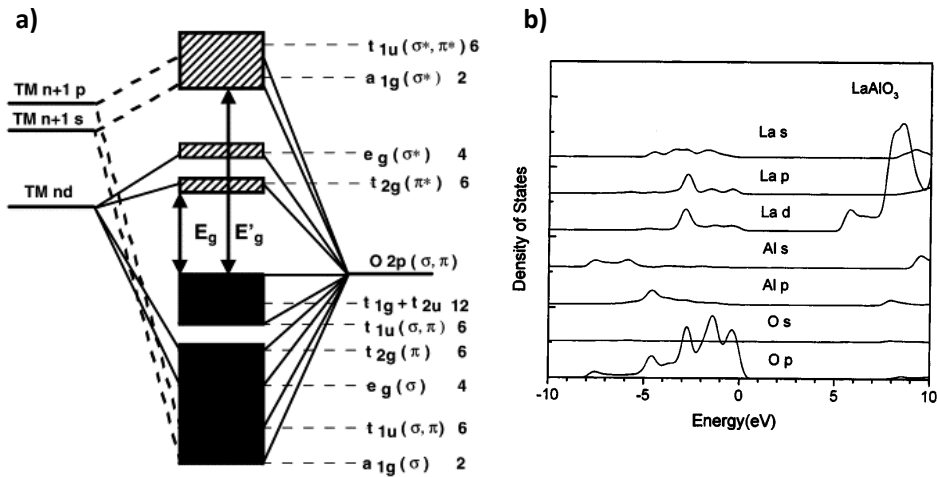


Figure 5.2: a) Universal band structure for transition metal/rare earth oxide dielectrics (as proposed by Lucovsky, Whitten and Zhanga [55]); b) calculated  $\text{LaAlO}_3$  DOS by Peacock and Robertson [52]

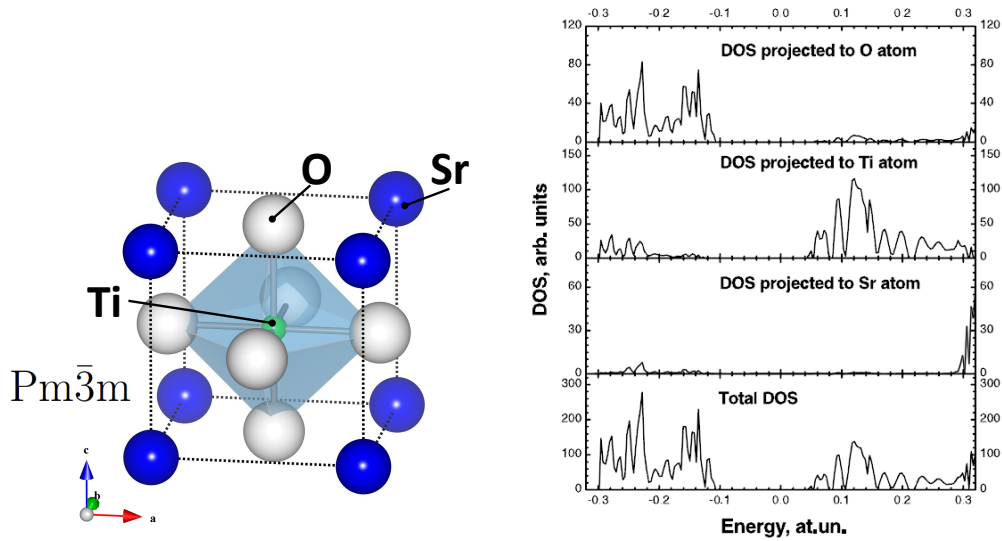


Figure 5.3: a) Structure of  $\text{SrTiO}_3$  -  $\text{Pm}\bar{3}\text{m}$  space group at room temperature; b) Total and projected DOS for bulk  $\text{SrTiO}_3$ . Reproduced from Heifets et al. [58].

perovskite type oxides and allowing epitaxial growth also because of its chemical inertness. Interestingly, from the thin film growth point of view, SrTiO<sub>3</sub> can be easily B-site terminated by chemical etching [59].

Electronically, stoichiometric SrTiO<sub>3</sub> is a band-insulator with a relatively large and indirect band gap of 3.25 eV [58, 60] in agreement with the band diagram of fig, 5.2.a and Fig. 5.3.b. When doped, however, SrTiO<sub>3</sub> can exhibit semiconducting or metallic behavior and, at very low temperatures, of order of 300 mK, superconductivity.

There are few doping mechanisms in SrTiO<sub>3</sub> that influence its electronic properties. We mention two of them:

- n-type doping by introduction of oxygen vacancies [61, 62]. In single crystals the introduction of oxygen vacancies is easily achieved by heating the stoichiometric crystal at temperatures between 800° C and 1200° C in vacuum [61] or by Ar-ion etching [63]. For certain doping levels a superconducting phase appears with critical temperatures  $T_c < 300$  mK [64, 65]. As will be shown later, control of oxygen vacancies level during the deposition process, when SrTiO<sub>3</sub> is used as a substrate and kept at high temperatures, can be of crucial importance for the electronic properties of the system grown.
- doping by substituting small amounts of Sr with La (n-type) [66], Ti with Nb (n-type) [67], or other similar substitutions [62]. Similarly to oxygen vacancies doping, superconductivity in doped SrTiO<sub>3</sub> has been reported [67].

Among other interesting characteristics of SrTiO<sub>3</sub>, it is a quantum paraelectric (a dielectric which approach the ferroelectricity in the limit of zero K) with huge values of dielectric constant at room temperature  $\kappa \approx 300$ , which increases up to 20000 at low temperatures. Its high dielectric constant makes SrTiO<sub>3</sub> a good candidate for gate dielectric in oxide based field effect devices [68]. The possibility to grow ultra-thin film of SrTiO<sub>3</sub> on Si(001) [69] makes application as a gate dielectric in Si-based technologies possible. Although not being ferroelectric in its natural single crystal form, SrTiO<sub>3</sub> can be driven into a ferroelectric state by the application of strain. [70].

### 5.3 LaAlO<sub>3</sub> on SrTiO<sub>3</sub>

The realization of conducting interface between LaAlO<sub>3</sub> and SrTiO<sub>3</sub>, came to the attention of the scientific community after the work of A. Ohtomo

and H.Y. Hwang from Bell Labs (USA) [71, 72]. Investigating polarity discontinuities in oxides they showed, for the first time, that a 2D electron gas is created at the interface between two band oxide insulators. The need to understand the origin of this conductive and confined state, and the promise of new functionality between the interfaces of strongly correlated materials, initiated a lot of theoretical and experimental research on this system.

In their study A. Ohtomo and H.Y. Hwang deposited heterostructures of thin films of  $\text{LaAlO}_3$  and  $\text{SrTiO}_3$  by pulsed laser deposition (PLD) and analyzed two interface type combination:

- the  $(\text{AlO}_2:\text{SrO})$  interface, obtained by depositing  $\text{LaAlO}_3$  on A-site terminated  $\text{SrTiO}_3$  [Fig. 5.4 a)];
- the  $(\text{LaO}:\text{TiO}_2)$  interface, obtained by depositing  $\text{LaAlO}_3$  on B-site terminated  $\text{SrTiO}_3$  [Fig. 5.4 b)].

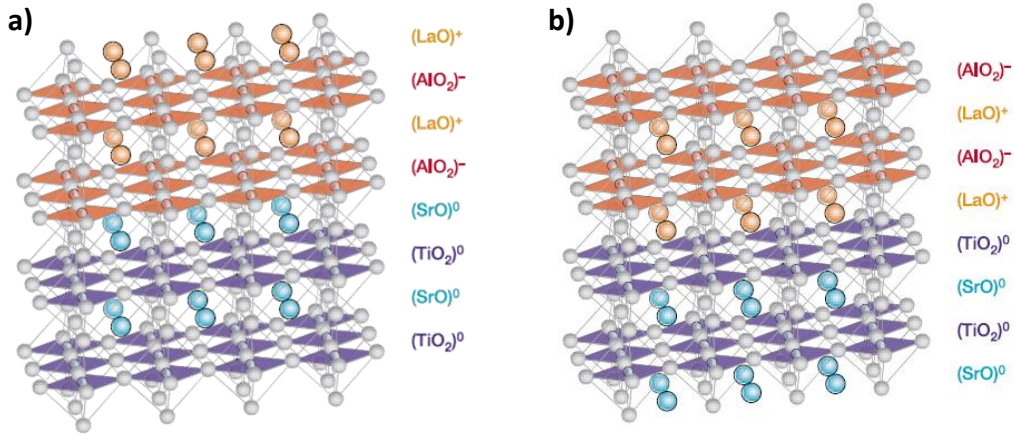


Figure 5.4: Two possible  $\text{LaAlO}_3/\text{SrTiO}_3$  interfaces a)  $\text{LaAlO}_3$  grown on SrO (A-site) terminated  $\text{SrTiO}_3$  -  $\text{LaAlO}_3/\text{SrTiO}_3:\text{SrO}$ ; b)  $\text{LaAlO}_3$  grown on  $\text{TiO}_2$  (B-site) terminated  $\text{SrTiO}_3$  -  $\text{LaAlO}_3/\text{SrTiO}_3:\text{TiO}_2$ . Reproduced from Ohtomo and Hwang [71]

They found that the  $\text{AlO}_2:\text{SrO}$  system [Fig.5.4 a)] exhibits insulating behavior while  $\text{LaO}:\text{TiO}_2$  interface was conducting [Fig.5.4.b] with high carrier mobility (greater than  $10000 \text{ cm}^2\text{V}^{-1}\text{s}^{-1}$  at low temperatures) possibly associated to the formation of a 2D electron gas.

In the  $\text{LaAlO}_3(001)/\text{SrTiO}_3(001)$  system, it turns out, that a polar discontinuity occurs at the interface independent of the stacking sequence. This is due to the fact that while  $\text{SrTiO}_3$  is composed of  $[\text{Sr}^{2+}\text{O}^{2-}]^0$  and

## 5. LaAlO<sub>3</sub> on SrTiO<sub>3</sub> - 2D electron gas at the interface: Overview

[Ti<sup>4+</sup>O<sub>2</sub><sup>2-</sup>]<sup>0</sup> neutral layers, LaAlO<sub>3</sub> is polar in the (001) direction and composed of [La<sup>3+</sup>O<sub>2</sub><sup>-</sup>]<sup>+</sup> and [Al<sup>3+</sup>O<sub>2</sub><sup>2-</sup>]<sup>-</sup> charged atomic planes. In both cases, charged layers are stacked on a non-polar surface, leading to the realization of electric dipoles and to an electric field distribution such that a divergence of the potential is expected when LaAlO<sub>3</sub> unit cells are added. Of course this picture is energetically unfavorable as shown in Fig. 5.5. This scenario is often referred to as "polar catastrophe".

From the previous studies, done on system with polar discontinuities that involved semiconducting hetero-junctions of structurally almost perfectly matched crystals like Ge (nonpolar) and GaAs (polar) [73, 74], it was known that to avoid the polar catastrophe, a structural or chemical redistribution of the atoms at the surfaces and interfaces has to take place, resulting on different possible phenomena, like interface roughening, surface or interface reconstructions, and cationic mixing. Nakagawa et al. [75] proposed, in the case of LaAlO<sub>3</sub>/SrTiO<sub>3</sub> interface, another possible mechanism for compensating the polar discontinuity, the so called electronic reconstruction. For correlated materials, the electronic reconstruction means redistribution of parameters governing electronic properties of the material (interaction strengths, bandwidths and electron densities) [14, 76].

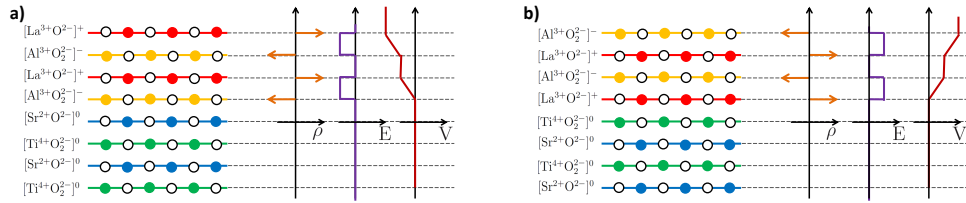


Figure 5.5: Charge, field and potential distribution for two possible LaAlO<sub>3</sub>/SrTiO<sub>3</sub> interfaces a) LaAlO<sub>3</sub>/SrTiO<sub>3</sub>:SrO; b) LaAlO<sub>3</sub>/SrTiO<sub>3</sub>:TiO<sub>2</sub>.

In this framework the ability of Ti ion to host two different valences is crucial. Two valences of Ti are that of Ti<sup>4+</sup> present in the SrTiO<sub>3</sub> compound, where 3d states of Ti are empty, and the other possible valence is that of Ti<sup>3+</sup> present in the LaTiO<sub>3</sub> compound, where one electron occupies the Ti 3d shell. Since surrounded by O<sub>6</sub> octahedra, and as mentioned in section 3.2 for materials with cubic structure, Ti 3d states have a lifted degeneration, with *t<sub>2g</sub>* states being lower in energy than that of *e<sub>g</sub>*. In the case of LaAlO<sub>3</sub>/SrTiO<sub>3</sub>, the proposed electronic reconstruction mechanism is presented in figure 5.6. In the case of conducting n-type LaO:TiO<sub>2</sub> interface, half electron per 2D unit cell transferred to the TiO<sub>2</sub> layer, is sufficient to compensate the polar catastrophe while still accommodating polar planes

in the bulk. Nakagawa et al. [75] approach started from the assumption of charged  $\text{LaO}$  and  $\text{AlO}_2$  layers with  $\text{LaO}$  layers donating half of electron ( $e/2$ ) per 2D unit cell to the neighbor layers (in the  $c$ -direction), effectively filling  $t_{2g}$  states of  $\text{Ti}$  with electrons transferred from the surface, causing the appearance of a mixed valence state composed of half  $\text{Ti}^{4+}$  and half  $\text{Ti}^{3+}$  ions. In the same framework, i. e.  $\text{LaO}$  donating  $e/2$  electrons to neighbor layers in the case of an  $\text{AlO}_2:\text{SrO}$  termination, the  $\text{SrO}$  layer would be doped by half hole per 2D unit cell, that should also make it conductive.

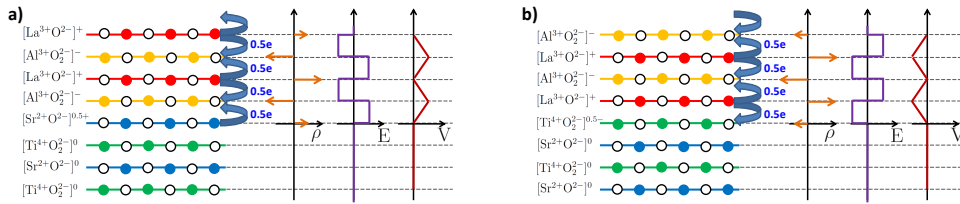


Figure 5.6: Charge, field and potential distribution for two possible  $\text{LaAlO}_3/\text{SrTiO}_3$  electronically reconstructed interfaces a)  $\text{LaAlO}_3/\text{SrTiO}_3:\text{SrO}$ ; b)  $\text{LaAlO}_3/\text{SrTiO}_3:\text{TiO}_2$ .

Although the importance of electronic reconstruction was recognized, other mechanisms has to be included to fully address the experimental results emerged during the years.

In early theoretical papers the role that  $\text{SrTiO}_3$  termination on the final electronic state of the system was addressed. The fact that the  $\text{AlO}_2:\text{SrO}$  layer is not conductive was very soon recognized as a result contradicting the polar catastrophe scenario. To justify this experimental finding, Nakagawa et al. proposed that instead of electronic reconstruction, a rearrangement of oxygen vacancies at the interface, compensating the polar discontinuity, was energetically more favorable in the case of the  $\text{AlO}_2:\text{SrO}$  interface. In addition to the oxygen compensation, Pentcheva et al. [77] proposed that disproportionated, charge-, orbital-, and spin-ordered O 2p magnetic hole is formed, resulting in small hole polaron crystal formation that results in an insulating phase. What is the exact mechanism that leads to insulating phase is yet not clearly defined.

As for the origin of a 2D electron gas, at the n-type  $\text{LaO}:\text{TiO}_2$  interface there is a general agreement in theoretical papers that a mixed valence phase is occurring at the interface [77–80]. It is also agreed that on-site correlations should have an important role, since the interface itself has the stoichiometry of  $\text{LaTiO}_3$ , known to be a Mott-insulator but with semiconducting behavior [81, 82]. Using the LDA+U method, Pentcheva et al. [77] proposed that

ferromagnetic check-board like charge and orbital ordering is taking place at the interface, with Ti  $t_{2g}$  additionally split with  $d_{xy}$  states being more favorable (lower in energy) than  $d_{yz}$  and  $d_{xz}$  states, as shown in figure 5.7. As we mentioned in chapter 3.2 the charge order phase is usually associated with insulating behavior, at odds with high conductivity measured in this systems. Pentcheva et al. argued that with half the Ti sites empty, hopping to neighboring sites will be a frequent process even at relatively low temperature due to the more pronounced fluctuation effects in two dimension than in three. This site-centered picture has yet to be experimentally confirmed.

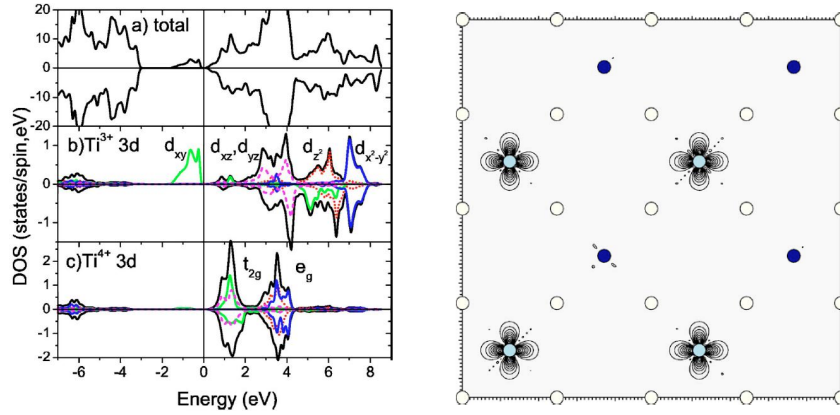


Figure 5.7: (left) Density of states of the n-type interface: a) total; b) d states of magnetic Ti<sup>3+</sup> showing the split-off majority  $d_{xy}$  band, with the corresponding minority states lying at +5 eV; the other 3d states are not strongly polarized; c) the nonmagnetic Ti<sup>4+</sup> ion, showing the conventional although not perfect  $t_{2g}$ - $e_g$  crystal field splitting.  $d_{xy}$  orbitals are marked by a green light gray line,  $d_{xz}$  and  $d_{yz}$  states by a magenta dashed line, states with  $d_{z^2}$  and  $d_{x^2-y^2}$  character by a red dotted and blue dark gray solid lines, respectively. (right) Proposed charge and orbital ordered state at the interface

The other problem needed to be addressed is that, in the proposed framework, only a single layer of LaAlO<sub>3</sub> would lead to a conducting behavior. In the bilayer configuration, however, as it is shown by Thiel et al. [Fig. 5.8 a)] [83], there exist a critical thickness of 3 u.c. of LaAlO<sub>3</sub> grown on TiO<sub>2</sub> terminated SrTiO<sub>3</sub> above which the 2D electron gas appears. The only theoretical paper, to our knowledge, that treats thin n-type LaAlO<sub>3</sub> film on SrTiO<sub>3</sub> is that of Pentcheva et al.[84] predicting a critical thickness of 5 u.c. To address this problem Pentcheva et al. showed, using generalized gradient approximation with included correlations (GGA+U), that a strong lattice

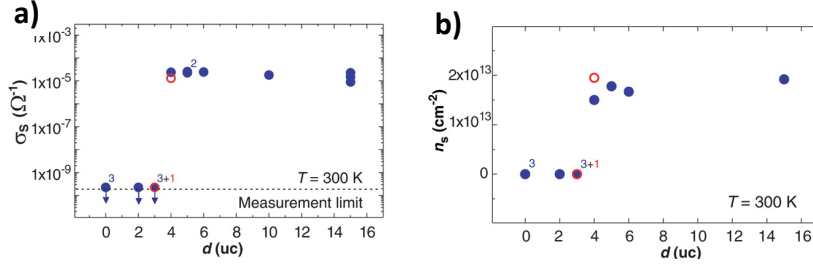


Figure 5.8: a) The conductance threshold thickness was found to be 3 u.c. in  $\text{LaAlO}_3/\text{SrTiO}_3:\text{TiO}_2$  system by Thiel et al. [83]

polarization compensates the dipolar electric field responsible for potential divergence, sustaining the insulating behavior up to certain critical thickness [84]. In figure 5.9 the total DOS and layer-resolved DOS for n-type system are shown. A gradual collapse of the band gap with the increase of the  $\text{LaAlO}_3$  thickness from 1 u.c. to 5 u.c., due to the strong lattice polarization in  $\text{LaAlO}_3$  layer, is shown, giving rise to an electronic reconstruction as the system approaches the limit of the isolated interface. The effect of this polar distortion is crucial since, without it, the system is metallic for any coverage of  $\text{LaAlO}_3$ . In this frame, a band gap in the relaxed systems is formed between two spatially separated bands: conductive Ti 3d (or more precisely  $d_{xy}$ ) band at the interface and valence of O 2p band at the surface layer.

We mention here the x-ray absorption spectroscopy (XAS) measurements that were performed on the samples studied in this thesis, that address both the critical thickness and the eventual orbital ordering at  $\text{LaAlO}_3/\text{SrTiO}_3$  [85]. XAS is a technique in which x-ray photons excite core electrons to the unoccupied states of the solid, thus providing an orbital resolved measurement of the unoccupied 3d states of Titanium at the interface. A comparison among experimental and calculated  $\text{SrTiO}_3$  absorption spectra ( $\text{Ti}^{4+}$  valence) and experimental  $\text{LaTiO}_3$  ( $\text{Ti}^{3+}$  valence) [Fig. 5.10 b)], showed very different spectral responses. When experimental data obtained on 4 u.c. n-type  $\text{LaAlO}_3/\text{SrTiO}_3$  bilayer were modeled with a monolayer of  $\text{La}_x\text{Sr}_{1-x}\text{TiO}_3$  no good fit could be obtained, indicating that limited cation mixing is present at the interface and also that there is no detectable occupancy of localized 3d  $\text{Ti}^{3+}$  states, at odds with mixed valence site-centered picture of charge order. Rather some kind of covalent, bond-centered, distribution is present, not excluding possible orbital ordering [Fig. 5.10 c)].

Also, linear dichroism (LD), a difference of spectral response for out of plane and in plane polarized x-ray beam, was obtained for different film thicknesses. Different polarizations favor different orbital orientations: in

5.  $\text{LaAlO}_3$  on  $\text{SrTiO}_3$  - 2D electron gas at the interface: Overview

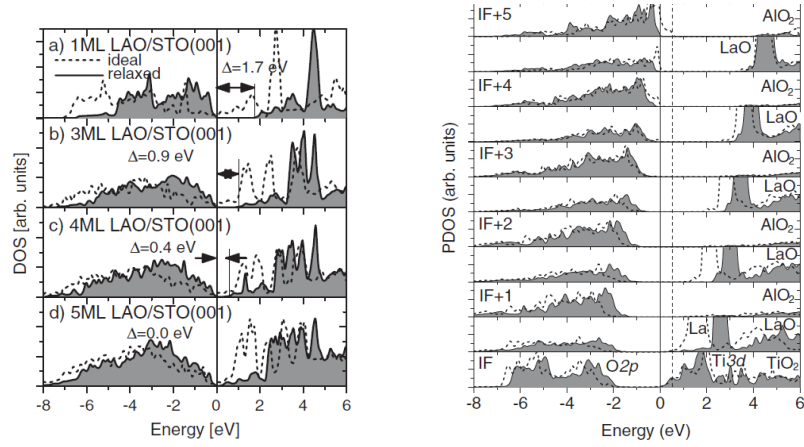


Figure 5.9: (Left) Density of states for the ideal (dashed line) and relaxed (solid line, grey filling) structure of 1–5 ML LAO on STO(001). The relaxation opens a band gap, but its size decreases with each added LAO layer. (Right) Layer-resolved density of states of 5 ML LAO on STO (001) with ideal (dashed line) and relaxed (grey shaded area) coordinates. The DOS for the ideal positions was shifted by 0.5 eV to align with the conduction band of the system with the relaxed atomic positions. Its Fermi level is marked with a dashed line. Reproduced from [84]

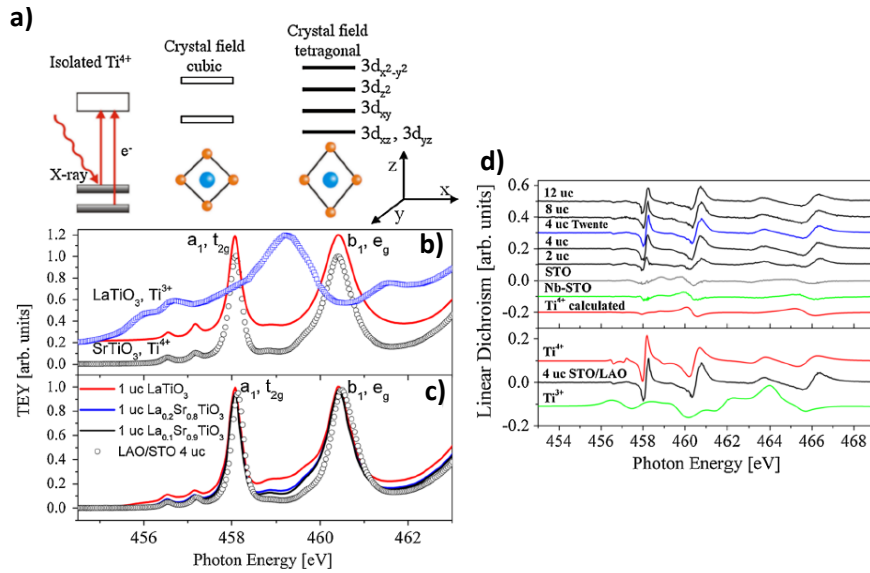


Figure 5.10: Results of XAS measurements . Reproduced from Salluzzo et al.[85]

plane polarization (ab) probing  $d_{xy}$  and  $d_{x^2-y^2}$  while out of plane one (c) probing  $d_{xz}$ ,  $d_{yz}$  and  $d_{z^2}$ . Results on figure 5.10 clearly show the rise of the LD signal when critical thickness of 4 u.c. is reached. The strength of the LD is related to the distortion of TiO<sub>6</sub> octahedra indicating that together with electronic reconstruction, orbital reconstruction take place as well, since the structural distortion of the ligand octahedra leads to rearrangement of d-type orbitals in energy as discussed in chapter 3.1.1. This results are best matched by assuming an interface composed of at least 90% of Ti<sup>4+</sup> ions characterized by in-plane  $d_{xy}$  and  $d_{x^2-y^2}$  orbitals having smaller energy than the out-of-plane  $d_{xz}$ ,  $d_{yz}$  and  $d_{z^2}$  orbitals by 50 and 100 meV, respectively.

From all above mentioned theoretical and experimental results, the lifting of degeneration of Ti  $t_{2g}$  and  $e_g$  states, favoring the occupation of in plane states, can be concluded.

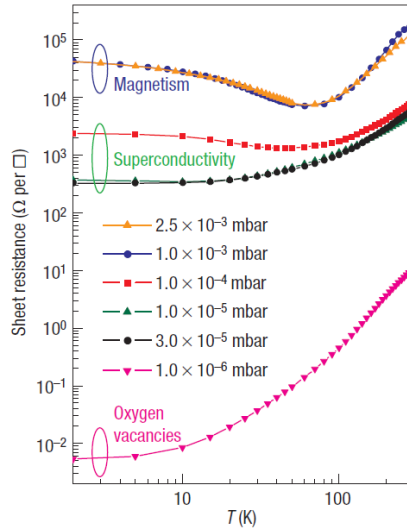


Figure 5.11: The role of the oxygen pressure used during the deposition on the final state of LaAlO<sub>3</sub>/SrTiO<sub>3</sub>:TiO<sub>2</sub>(001) interface . Reproduced from Rijnders(Brinkman)[86, 87].

That electronic reconstruction mechanism is not the only one contributing to novel properties of the interface, and that deposition condition, namely oxygen partial pressure during deposition plays important role in determining the final state of the interface was shown by Brinkman [87]. The deposition oxygen partial pressure is strongly connected to the concentration of oxygen vacancies in SrTiO<sub>3</sub>, thus influencing electronic properties of the substrate and the grown system. Brinkman et al. identified three regions, in sense of the value of deposition oxygen pressure that leads to different electronic and

## 5. LaAlO<sub>3</sub> on SrTiO<sub>3</sub> - 2D electron gas at the interface: Overview

magnetic properties of LaAlO<sub>3</sub>/SrTiO<sub>3</sub>:TiO<sub>2</sub> interface [Fig. 5.11]:

- for the low deposition pressures when  $p_{O_2} \leq 10^{-6}$  mbar the high conductivity is measured [71];
- for intermediate pressures  $10^{-5}$  mbar  $\leq p_{O_2} \leq 10^{-4}$  mbar the superconductivity emerges [88, 89];
- for intermediate pressures  $10^{-3}$  mbar  $\leq p_{O_2}$  the insulating and magnetic behavior appears [87].

This data clearly show that oxygen vacancies can not be ruled out when addressing the electronic properties of the interface, but they also do confirm the role of electronic reconstruction since the conducting state is always present, even at high oxygen partial pressure.

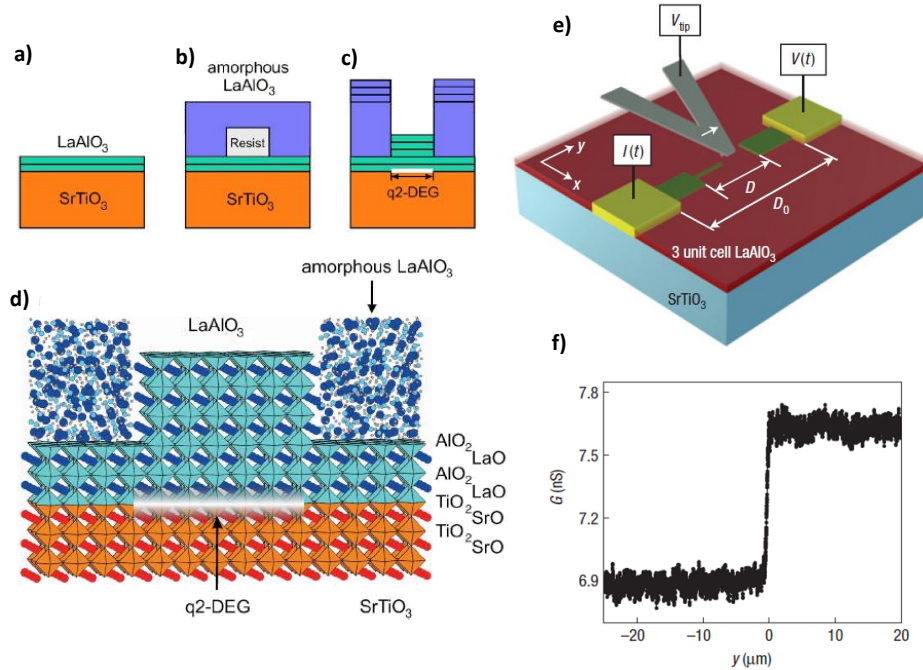


Figure 5.12: a-d) patterning technique for fabricating all LAO/STO device; e) Schematics of the AFM patterning experiment where positively biased AFM tip "writes" the conductive line at the interface of 3 u.c. thin film f) the change in channel conductance as the tip reaches second electrode.

Finally n-type LaAlO<sub>3</sub>/SrTiO<sub>3</sub> interface was found to have potential for application and realization of all-oxide devices. Here the two approach of

constructing LaAlO<sub>3</sub>/SrTiO<sub>3</sub> devices will be illustrated. Both of them use the existence of above mentioned critical thickness of the LaAlO<sub>3</sub> film of 3u.c. Film thinner than 3 u.c. are insulating while that of 4 u.c. and more are conducting and, as shown by Thiel et al. [83], film of 3 u.c. thickness can be switched from insulating into conducting phase by electric field induced electron doping of the interface.

The first approach in building the LaAlO<sub>3</sub>/SrTiO<sub>3</sub> device, uses the patterning technique proposed by Schneider et al. [90] that enables patterning the 2D electron gas by modulating the thickness of the LaAlO<sub>3</sub> layers with unit cell resolution [Fig. 5.12 a-d)]. The other approach is that of Cen [91, 92] where biased conductive atomic force microscopy tip is 'writing' (positive bias) or 'erasing' (negative bias) nanoscale conducting regions in 3 u.c. LAO overlayers on SrTiO<sub>3</sub>(001) [Fig. 5.12]. In the later case, the change of the conducting properties to the removing of the oxygen ('writing') and facilitating adsorption of oxygen or other anions (erasing) from the surface by the AFM tip. This is interesting because it stresses again the role of the surface in the thin layer limit.

## 5.4 SPM/STS measurements on LaAlO<sub>3</sub>/SrTiO<sub>3</sub> interface

Investigation of buried interfaces, like the one of LaAlO<sub>3</sub> on SrTiO<sub>3</sub>, by the SPM probe was usually done in cross section mode, a mode when the tip is parallel rather than perpendicular to the investigating interface, and probing the in plane transport properties of the interface. The challenge in this approach is that it requires a complex sample preparation and cannot be done *in situ*.

For this system in particular there is another obstacle making the interface unreachable to standard cross-section STM: although the interface itself is conducting the SrTiO<sub>3</sub> and LaAlO<sub>3</sub> are not, thus making the tunneling impossible. To probe this interface electronic properties in cross-section configuration the conducting atomic force microscopy was used [Fig. 5.13.a)] by Basletic et al. [93]. They showed that conductivity was confined within 7 nm from the interface as shown in figure 5.13. This result was important since it presented a direct observation and confirmation of confined state at this system.

The only STM/STS measurements on LaAlO<sub>3</sub>/SrTiO<sub>3</sub> we are aware of and that are done in perpendicular geometry are that of Breitschaft et al. [94]. They are done in UHV and low temperatures (4.7 K) on 4 u.c.

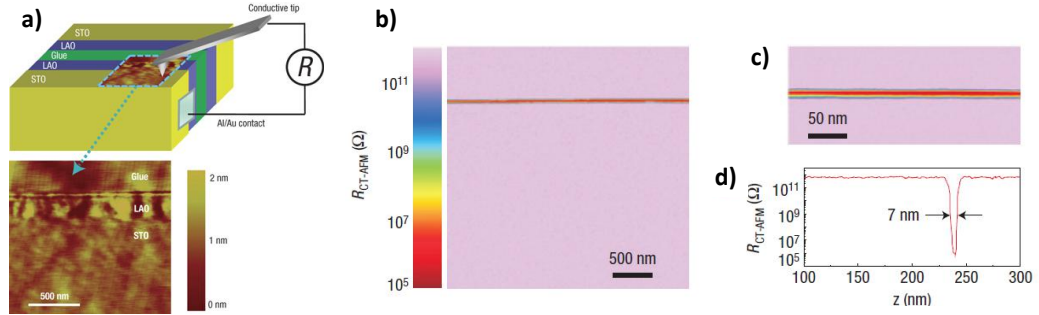


Figure 5.13: a) Schematic of cross-section C-AFM; b) resistance map obtained at the interface; c) detail from b.; d) resistance profile over interface showing less than 7 nm conducting interface

LAO/STO sample, probing the unoccupied states of the system. Rather than standard STM implementation the more sophisticated tuning-fork STM setup is used observing the surface both in AFM like and pure STM mode. The goal of this measurements was not to obtain the spatial spectroscopic map but to probe the electronic response of the interface at low temperatures hoping to observe the effect of eventual correlation on electronic properties by comparing the measured spectra with local density approximation (LDA) and LDA+U (LDA with on site correlation included) calculations. The STS measurements were able to reproduce all characteristic peaks predicted by theory. This result is also interesting because the states in calculated LDA+U are of  $(d_{xz}+d_{yz})$  and  $d_{xy}$  nature with  $d_{xy}$  being lowest in energy that is in agreement with orbital reconstruction picture.

## 5.5 Summary

In this chapter the main characteristic of the  $\text{LaAlO}_3/\text{SrTiO}_3$  system were introduced and a short overview of the results obtained in last years on this system was given. The n-type and p-type draw attention governed by a large potential for fundamental physics but also for the possible application when n-type  $\text{LaAlO}_3/\text{SrTiO}_3$  interface is considered. There have been only few STM/STS studies of the system primarily because of the buried interface geometry.

# Chapter 6

## Scanning tunneling spectroscopy on $\text{LaAlO}_3$ on $\text{SrTiO}_3$ systems

### 6.1 Tunneling through insulating barrier

Investigating the surface properties with STM and STS technique is routinely done if the material is conductive enough. Probing insulating material is, on the other hand, a very different task. One of the approaches that have led to successful observation of the insulating material surface is done on very thin insulating structures on conducting substrate [95, 96]. In the Viernow et al. paper [97] it is shown that by tuning the bias voltage, one is able to select what material he wants to probe: insulating structures or the conductive buried interface [Fig. 6.1 left]. Working with low bias voltages the probed states are one of the conductor, since, for the insulator, there are no states around the Fermi level located in the gap. By increasing the bias voltage above the value corresponding to the conduction band minimum (CBM) of the insulating over-layer (the difference between conduction band minimum energy and Fermi level of the insulator), one is starting to probe the states of the insulator rather than the conductor. However, to be able to perform STM measurements, the transferred charge should be removed from the insulator. Here the geometry of the insulator becomes important. Since for thick insulator films there is no conducting path to effectively remove the transferred charge, the potential of the surface slowly increases (or decreases) towards the tip, eventually leading to a tip-sample crash. If the insulator is in the form of very thin film or very thin islands, thinner than the free electron path, and if the underneath surface is conducting, there is

no charging effect taking place and hence no change in the surface potential, making the STM measurement possible. Of course the working current have to be small enough to allow the effective removal of the charge.

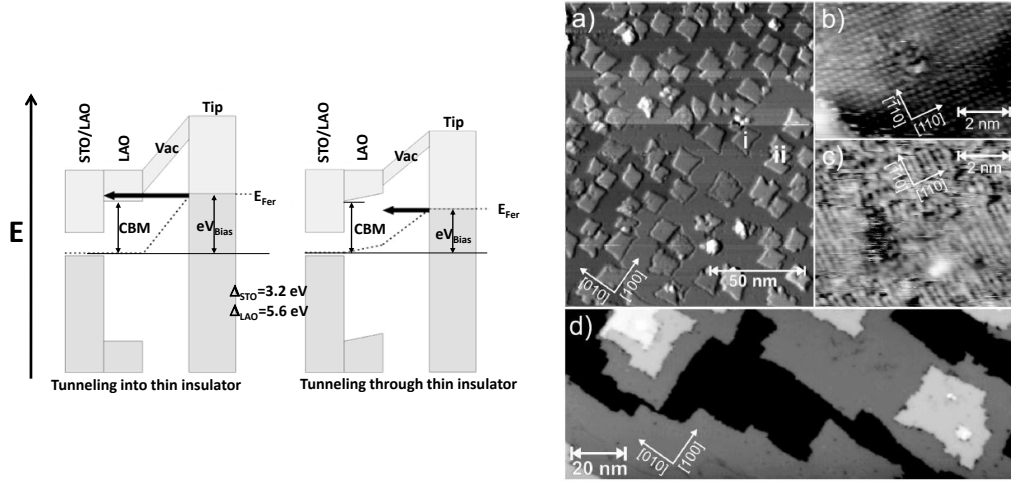


Figure 6.1: (left) The schematic energy diagrams associated with tunneling through insulating barrier in two modes; (right) The experimental results obtained on MgO insulating islands grown on Ag(001): a) the image obtained working above CBM on 0.3 mono layer of MgO on Ag ( $V_{BIAS}=5\text{ V}$  ;  $I_{SET}=1\text{ nA}$ ), b) atomic resolution obtained on Ag through MgO ( $V_{BIAS}=30\text{ mV}$  ;  $I_{SET}=2\text{ pA}$ ), c) atomic resolution obtained on MgO when working above CBM ( $V_{BIAS}=2.5\text{ V}$  ;  $I_{SET}=50\text{ pA}$ ), d) 2 monolayer MgO on Ag ( $V_{BIAS}=3\text{ V}$  ;  $I_{SET}=1\text{ nA}$ )

Another example of the selective nature of STM in probing insulating/conductive systems, is presented by Schintke [96] in the case of MgO islands grown on Ag(001) [Fig. 6.1 right]. By using the selectivity of the STM, i.e. tuning the bias voltage above or below the CBM of the insulator and setting the proper current, either insulating surface or the conductive substrate were observed with atomic resolution at low temperatures. It was also demonstrated that even a 2 monolayer thick MgO film, fully covering the conducting substrate was imaged in the regime above the CBM.

In the case of the  $\text{LaAlO}_3/\text{SrTiO}_3$  system, one is interested to study the buried conducting interface, rather than the  $\text{LaAlO}_3$  insulating surface. Doing this with STM is possible only if following conditions are fulfilled:

- the interface probed is metallic or conductive enough to efficiently transfer charge

- The LaAlO<sub>3</sub> thin film is thin enough and comparable with typical vacuum barrier thicknesses (usually of the order of few nanometers)
- the bias voltage is below the CBM value. This is very important since as mentioned earlier in thin film configuration it is also possible to measure the insulator surface rather than interface
- working currents have to be small enough. This condition is needed to be sure that the tip is not in contact with the insulator and the charge is efficiently removed to the ground.

When STS measurements are considered, one could consider a regime in which the tip is stabilized above the CBM. Indeed I(V) spectroscopy will probe, around the Fermi level, only the conductive interface. The problem with this approach is that the tip working z-position would be such that the contribution of the interface signal would be negligible, due to the exponential nature of tunneling current as function of the tunneling barrier thickness.

The thinnest LaAlO<sub>3</sub>/SrTiO<sub>3</sub> system that fulfills conductivity criteria is one of 4 u.c. (1.5 nm thickness) and it will be the structure primarily studied and analyzed in this thesis. We will also report measurements on 2 u.c. LAO/STO under illumination and we will show that there is a photo-doping mechanism inducing conductivity in this configuration. Although the photo-conductivity effect, was already observed in 3 u.c. LaAlO<sub>3</sub>/SrTiO<sub>3</sub> samples, to our knowledge no transport measurement on 2 u.c. were done in this view, since it shows strongly insulating properties by standard transport measurements.

## 6.2 4 u.c. LaAlO<sub>3</sub> on SrTiO<sub>3</sub>

As mentioned earlier, the minimum thickness of LaAlO<sub>3</sub> film that leads to the formation of a conducting interface is that of 4 u.c. The total thickness of the film of  $\approx 1.5$  nm, so of the order of typical tip to sample separation distances with standard STM experiments done on conductive surfaces and with vacuum barrier. Although critical, we will demonstrate the ability to tunnel to the interface of this system by using very small currents (less than one pA) and bias voltages (less than  $\pm 1$ V) at room temperature.

The 4 u.c. LaAlO<sub>3</sub>/SrTiO<sub>3</sub> samples studied were grown by Prof. Jochen Mannhart group in Augsburg, one of the leading groups in producing and researching the LaAlO<sub>3</sub>/SrTiO<sub>3</sub> system. The analyzed samples were deposited at an oxygen pressure of  $8 \times 10^{-5}$  mbar and 780° C with a laser fluency of 1.0 Joule cm<sup>-2</sup> and were oxygenated in situ at an oxygen pressure of 0.5 bar to

reduce the oxygen vacancies. About details on the growth parameters and the procedure used for producing optimized samples, one is referred to the chapter 3 of the Stefan Patrick Thiel PhD thesis [68].

Transport measurement done on the 4 u.c. sample were in agreement with the expected conducting behavior of the interface while the 2.u.c was insulating to the extent that it was impossible to measure its resistive properties even at room temperature.

Since our measurements were not done *in situ*, a initial cleaning of the samples by rinsing them in propylene was done prior the introduction into the UHV system. Each sample were  $5 \times 5 \times 0.5 \text{ mm}^3$  in size and have gold contacts at the corners. The contacts are deposited onto the interface, thus providing a conductive path to the interface itself. The gold contacts are also grounded by application of small amount of silver paste at their edges. This is important since our configuration is tip biased, thus the interface has to be grounded.

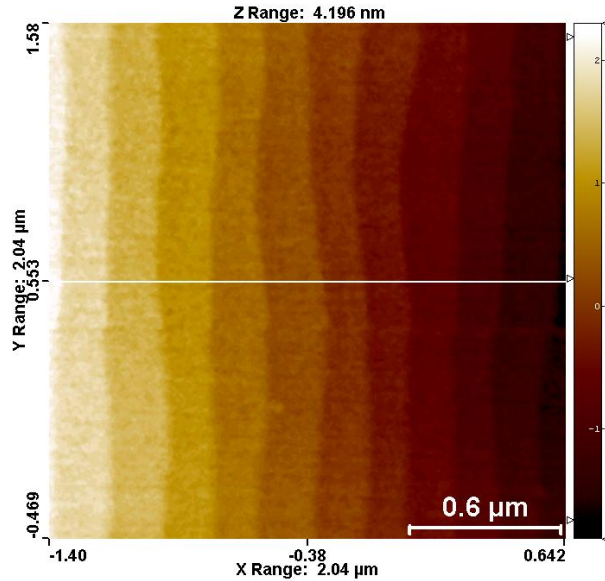


Figure 6.2: C-AFM image of LaAlO<sub>3</sub>/SrTiO<sub>3</sub> 4 u.c. thin film surface

Prior to STM, contact AFM (C-AFM) measurements were done to confirm the morphological state of the surface. Typical large scale topographic image obtained by C-AFM is presented in figure 6.2 with corresponding step-edge profile and image histogram in 6.3. As expected the single terminated film is characterized by  $3.8 \pm 0.2 \text{ \AA}$  step edges.

To probe the surface, an Ir tip obtained with electrochemical etching was used. To be able to get stable tunneling conditions we had to improve the

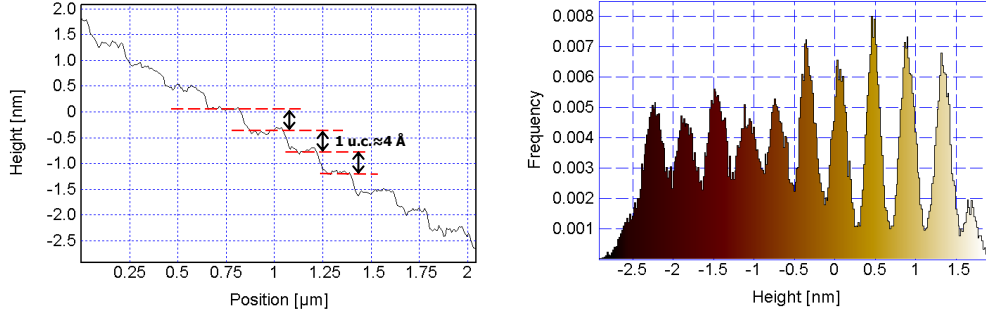


Figure 6.3: Step edge profile (left) and corresponding height histogram distribution (right) for the C-AFM measurement presented on Fig. 6.2

work function and the tip sharpness, we used a classical procedure, consisting in fast approaching the tip to the gold surface while applying short (10 ms-100 ms) -10 V pulses. We checked the tip condition after each of this procedure, by performing topographic and  $I(z)$  measurements on gold. Typical gold granular type topographic image are obtained [Fig. 6.4 a)]. The  $I(z)$  curve on the other hand, show the classical exponential characteristic (at level of order per few  $\text{\AA}$ ) proving in that way that we are having sharp tip and that we are in tunneling regime [Fig. 6.4 b)].

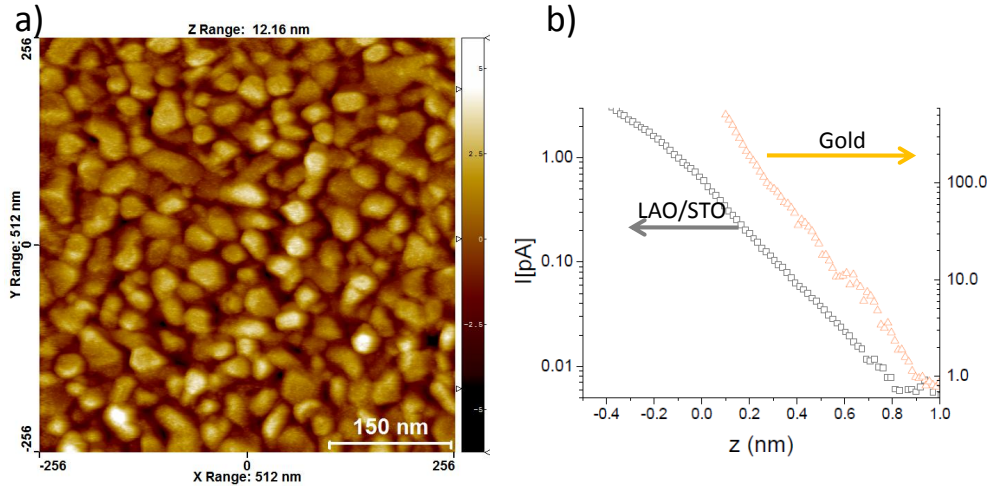


Figure 6.4: Current-distance dependence on 4 u.c. LAO/STO and gold

An important question to be addressed is the problem of tunneling stability in all the measurements performed and in particular in the conditions where one is expecting to tunnel to the interface. The typical  $I(V)$  spectra

and differential conductance curve shown in Fig. [Fig. 6.5], is characterized by a strong asymmetry from positive to negative voltages. The consequence of this is that it is easier to obtain stable conditions at positive voltages than for the negative ones. Being able to work with low currents enabled us to lower the bias voltage thus going further away from the CBM of LAO and also to obtain topographic image even working for negative bias voltages

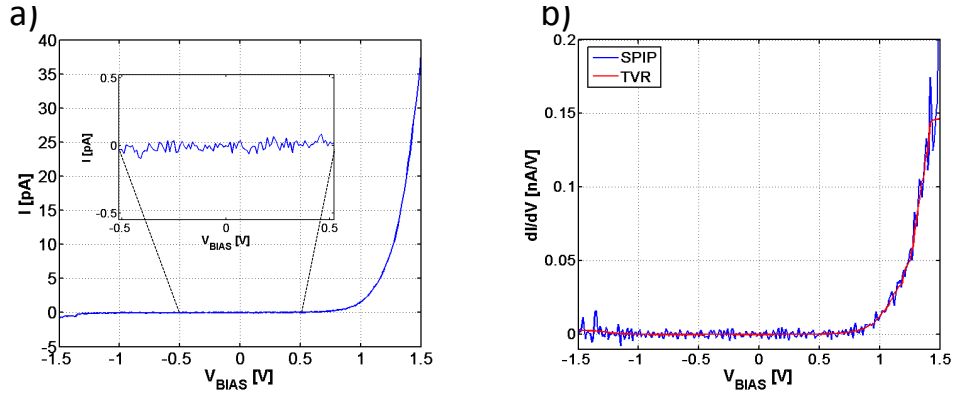


Figure 6.5: a) Single measurement current-voltage characteristic; b) Corresponding calculated differential conductance (calculated by SPIP and TVR)

From the tunneling stability point of view low tunneling currents are desirable, however this is not the case when spectroscopic measurements are in question. The goal in the spectroscopy case is to maximize the current for the given voltage that is usually defined by the maximum/minimum energy value in the spectroscopic energy range of interest. This is important because by doing this we are lowering the tunneling resistance value, thus becoming more sensitive to the voltages lower than the stabilization one. The fact that we were working with sub picoampere currents made the role of this optimization even more pronounced since the noise limit, set by the overall environment, was of 50 fA order. Thus typical stable tunneling conditions used to perform both spectroscopic and topography measurements were bias voltage of 0.75 to 1.0 V and tunnelling currents of 250 fA to 900 fA.

As mentioned at the beginning of this chapter, to probe an interface we should work at low bias voltages, corresponding to an energy lower than that of LAO CBM. The position of the CBM is estimated to be around  $\approx 2.5\text{V}$  [94]. At voltages higher than this values, we obtained a topographic image that is in agreement with the AFM measurements, showing similar terraces orientations and step edges sizes. When working below the CBM, the topographic image shows an increased surface roughness to that above the CBM, while step edges and terraces continued to be well distinguished

[Fig. 6.6]. This effect can be addressed by the fact that in addition to nominal interface roughness (structural or electronic) there is an influence of the LAO barrier roughness on the interface corrugation. The LAO roughness corresponds to an effective increase of the tunneling barrier and, therefore, to an exponential enhancement of the interface corrugation.

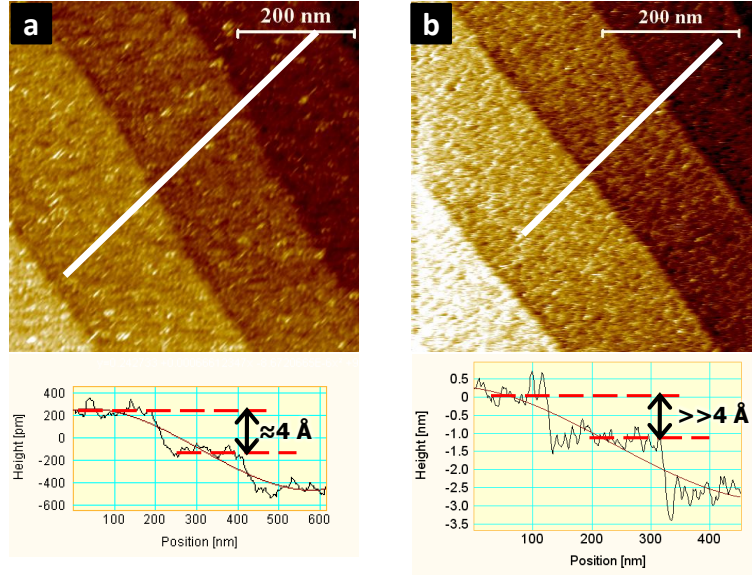


Figure 6.6: Different topographic response when working a) above CBM ( $V_{BIAS}=3.5$  V,  $I_{SET}=5$  pA) and b) below CBM value ( $V_{BIAS}=0.8$ V,  $I_{SET}=250$  fA)

Another interesting difference between the morphology measured below and above the CBM, is a higher step edges heights, well above  $4 \text{ \AA}$ , between neighboring terraces. This can not be explained by a tip to sample contact (and eventual unlikely elastic deformation of the tip), because, even in that case, the topography image should mimic a  $4 \text{ \AA}$  terrace separation. It also can't be explained by assuming different interface depths regarding to the surface of neighboring terraces, since it would lead to the divergence of the interface from the surface plane.

The only plausible explanation comes from the way we are treating data - the only correction we apply to raw topographic images is that of the linear tilt correction (natural tilting of the whole sample and thermal drift compensation). If we assume that apart from regular tilted surface profile there is a linear offset of the tip starting from the step edge and linearly increasing towards the next step edge, the tilt correction will result in the image correctly reproducing terrace planes and step edges form, but producing the height of

more than  $4 \text{ \AA}$ . The only possible reason for the existence of additional linear (or very close to linear) moving of the tip away from the surface/interface, would be a increase in integral density of states from the lower step edge to the higher one [Fig. 6.7]. If this is true, the substrate vicinality should play a role in the overall conducting properties of the electron gas formed. More accurate measurements are needed to confirm this model.

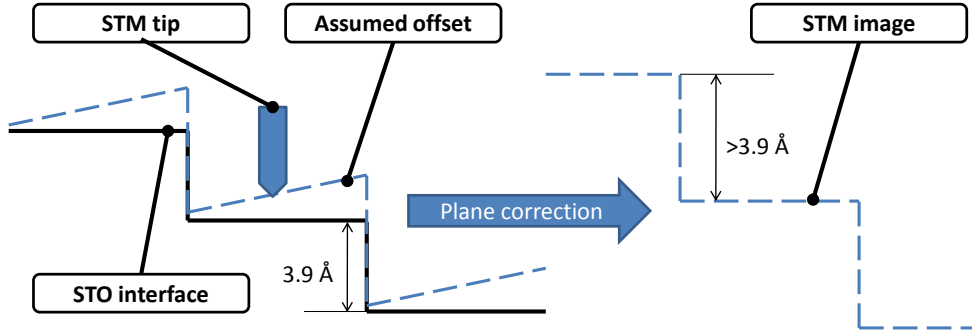


Figure 6.7: Proposed mechanism to address step edge sizes much greater than 1 u.c. in LAO/STO measurements below CBM.

Another important difference between the surface morphology imaged above the CBM (surface sensitive) and below the CBM (interface sensitive) is that using higher spatial resolution a regular pattern is observed on the interface. As example, here we present the measurements done on  $256 \times 256 \text{ nm}^2$  with  $1024 \times 1024 \text{ px}^2$  resolution. The tunneling conditions were  $V_{BIAS}=0.9 \text{ V}$  with  $I_{SET}=700 \text{ fA}$  [Fig. 6.8].

To analyze the pattern, we applied both 2D autocorrelation operator and 2D fast Fourier transform (2D FFT) to the image at Fig. 6.8 (also shown at Fig. 6.9 a)) and to the one obtained by focusing on the terrace pattern, away from the step-edge, shown at Fig. 6.9 b). The real space pattern of ordered structure is enhanced in the autocorrelation image and allows some quantitative estimation. The regular pattern is not long range ordered, but is present in the whole area analyzed [Fig. 6.9 c) and d)]. The 2D-FFT confirms this finding, by showing very spread, but defined, spots around (0,0) point in the reciprocal space. The large width of the spots in the 2D FFT is correlated to the short ordered nature of the structure, which is characterized then by a correlation length of the order of 20 nm (from the inverse of the full width at half maximum of the peaks). The 2D FFT pattern has apparently an hexagonal shape [Fig. 6.9 e)], but when only a part of the sample, not including the step edge is observed [Fig. 6.9 f)] the pattern becomes that of quasi-rectangular lattice with  $a_{ORDERED}=6 \text{ nm}$ ;

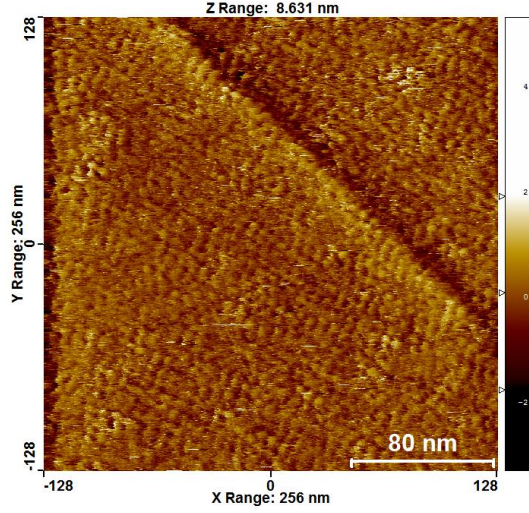


Figure 6.8: STM image on 4 u.c. ( $V_{BIAS}=0.9$  V,  $I_{SET}=700$  fA) showing ordered pattern

$b_{ORDERED}=8$  nm;  $\gamma_{ORDERED}=90^\circ$  [Fig. 6.10], where  $a_{ORDERED}$  and  $b_{ORDERED}$  are oriented in  $(110)$  and  $(1\bar{1}0)$  direction of the  $\text{SrTiO}_3$ . This indicates that near the step edge there is a distortion of this lattice. The overall ordered structure is then more easily described by aligned "bright" spots, being around 3 nm wide, aligned along the  $(110)$  and  $(1\bar{1}0)$  direction of the lattice, and thus forming locally an overall ordered lattice.

To address the nature of this pattern and to see if there are inhomogeneities present in the electronic states of LAO/STO, eventually correlated to the superstructure, we performed an STS mapping of the surface.

To make spectroscopic measurements possible, the bias voltage was kept at  $V_{BIAS}=0.9$  V with  $I_{SET}=700$  fA while the spectroscopy was done in range starting  $V_{START}=1.5$  V and ending at  $V_{START}=-1.5$  V, with nominal 10 mV resolution (301 equidistant point spectra).

In the Fig. 6.11 a) we present typical topographic image obtained during STS mapping. The scan area is of  $256 \times 64$  nm<sup>2</sup> size, sampled in  $256 \times 64$  px<sup>2</sup> both in topographic and spectroscopic regime. The periodic structure is also present in this image, indicating that it is no artifact of the measurements, since the dynamics and biasing procedure in which the topographic image is obtained in standard and spectroscopic mode are completely different (former being acquired in several minutes with feedback always present and spectroscopic one during several hours with regulation turned off in each point).

The over-all average of the tunneling current is presented on Fig. 6.12 a)

6. Scanning tunneling spectroscopy on  $\text{LaAlO}_3$  on  $\text{SrTiO}_3$  systems

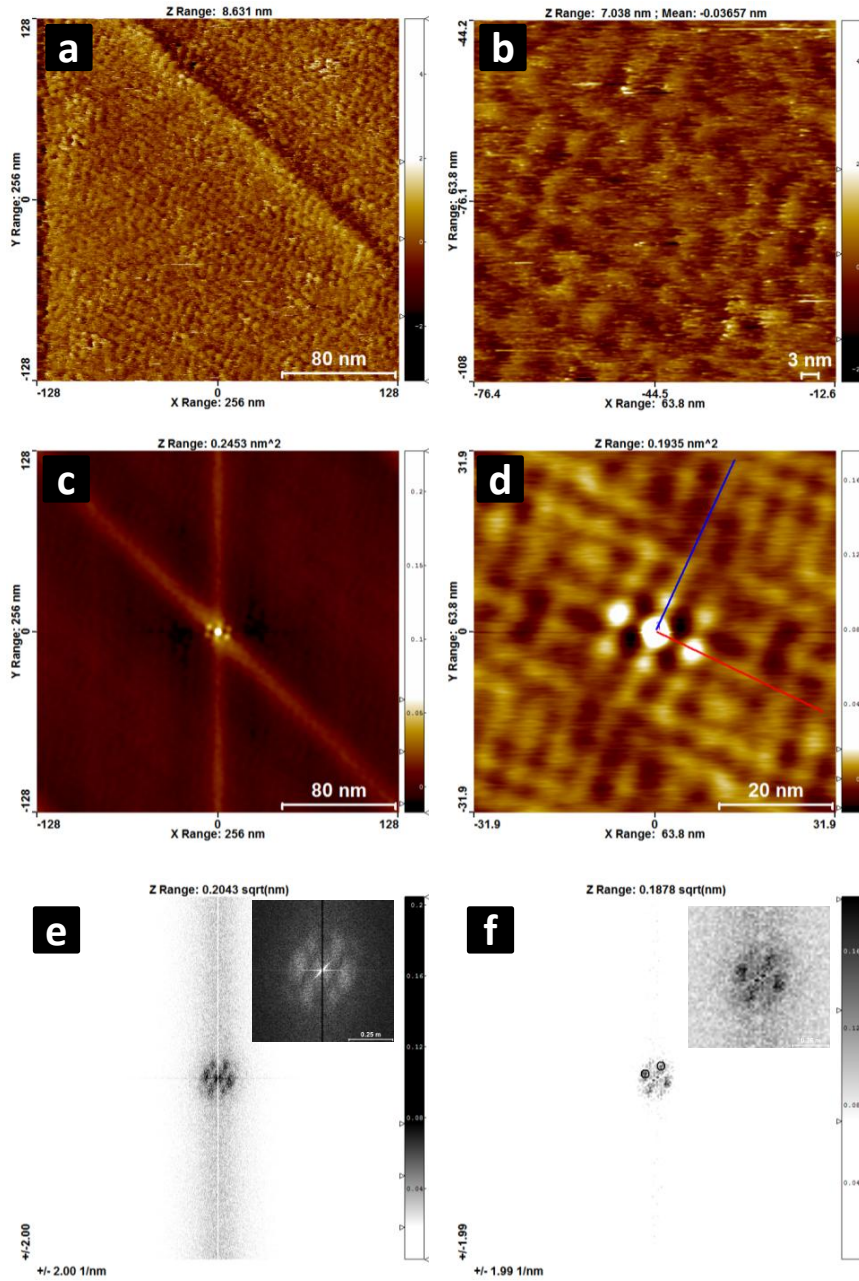


Figure 6.9: The analysis of ordered pattern on 4 u.c. LAO/STO a) The large scale image (includes step-edge); b) small scale image on the terrace away from the step-edge;c) autocorrelation image of a); d) autocorrelation image of b); e)2D FFT of a) with inset showing magnified area around (0,0) peak; f)2D FFT of b) with inset showing magnified area around (0,0) peak;

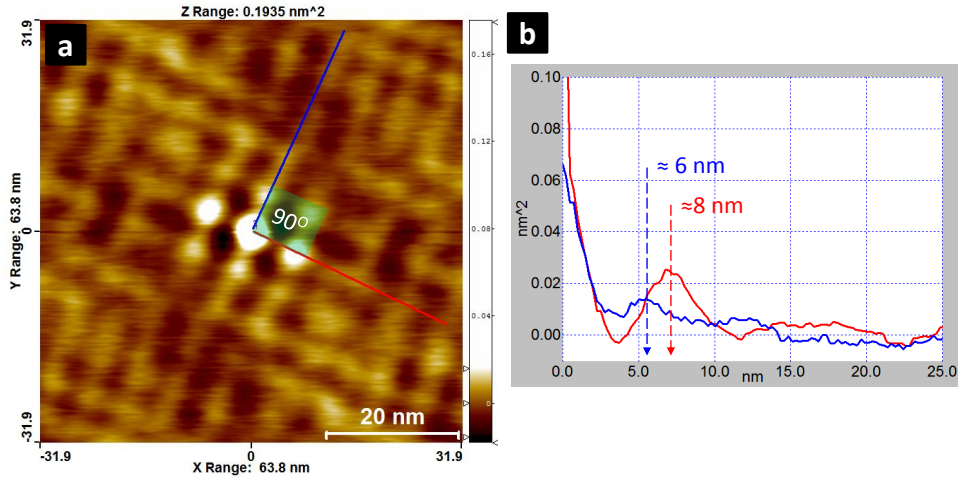


Figure 6.10: Autocorrelation image of on terrace part of the sample and corresponding profile enhancing the real space periodicity showing quasi-rectangular lattice

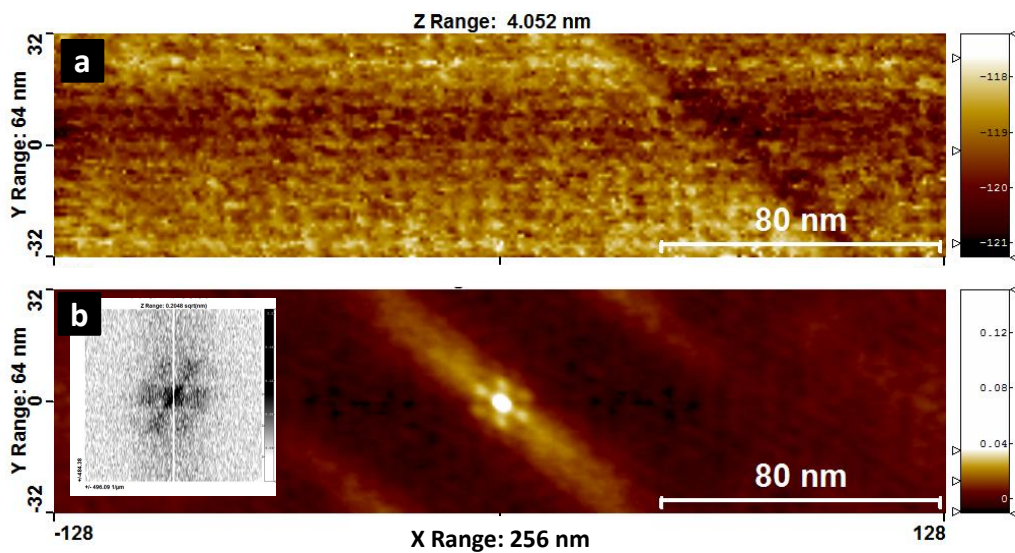


Figure 6.11: a) Topographic image obtained during STS measurement; b) Autocorrelation map and 2D FFT (inset) show same patterns as those obtained during STM measurements

## 6. Scanning tunneling spectroscopy on LaAlO<sub>3</sub> on SrTiO<sub>3</sub> systems

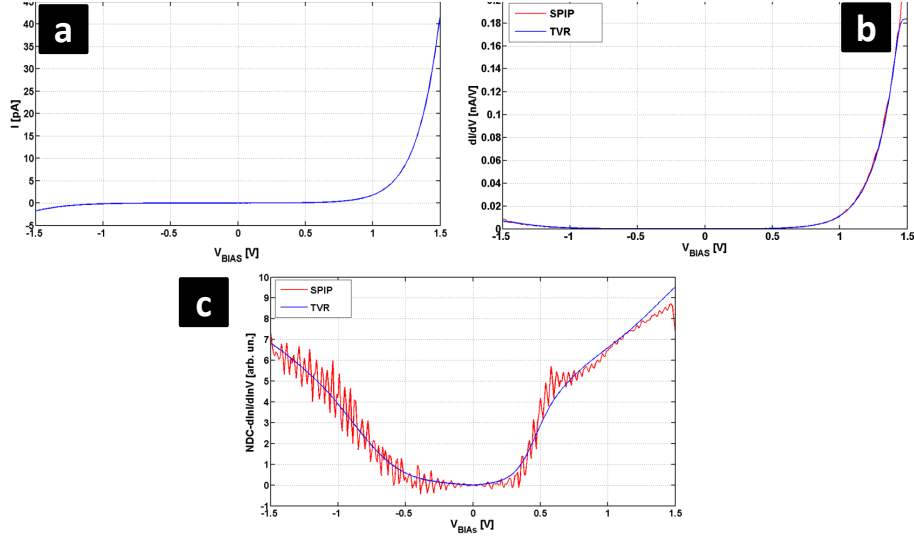


Figure 6.12: a) Average  $I(V)$  curve obtained from the whole spectra set; b) Average of all  $dI/dV(V)$  calculated at each point using SPIP and TVR; c) Average normalize conductivity obtained by using  $d\ln I/d\ln V$  method calculated using SPIP and TVR

, showing, previously mentioned and discussed, strong asymmetry between occupied and unoccupied states. The average of calculated  $dI/dV-V$  curves using commercial SPIP program and TVR algorithm is shown in Fig. 6.12 b) together with  $d\ln I/d\ln V(V)$  normalization also calculated with SPIP and TVR on Fig. 6.12 c).

To address the electronic inhomogeneities the K-means method has been applied to the data using a procedure similar to that used for PCMO ( $x=0.3$ ). On the upper part of figure 6.13, the classification data are presented using the whole spectra (all the bias voltages), only occupied states (negative voltages) and only unoccupied states (positive voltages) values for classification in 2, 3 and 4 classes. On the bottom part of the image the averaged spectra for each class are presented (color coded). Similarly, in 6.14, the classification results and averaged spectra obtained by excluding the  $-0.5$  V to  $0.5$  V region, characterized by a strong suppression of the DOS, are presented.

One can notice that, as for PCMO data, by excluding the gap states, the class image contrast is enhanced, strengthening the empirical rule we proposed that the noise present in the gap of normalized spectra is increasing the error in the classification process thus excluding it from this process would improve reliability of the classification. In this frame, we'll discuss only the spectra obtained from the classification that did not consider the region characterized by very low DOS (Fig. 6.14).

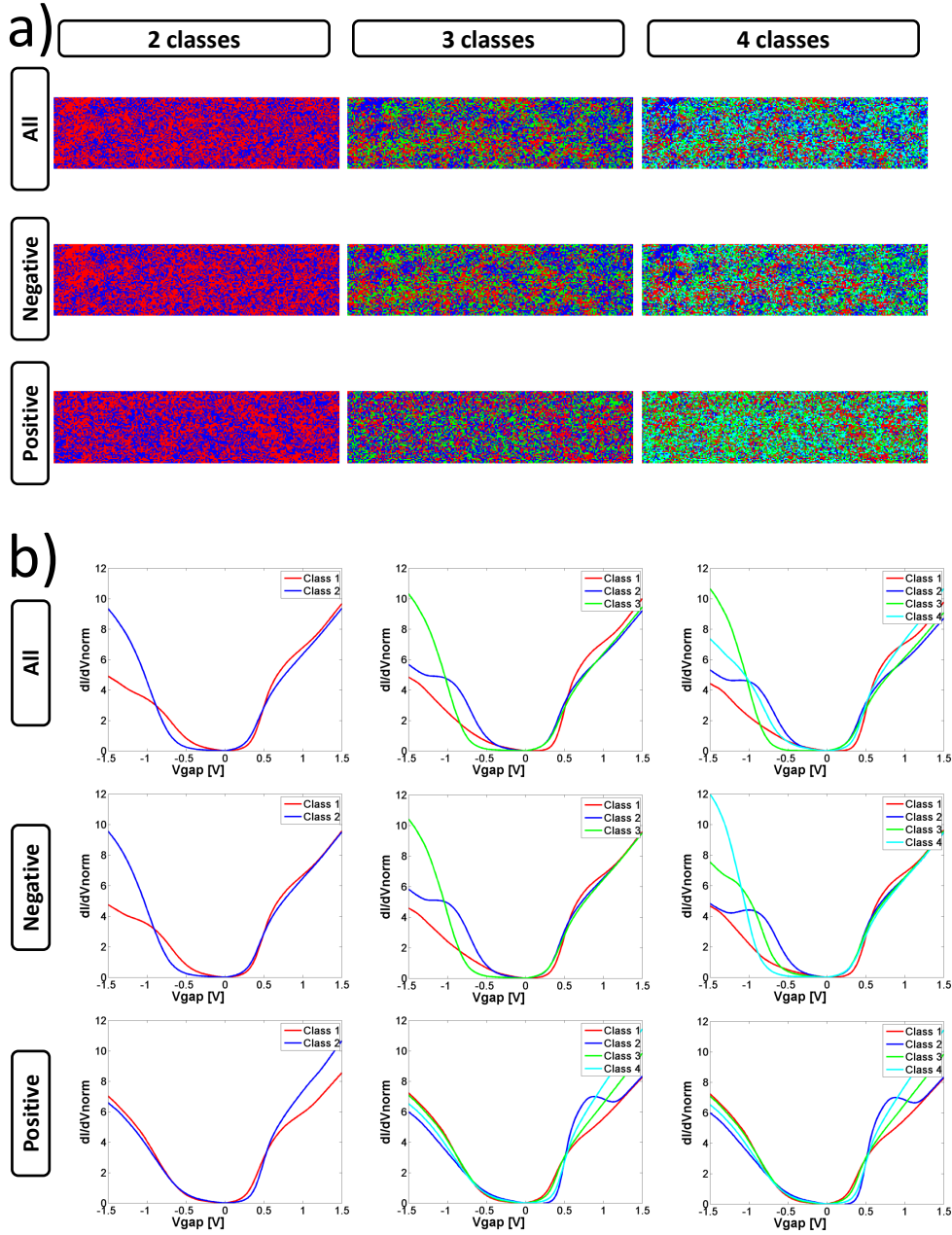


Figure 6.13: a) The result of the k-means classification for 2,3 and 4 assumed classes taking into account whole spectra, only negative voltages and only positive voltages b) corresponding average spectra for each class shown on a) (the curves and classes are appropriately color coded)

6. Scanning tunneling spectroscopy on  $\text{LaAlO}_3$  on  $\text{SrTiO}_3$  systems

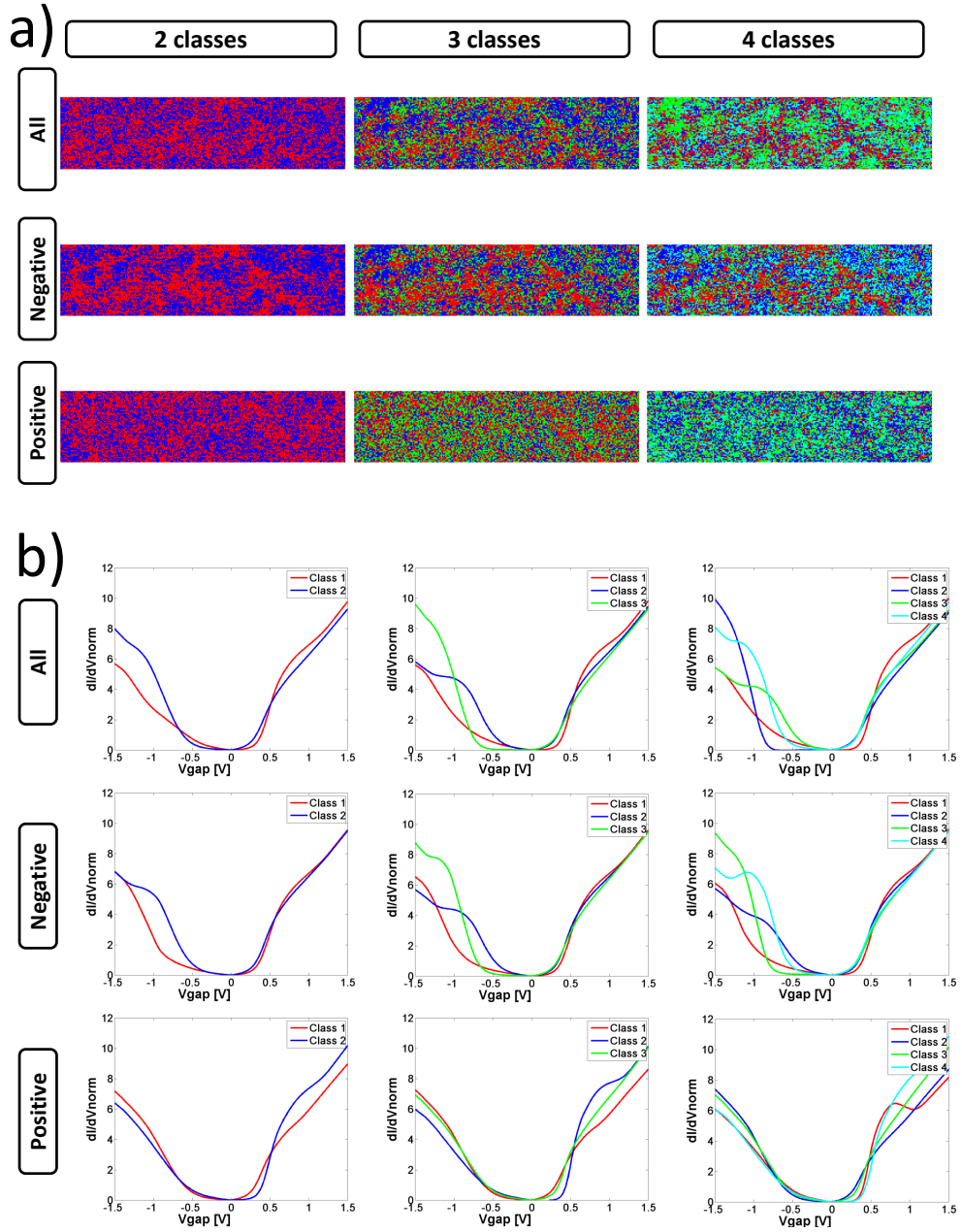


Figure 6.14: a) The result of the k-means classification for 2,3 and 4 assumed classes taking into account whole spectra, only negative voltages and only positive voltages excluding the gap states in each (-0.5 V to 0.5 V); b) corresponding average spectra for each class shown on a) (the curves and classes are appropriately color coded)

It is also clear that the class image obtained when the whole spectral range or only the occupied states are considered (first and second row of upper figure 6.14 ) are better correlated, while the one obtained using only unoccupied states is not (third row of upper figure 6.14). While the former class images show clear regions of different spectral response, the class image for occupied states does not show any clear class separation, but rather noise-like spread classes with a weak correspondence to the other. This indicates that, from an electronic point of view, the unoccupied states are uniformly spread within the spatial resolution used (1nm per px), indicating homogeneous distribution of states contributing to the energy conduction band. Differently from the PCMO (x=0.3) measurements, where the class image was strongly correlated to the topographic one, here we do not see that kind of correlation on any of the class images, apart from the enhancement of the step edge. The inhomogeneities are clearly present in occupied states class image and only few features can be noticed (Fig. 6.14 negative- 2 class image). Different regions (more conductive blue and more insulating red) both show the existence of the states near the Fermi level indicating that both phases are conductive. The inhomogeneities seen at occupied states can be attributed to the role of defects either in the interface or the surface. This is better showed by 3 and 4 class images. In the occupied states, locally emerges a peak at -1 V, most clearly defined on 4 classes map for negative voltages (light blue on Fig. 6.14 4 classes - negative ). This is interesting, because this feature has been observed in the case of doped SrTiO<sub>3</sub> and LaTiO<sub>3</sub>/SrTiO<sub>3</sub> superlattices [98] by photoemission spectroscopy (which is a non local probe). The presence of this peak is often correlated to oxygen vacancies in the case of STO, and therefore to the doping mechanism of this compound. However, the fact that it appears only locally in the interface, indicates that the conduction mechanism in 2D electron gas of LAO/STO is different than that of doped SrTiO<sub>3</sub>.

Another important result of the STS measurements emerges by comparing our data with the theoretical predictions for a bilayer obtained by Pentcheva et al. [84] we mentioned in the previous chapter. LDA+U calculation, obtained on a bilayer perfectly terminated by AlO, suggest that the effective gap of the LAO/STO system is that one from the valence band of surface O2p states (belonging to LAO) to the conduction Ti 3d band at the interface. In particular, for a conducting bilayer, electrons are transferred from the surface O2p to the interface Ti3d. The DOS of the LAO surface, then, should have quite high O2p states close to the Fermi Level. Then tunnelling at negative bias voltages should be much enhanced to that of interface, due to the reduced tunnelling barrier. This is opposite to our observation, suggesting that the surface is not perfectly AlO terminated, and that the theoretical

## 6. Scanning tunneling spectroscopy on LaAlO<sub>3</sub> on SrTiO<sub>3</sub> systems

picture should be revised. Moreover we notice that using large negative voltages, higher than -4 V, an abrupt jump in the current occurs, followed by formation of local granular structure in the topographic image at the place of applied voltage (FIG). This suggest that we are then really tunnelling into or removing oxygen from the surface for negative voltage, because the O2p states of the surface are then accessible. Moreover, our measurements do not favor the idea that localized Ti<sup>3+</sup> 3d<sub>xy</sub> states are realized and occupied by electrons, because from calculation these states should give a quite high peak in the DOS at low negative energy [77]. In contrast we do not see abrupt rise of any states there. It seems again that the states involved in conduction (those around Fermi level) have more an hybrid character, i.e. comes from the hybridization of O 2p and Ti 3d states.

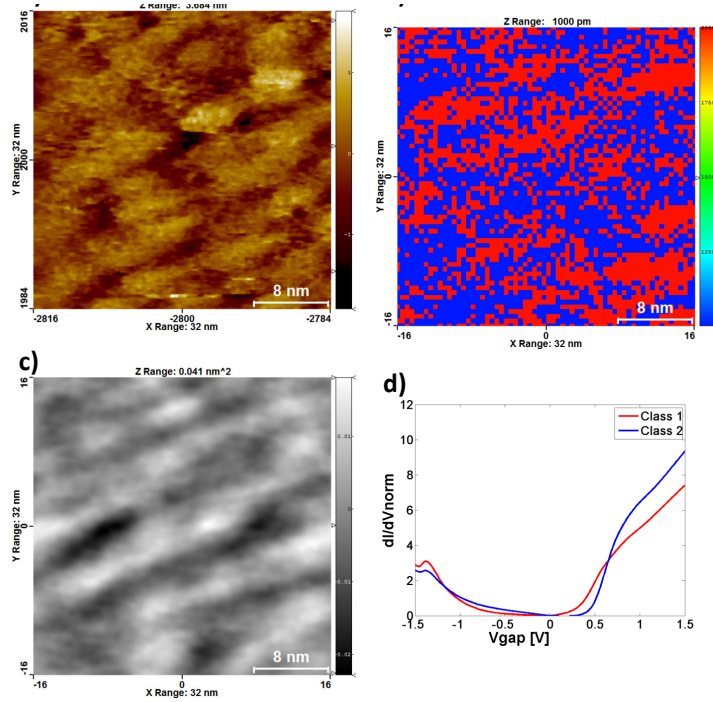


Figure 6.15: a) Topographic image 32×32 nm<sup>2</sup> ; b) Class image 32×32 nm<sup>2</sup> ; c) Cross correlation between images a) and b); d) Averaged spectra for each class (color-coded)

This result is in agreement with XAS measurements [85], which show that non localized occupied states (delocalized electronic states) are favored respect site-centered states which would realize substantial fraction of Ti<sup>3+</sup> cations. At the same time, however, we observe the presence of some kind of ordering from the topographic measurements. This two facts seem to be

at odds, unless the ordering is related to some kind of bond-centered structure, which maintain the valence of Ti close so Ti<sup>4+</sup>. Then the complex topographic response is the combination of structural, electronic and orbital ordering at the interface. The role of the surface is excluded, since its contribution can be only through structural ordering at the surface, not seen in our AFM measurements. Also structural ordering at the surface would be of much smaller roughness, since there is no barrier that would alter it. In this frame, though, a correlation between a spectroscopic class image (electronic properties) and topographic one should be observed. This is particularly true if the 2D-electron gas is strongly correlated.

To substantiate this hypothesis measurement having higher spatial resolution have been performed. In particular a 32×32 nm<sup>2</sup> STS map has been obtained in 256×256 px<sup>2</sup> in topographic and 64×64 px<sup>2</sup> in spectroscopic mode. In Fig. 6.15 the topographic image, two class image obtained by classification considering only unoccupied states, a cross-correlation image between the two and averaged spectra for each of two classes, are shown.

Cross-correlation image between class image and topographic one, clearly show that a correlation exists, since the periodic pattern of the topographic image is reproduced in cross-correlation one, only possible if there exist a similar periodicity between the two images. This leads to conclusion that, in the framework of structurally originated ordered pattern, structural changes are followed by changes in electronic response. Even more, if we examine the average spectra that belongs to each classes, we can see that the structural changes are followed by an orbital reconstruction. Indeed, the majority of theoretical calculation performed on the LAO/STO interface, show that the unoccupied states are mainly composed by 3d states, and in particular 3d<sub>xz</sub>, 3d<sub>yz</sub>, at low energy, while 3d<sub>xy</sub> states cross the Fermi level. Moreover, the 3d<sub>x<sup>2</sup>-y<sup>2</sup></sub> and 3d<sub>z<sup>2</sup></sub> states are located at higher energy, above 1 eV above the Fermi Level. It is possible to notice that the two kind of spectra obtained from the classification on unoccupied states, have interesting features. First we sees that both on the occupied and unoccupied states, there is transfer of states. More precisely, we can see that switching from the red to the 'blue' class, on the occupied states, there is a transfer from the high energy O2p states (red) to the low energy tail crossing the Fermi level, which suggests an hybridization between O2p and Ti3d<sub>xy</sub> playing a role in the electronic properties and in the formation of the ordered pattern[98]. At the same time, going from the 'red' class to the blue one, a transfer of states with energies ≥ 0.7V (usually ascribed to localized Ti 3d<sub>xz</sub> and 3d<sub>yz</sub>) to the Fermi level, correlated with a decrease of hybridized O 2p - Ti 3d<sub>xy</sub> states on the occupied side. This result matches with the idea of an orbital reconstruction taking place in the system.

This orbital, electronic in origin, reconstruction, is clearly correlated with the structural reconstruction which, as happens to the majority of transition metal oxides, probably includes buckling or deformation of the ligand octahedral around Ti ion thus lifting the degeneracy of the Ti 3d bands. The presence of electronic signature ordering is something that can be only attributed to the presence of correlation at the interface. Although not that strongly enhanced as in the narrow-bandwidth strongly correlated PCMO, the electronic signature of the presence of correlation is manifested in the simultaneous observation of an orbital, electronic and structural reconstruction of the interface.

### 6.3 2 u.c. $\text{LaAlO}_3$ on $\text{SrTiO}_3$

As mentioned earlier, the 2 u.c.  $\text{LaAlO}_3$  thin film on  $\text{SrTiO}_3$  is insulating with resistivity above the limits of or instrumental resolution, measuring pA values at best. However, due to the capability of our STM instrument (Omicron nanotechnology VT-SPM) able of measuring  $10^{-13}$  A (limited by noise order this value) we tried to probe the system, even if only to obtain point contact spectra.

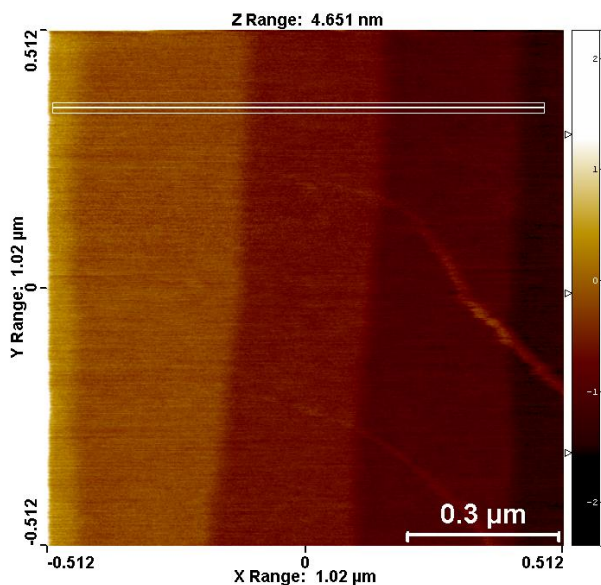


Figure 6.16: C-AFM image of  $\text{LaAlO}_3/\text{SrTiO}_3$  2 u.c. thin film surface

Prior to STM measurements we checked the sample with C-AFM to be sure that the morphology is good. The results of C-AFM measurement on

2 u.c. film of  $\text{LaAlO}_3$  on  $\text{SrTiO}_3$  showing the expected topographic picture is presented in figure 6.16 with corresponding step-edge profile and image histogram in figure 6.17.

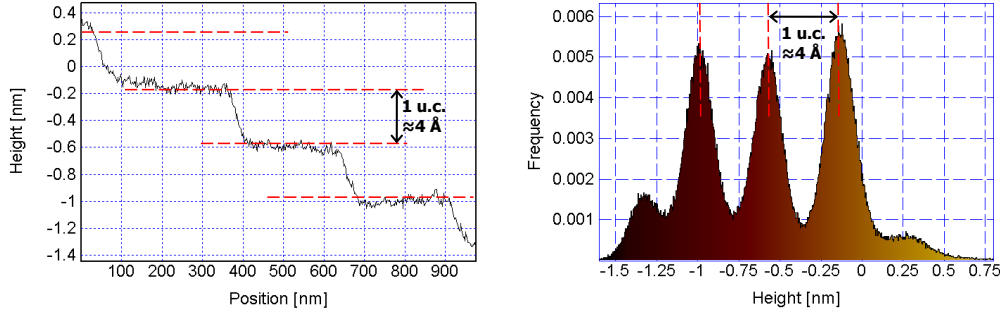


Figure 6.17: Step edge profile (left) and corresponding height histogram distribution (right) for the C-AFM measurement presented on Fig.6.16

Using the same tunnelling conditions used in the case of the 4 u.c. sample, we were able to tunnel to the interface and obtain topographic images in the STM mode [Fig. 6.18 a)], but only with the sample being exposed to ambient light. Once the samples is under dark (all UHV chamber windows covered with appropriate cover), a procedure we used in the case of the 4 uc sample, stable tunneling condition are lost and an eventual tip crash to the sample occurs. This result, suggest that a photodoping mechanism, already known for 3 u.c. samples takes place [99] . The STM mode images of the 2 uc. sample, obtained below the CBM, compared to the 4 u.c., showed similar characteristics, for example the artificial large interfacial roughness.

To investigate the photodoping process, STS measurements were performed and the evolution of DOS spectra in a single point was followed, while changing the lightning conditions. Unfortunately this is more the proof of concept, than rigorous measurements, since we lack a system to introduced controlled light intensities and wavelengths into the STM chamber on to the sample. Rather we controlled three level of ambient light intensity (bright light from the halogen lamp, ambient light and dark closed chamber) and observed the DOS evolution while we changed this conditions.

The spectra are obtained in same conditions as for 4 u.c. ( $V_{BIAS}=0.9$  V with  $I_{SET}=700$  fA ) and were done with tip point constrained while measuring. The  $d\ln I/d\ln V$  normalization was used for obtaining the normalized conductance (NDC).

As shown in figure 6.19 , the spectra show a pronounced peak at -1 eV when photodoping is present. This peak matches again the feature locally

6. Scanning tunneling spectroscopy on LaAlO<sub>3</sub> on SrTiO<sub>3</sub> systems

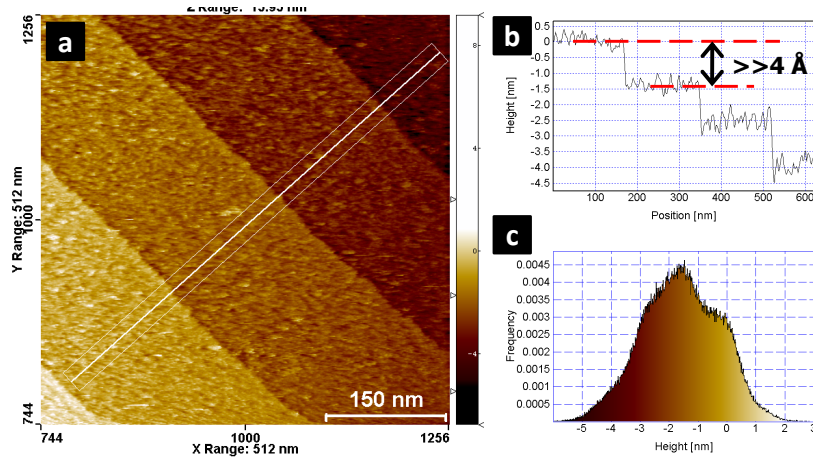


Figure 6.18: a) STM image obtained on 2 u.c. LAO/STO system under ambient light; b) Step edge profile; c) corresponding histogram

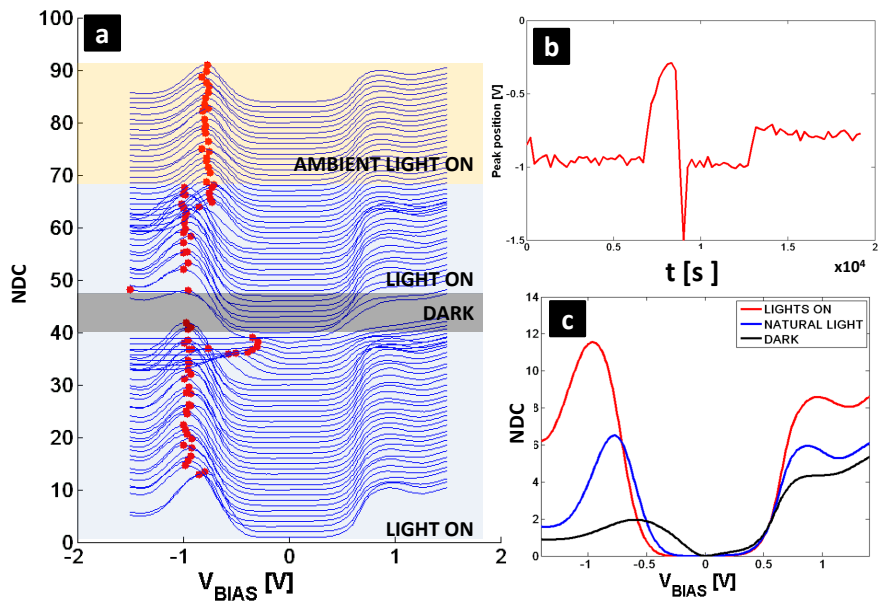


Figure 6.19: a) Evolution of NDC and b) peak shift with time and light intensity; c) average NDC for different light intensities.

observed for the 4 uc LAO/STO, and in photoemission experiments done on doped SrTiO<sub>3</sub> and LaTiO<sub>3</sub>/SrTiO<sub>3</sub> superlattices by Takizawa [98]. This peak is attributed to a bulk like in gap state (IGS) [98]. This feature is present everywhere on the sample surface. We notice here that, when working in the photodoping mode, the assumption of a Fermi distribution of electrons is no longer valid so it is not completely correct to identify the NDC spectra with the DOS.

Upon the putting sample into the dark conditions, a slow decrease followed by a peak movement toward higher energies is observed on occupied state side while the unoccupied states goes to zero. This result, simply indicates in dark the current goes to zero since the interface become insulating. Ultimately the tip and sample will come in contact, indicated by strange I(V) curves exhibiting zero voltage current (due to charge effects since) and : Schottky I(V) dependence elsewhere.

When turned on again a fast switching on (within few seconds) to a 'conducting' state reappears restoring the initial condition. If the intensity of light is lowered, a decrease in the NDC and a peak position movement towards the Fermi level is detected, while the NDC decrease on unoccupied side. This implies that we are not observing the density of states, but rather a value in some way proportional both to the carrier density and the DOS.

## 6.4 Summary

In this chapter we showed that it is possible to probe the conductive interface of the LaAlO<sub>3</sub>/SrTiO<sub>3</sub> through thin insulating film of LaAlO<sub>3</sub>.

For the 4 u.c. sample, we were able to measure STS maps and we found that there are two kind of inhomogeneous signatures associated to the DOS of the interface. Concerning the occupied states, local regions where an in gap state at -1 eV is observed, and a depletion of the DOS toward the lower step edge, are observed. Concerning the unoccupied states, a short range ordered superstructure observed in the topographic images, prove to be correlated also to a spatial distribution of spectral weights from different unoccupied 3d orbitals. The latter are also correlated to a spatial ordering of the orbitals, and therefore to the degree of O2p and Ti3d<sub>xy</sub> hybridization. This measurements also favor a bond-centered distribution of carriers respect the site-centered localization.

For 2 u.c. we were able to measure the evolution of density of states with applied light field and we showed that a photo-doping is taking place at this interface.

A comparison between the results obtained on the 4 uc and 2 uc samples,

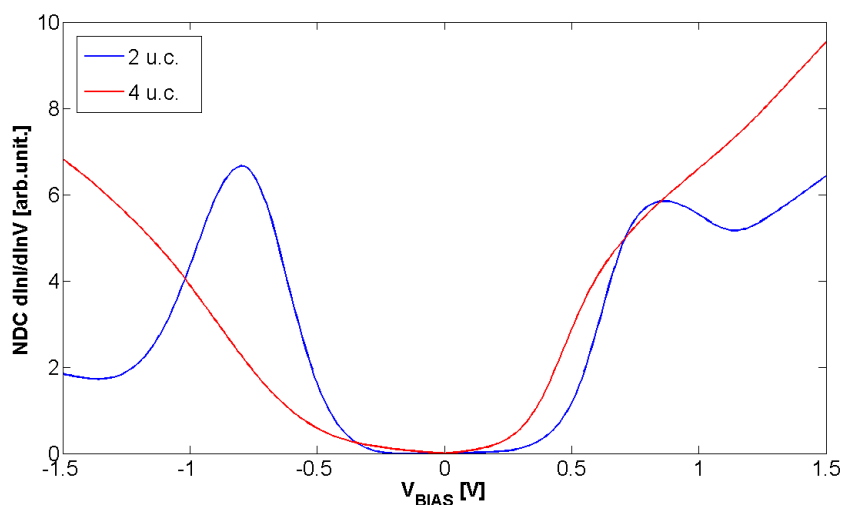


Figure 6.20: Comparison between average 4 u.c normalized conductivity spectra and that of photo-doped 2 u.c.. LAO/STO bilayer

however, show that the conduction mechanism in the two cases is certainly different, also demonstrating that photodoping and electronic reconstructions are not equivalent. Indeed, photodoping produce carriers which are partially localized in the IGS at -1.0 eV, and partially contribute probably to the Fermi LEVEL. However, we have to mention that, while in the case of the 4 uc. there are indication that states are present at the Fermi level, even being very small ( judging from the tail in the DOS ), in the case of the 2uc it seems that even under photo-doping there is a clear gap in the spectra[Fig. 6.20].

This again is in favor of the idea that the appearance of a conductive interface in the LAO/STO system above 4 uc, is related to an intrinsic electronic reconstruction mechanism.

# Chapter 7

## Conclusion

The research presented in this thesis and its original contribution can be roughly divided in two parts; the first part, more technical one, was dealing with the optimization of scanning tunneling spectroscopy technique through numerical tools to extract and analyze spectroscopic data, and the second part in trying to shed a light on the electronic properties of some example of transition metal surfaces and interfaces.

Concerning the first goal, in this thesis we presented three problems arising when dealing with spectroscopic data that need to be treated numerically. We first addressed the problem of numerical derivation and proposed a tool in form of total variation regularization (TVR) algorithm to address the problem. Then we made an overview of existing normalization techniques, used when semiconducting and insulating materials are studied, emphasizing their limits and also putting them in context of proposed TVR algorithm. Lastly, we addressed a method to identify electronic inhomogeneities from the huge amount of data (spectra) acquired in the spectroscopy STS maps. The introduction of the K-means classification algorithm to the STS data analysis, an algorithm well-known in image processing in other areas of science and technology, was successfully implemented to get clear information about the correlation between electronic and morphologic properties of the materials. We used all of this methods when dealing with our experimental data.

Transition metal oxides include variety of materials with different electronic and magnetic properties. The two materials we presented in this thesis are of special interest because they show both the richness of physical phenomena, all involved in explanation of their properties, and, at the same time, a potential for application in novel, all-oxide type devices.

$\text{Pr}_{1-x}\text{Ca}_x\text{MnO}_3$ , a manganite with very strong correlation exhibiting an insulating behavior in the whole phase diagram, is the first material we studied, for two different doping values corresponding to the boundaries of its

charge ordered phase. In both Pr<sub>0.5</sub>Ca<sub>0.5</sub>MnO<sub>3</sub> and Pr<sub>0.7</sub>Ca<sub>0.3</sub>MnO<sub>3</sub>, a correlation between topographic and electronic properties has been found, even though the origin of structural inhomogeneities in the two cases is different. What is presented in this thesis, is the existence of strong connection between the structural and electronic properties in narrow-bandwidth PCMO manganites on a relatively large scale, in contrast with band like or weakly correlated systems.

Finally, we studied the LaAlO<sub>3</sub>/SrTiO<sub>3</sub> system, which in the last years attracted the attention of the condensed matter community for the realization of a highly mobile, 2D electron gas at the interface between two band-insulators. From the point of view of STM, this system seemed unreachable due to the fact that the 2D electron gas is buried and confined to the interface, hence not directly accessible by the STM probe. What is demonstrated here is not only the selective and direct imaging of the interface, but more specifically, the possibility to map the spectroscopic response of this interface spatially. We also speculate, based on our data and data from other experiments, that while the correlations do play a role in this system and give rise to an orbital and structural reconstruction of the interface, the mobile carriers tend to be delocalized rather than occupying localized 3d states. We were also able to probe insulating 2 u.c. LaAlO<sub>3</sub>/SrTiO<sub>3</sub> system associated to a photodoping effect.

As outlook for the future, improving numerical approaches to the raw STS data, could allow to extract the real local density of states (LDOS) e.g. like including density of state of the tip into calculation or using I(z) spectroscopy together with I(V) spectroscopy. Another major improvement would be the possibility to perform spectroscopy as function of the temperature, a parameter very important in transition metal oxides. Mapping the spectroscopic response as a function of temperature in transition metal oxides, especially in Pr<sub>1-x</sub>Ca<sub>x</sub>MnO<sub>3</sub>, should be considered as a next logical step, that would surely give a better understanding on mechanism guiding the TMO electronic properties.

In conclusion, numerical and experimental methods have been proposed for the application of STM/STS to unconventional systems, not only for probing surfaces but also buried interfaces.

# Bibliography

- [1] G. Binnig, H. Rohrer, Ch. Gerber, and E. Weibel. Surface studies by scanning tunneling microscopy. *Phys. Rev. Lett.*, 49(1):57–61, Jul 1982.
- [2] G. Gamow. Successive alpha-transformations. *Nature*, 123:606, Apr 1929.
- [3] J. M. Van Hove, P. Pukite, P. I. Cohen, and C. S. Lent. Rheed streaks and instrument response. *Journal of Vacuum Science and Technology A: Vacuum, Surfaces, and Films*, 1(2):609–613, 1983.
- [4] P. J. Dobson N. Norton J. H. Neave, B. A. Joyce. *Applied Physics A: Materials Science & Processing*, 31:1, 1983.
- [5] Rick Chartrand. Numerical differentiation of noisy, nonsmooth data. *Los Alamos National Laboratory*, 2005.
- [6] Karsten Ahnert and Markus Abel. Numerical differentiation of experimental data: local versus global methods. *Computer Physics Communications*, 177(10):764 – 774, 2007.
- [7] C. R. Vogel and M. E. Oman. Iterative methods for total variation denoising. *SIAM J. Sci. Comput.*, 17(1):227–238, 1996.
- [8] C. R. Vogel. *Computational methods for inverse problems*. Society for Industrial and Applied Mathematics, Philadelphia, 2002.
- [9] V Ukraintsev. Data evaluation technique for electron-tunneling spectroscopy. *Phys. Rev. B*, Jan 1996.
- [10] P. Mårtensson and R. M. Feenstra. Geometric and electronic structure of antimony on the gaas(110) surface studied by scanning tunneling microscopy. *Phys. Rev. B*, 39(11):7744–7753, Apr 1989.
- [11] Joel A. Appelbaum and W. F. Brinkman. Theory of many-body effects in tunneling. *Phys. Rev.*, 186(2):464–470, Oct 1969.

- [12] B. Koslowski, C. Dietrich, A. Tschetschetkin, and P. Ziemann. Evaluation of scanning tunneling spectroscopy data: Approaching a quantitative determination of the electronic density of states. *Physical Review B (Condensed Matter and Materials Physics)*, 75(3):035421, 2007.
- [13] A. D. McNaught and A. Wilkinson, editors. *IUPAC. Compendium of Chemical Terminology, (the 'Gold Book')*. Blackwell Scientific Publications, Oxford, 2nd edition, 1997.
- [14] M Imada, A Fujimori, and Y Tokura. Metal-insulator transitions. *Reviews of Modern Physics*, Jan 1998.
- [15] J. P. Zhou, J. T. McDevitt, J. S. Zhou, H. Q. Yin, J. B. Goodenough, Y. Gim, and Q. X. Jia. Effect of tolerance factor and local distortion on magnetic properties of the perovskite manganites. *Applied Physics Letters*, 75(8):1146–1148, 1999.
- [16] Y. Tokura and N. Nagaosa. Orbital Physics in Transition-Metal Oxides. *Science*, 288(5465):462–468, 2000.
- [17] D I Khomskii. Role of orbitals in the physics of correlated electron systems. *Physica Scripta*, 72(5):CC8, 2005.
- [18] Elbio Dagotto. Complexity in Strongly Correlated Electronic Systems. *Science*, 309(5732):257–262, 2005.
- [19] R. von Helmolt, J. Wecker, B. Holzapfel, L. Schultz, and K. Samwer. Giant negative magnetoresistance in perovskitelike  $la_2/3ba_1/3mnox$  ferromagnetic films. *Phys. Rev. Lett.*, 71(14):2331–2333, Oct 1993.
- [20] Dmitry V Efremov, Jeroen Van Den Brink, and Daniel I Khomskii. Bond- versus site-centred ordering and possible ferroelectricity in manganites. *Nat Mater*, 3(12):853–856, Dec 2004.
- [21] E Dagotto. Theory of manganites: key role of intrinsic inhomogeneities. *Journal of Magnetism and Magnetic Materials*, 226-230:763–768, May 2001.
- [22] Koichi Momma and Fujio Izumi. VESTA: a three-dimensional visualization system for electronic and structural analysis. *Journal of Applied Crystallography*, 41(3):653–658, Jun 2008.
- [23] Y Tomioka, A Asamitsu, H Kuwahara, and Y Moritomo. Magnetic-field-induced metal-insulator phenomena in  $pr_{1-x}ca_xmno_3$  with controlled. *Phys. Rev. B*, Jan 1996.

- 
- [24] Z. Jirak, S. Krupicka, Z. Simsa, M. Dlouha, and S. Vratilav. Neutron diffraction study of  $\text{Pr}_{1-x}\text{Ca}_x\text{MnO}_3$  perovskites. *Journal of Magnetism and Magnetic Materials*, 53(1-2):153 – 166, 1985.
- [25] Y Moritomo, H Kuwahara, Y Tomioka, and Y Tokura. Pressure effects on charge-ordering transitions in perovskite manganites. *Phys. Rev. B*, 55(12):7549–7556, 1997.
- [26] E Dagotto, T Hotta, and A Moreo. Colossal magnetoresistant materials: The key role of phase separation. *Arxiv preprint cond-mat*, Jan 2000.
- [27] A. Asamitsu, Y. Tomioka, H. Kuwahara, and Y. Tokura. Current switching of resistive states in magnetoresistive manganites. *Nature*, 388(6637):50–52, 1997. 0028-0836.
- [28] M Fiebig, K Miyano, Y Tomioka, and Y Tokura. Visualization of the local insulator-metal transition in  $\text{Pr}_{0.7}\text{Ca}_{0.3}\text{MnO}_3$ . *Science(Washington, D. C.)*, 280(5371):1925–1928, 1998.
- [29] V Kiryukhin, D Casa, JP Hill, B Keimer, A Vigliante, Y Tomioka, and Y Tokura. An x-ray-induced insulator-metal transition in a magnetoresistive manganite. *Nature*, 386(6627):813–815, 1997.
- [30] M. Hervieu, A. Barnabé, C. Martin, A. Maignan, and B. Raveau. Charge disordering induced by electron irradiation in colossal magnetoresistant manganites. *Phys. Rev. B*, 60(2):R726–R729, Jul 1999.
- [31] A. Daoud-Aladine, J. Rodríguez-Carvajal, L. Pinsard-Gaudart, M. T. Fernández-Díaz, and A. Revcolevschi. Zener polaron ordering in half-doped manganites. *Phys. Rev. Lett.*, 89(9):097205, Aug 2002.
- [32] M. Fäth, S. Freisem, A. A. Menovsky, Y. Tomioka, J. Aarts, and J. A. Mydosh. Spatially Inhomogeneous Metal-Insulator Transition in Doped Manganites. *Science*, 285(5433):1540–1542, 1999.
- [33] T. Becker, C. Streng, Y. Luo, V. Moshnyaga, B. Damaschke, N. Shannon, and K. Samwer. Intrinsic inhomogeneities in manganite thin films investigated with scanning tunneling spectroscopy. *Phys. Rev. Lett.*, 89(23):237203, Nov 2002.
- [34] S Seiro, Y Fasano, I Maggio-Aprile, E Koller, O Kuffer, and Ø Fischer. Polaronic signature in the metallic phase of  $\text{La}_{0.7}\text{Ca}_{0.3}\text{MnO}_3$  films detected by scanning tunneling spectroscopy. *Phys. Rev. B*, 77(2):4, Jan 2008.

## Bibliography

---

- [35] L Sudheendra, V Moshnyaga, E. D Mishina, B Damaschke, Th Rasing, and K Samwer. Direct imaging of lattice-strain-induced stripe phases in an optimally doped manganite film. *Phys. Rev. B*, 75(17):4, May 2007.
- [36] C Renner, G Aeppli, BG Kim, YA Soh, and SW Cheong. Atomic-scale images of charge ordering in a mixed-valence manganite. *Nature*, 416:518–521, 2002.
- [37] J. X Ma, D. T Gillaspie, E. W Plummer, and J Shen. Visualization of localized holes in manganite thin films with atomic resolution. *Phys. Rev. Lett.*, 95(23):4, Dec 2005.
- [38] H. M Rønnow, Ch Renner, G Aeppli, T Kimura, and Y Tokura. Polarons and confinement of electronic motion to two dimensions in a layered manganite. *Nature*, 440(7087):1025–1028, Apr 2006.
- [39] C Renner, G Aeppli, B Kim, Y Soh, and S Cheong. Atomic-scale images of charge ordering in a mixed-valence manganite. *Arxiv preprint cond-mat*, Jan 2002.
- [40] Z. Jirák, F. Damay, M. Hervieu, C. Martin, B. Raveau, G. André, and F. Bourée. Magnetism and charge ordering in  $pr_{0.5}ca_{x}sr_{0.5-x}mno_3$  ( $x = 0.09$  and  $0.5$ ). *Phys. Rev. B*, 61(2):1181–1188, Jan 2000.
- [41] L Vasylechko, L Akselrud, W Morgenroth, and U Bismayer . . . . The crystal structure of  $ndgao_3$  at 100 k and 293 k based on synchrotron data. *Journal of Alloys and Compounds*, Jan 2000.
- [42] J. X. Ma, D. T. Gillaspie, E. W. Plummer, and J. Shen. Visualization of localized holes in manganite thin films with atomic resolution. *Phys. Rev. Lett.*, 95(23):237210, Dec 2005.
- [43] Ch Renner, G. Aeppli, B. G. Kim, Yeong-Ah Soh, and S. W. Cheong. Atomic-scale images of charge ordering in a mixed-valence manganite. *Nature*, 416(6880):518–521, April 2002.
- [44] S. Seiro, Y. Fasano, I. Maggio-Aprile, E. Koller, O. Kuffer, and Ø . Fischer. Polaronic signature in the metallic phase of  $la_{0.7}ca_{0.3}mno_3$  films detected by scanning tunneling spectroscopy. *Physical Review B (Condensed Matter and Materials Physics)*, 77(2):020407, 2008.
- [45] M. Fujimoto, H. Koyama, Y. Nishi, T. Suzuki, S. Kobayashi, Y. Tamai, and N. Awaya. Crystallographic domain structure of an epitaxial

- (pr0.7ca0.3)mno<sub>3</sub> thin film grown on a sr<sub>2</sub>ti<sub>3</sub>o<sub>7</sub> single crystal substrate. *Journal of the American Ceramic Society*, 90:2205, 2007.
- [46] Jouko Nieminen, Hsin Lin, R. S. Markiewicz, and A. Bansil. Origin of the electron-hole asymmetry in the scanning tunneling spectrum of the high-temperature bi<sub>2</sub>sr<sub>2</sub>caCu<sub>2</sub>O<sub>8+δ</sub> superconductor. *Physical Review Letters*, 102(3):037001, 2009.
- [47] H. Lehnert, Hans Boysen, J. Schneider, Friedrich Frey, D. Hohlwein, P. Radaelli, and H. Ehrenberg. A powder diffraction study of the phase transition in laalo<sub>3</sub>. *Zeitschrift für Kristallographie*, 215:536, 2000.
- [48] S. A. Hayward, F. D. Morrison, S. A. T. Redfern, E. K. H. Salje, J. F. Scott, K. S. Knight, S. Tarantino, A. M. Glazer, V. Shuvaeva, P. Daniel, M. Zhang, and M. A. Carpenter. Transformation processes in laalo<sub>3</sub>: Neutron diffraction, dielectric, thermal, optical, and raman studies. *Phys. Rev. B*, 72(5):054110, Aug 2005.
- [49] Dominique de Ligny and Pascal Richet. High-temperature heat capacity and thermal expansion of sr<sub>2</sub>ti<sub>3</sub>o<sub>7</sub> and srzro<sub>3</sub> perovskites. *Phys. Rev. B*, 53(6):3013–3022, Feb 1996.
- [50] B. C. Chakoumakos, D. G. Schlom, M. Urbanik, and J. Luine. Thermal expansion of laalo<sub>3</sub> and (la,sr)(al,ta)o<sub>3</sub>, substrate materials for superconducting thin-film device applications. *Journal of Applied Physics*, 83(4):1979–1982, 1998.
- [51] Seung-Gu Lim, Stas Kriventsov, Thomas N. Jackson, J. H. Haeni, D. G. Schlom, A. M. Balbashov, R. Uecker, P. Reiche, J. L. Freeouf, and G. Lucovsky. Dielectric functions and optical bandgaps of high-κ dielectrics for metal-oxide-semiconductor field-effect transistors by far ultraviolet spectroscopic ellipsometry. *Journal of Applied Physics*, 91(7):4500–4505, 2002.
- [52] P. W. Peacock and J. Robertson. Band offsets and schottky barrier heights of high dielectric constant oxides. *Journal of Applied Physics*, 92(8):4712–4721, 2002.
- [53] R. W. Simon, C. E. Platt, A. E. Lee, G. S. Lee, K. P. Daly, M. S. Wire, J. A. Luine, and M. Urbanik. Low-loss substrate for epitaxial growth of high-temperature superconductor thin films. *Applied Physics Letters*, 53(26):2677–2679, 1988.

## Bibliography

---

- [54] Pietro Delugas, Vincenzo Fiorentini, and Alessio Filippetti. Dielectric properties and long-wavelength optical modes of the high- $\kappa$  oxide  $\text{LaAlO}_3$ . *Phys. Rev. B*, 71(13):134302, Apr 2005.
- [55] Gerald Lucovsky, Jerry L. Whitten, and Yu Zhang. A molecular orbital model for the electronic structure of transition metal atoms in silicate and aluminate alloys. *Microelectronic Engineering*, 59(1-4):329 – 334, 2001.
- [56] H. Ling, X. Lu, A. Li, D. Wu, Q. Shao, J. Sheng, Z. Liu, N. Ming, X. Wang, B.-Y. Nguyen, and H. Zhou. Study of interfacial oxide layer of  $\text{LaAlO}_3$  gate dielectrics on Si for metal insulator semiconductor devices. *Applied Physics A: Materials Science & Processing*, 80:641–644, February 2005.
- [57] K. A. Müller, W. Berlinger, and F. Waldner. Characteristic structural phase transition in perovskite-type compounds. *Phys. Rev. Lett.*, 21(12):814–817, Sep 1968.
- [58] E. Heifets, R. I. Eglitis, E. A. Kotomin, J. Maier, and G. Borstel. First-principles calculations for  $\text{SrTiO}_3(100)$  surface structure. *Surface Science*, 513(1):211 – 220, 2002.
- [59] M. Kawasaki, A. Ohtomo, T. Arakane, K. Takahashi, M. Yoshimoto, and H. Koinuma. Atomic control of  $\text{SrTiO}_3$  surface for perfect epitaxy of perovskite oxides. *Applied Surface Science*, 107:102 – 106, 1996. Proceedings of the Third International Symposium on Atomically Controlled Surfaces and Interfaces.
- [60] E. Heifets, R. I. Eglitis, E. A. Kotomin, J. Maier, and G. Borstel. Ab initio modeling of surface structure for  $\text{SrTiO}_3$  perovskite crystals. *Phys. Rev. B*, 64(23):235417, Nov 2001.
- [61] H. P. R. Frederikse, W. R. Thurber, and W. R. Hosler. Electronic transport in strontium titanate. *Phys. Rev.*, 134(2A):A442–A445, Apr 1964.
- [62] Weidong Luo, Wenhui Duan, Steven G. Louie, and Marvin L. Cohen. Structural and electronic properties of  $n$ -doped and  $p$ -doped  $\text{SrTiO}_3$ . *Phys. Rev. B*, 70(21):214109, Dec 2004.
- [63] D. Kan, T. Terashima, R. Kanda, A. Masuno, K. Tanaka, S. Chu, H. Kan, A. Ishizumi, Y. Kanemitsu, Y. Shimakawa, and M. Takano.

- 
- Blue-light emission at room temperature from Ar<sup>+</sup>-irradiated SrTiO<sub>3</sub>. *Nature Materials*, 4:816–819, November 2005.
- [64] J. F. Schooley, W. R. Hosler, and Marvin L. Cohen. Superconductivity in semiconducting srTiO<sub>3</sub>. *Phys. Rev. Lett.*, 12(17):474–475, Apr 1964.
- [65] J. F. Schooley, W. R. Hosler, E. Ambler, J. H. Becker, Marvin L. Cohen, and C. S. Koonce. Dependence of the superconducting transition temperature on carrier concentration in semiconducting srTiO<sub>3</sub>. *Phys. Rev. Lett.*, 14(9):305–307, Mar 1965.
- [66] K. O. Grosse-Holz, J. F. M. Cillessen, and R. Waser. Electrical characterization of semiconducting la doped srTiO<sub>3</sub> thin films prepared by pulsed laser deposition. *Applied Surface Science*, 96-98:784 – 790, 1996. Proceedings of Symposium F: Third International Symposium on Laser Ablation of the 1995 E-MRS Spring Conference.
- [67] G. Binnig, A. Baratoff, H. E. Hoenig, and J. G. Bednorz. Two-band superconductivity in nb-doped srTiO<sub>3</sub>. *Phys. Rev. Lett.*, 45(16):1352–1355, Oct 1980.
- [68] Stefan Patrick Thiel. *Study of Interface Properties in LaAlO<sub>3</sub>/SrTiO<sub>3</sub> Heterostructures*. PhD thesis, Mathematisch-naturwissenschaftlichen Fakultät der Universität Augsburg, 2009.
- [69] R. A. McKee, F. J. Walker, and M. F. Chisholm. Crystalline oxides on silicon: The first five monolayers. *Phys. Rev. Lett.*, 81(14):3014–3017, Oct 1998.
- [70] J. H. Haeni, P. Irvin, W. Chang, R. Uecker, P. Reiche, Y. L. Li, S. Choudhury, W. Tian, M. E. Hawley, B. Craigo, A. K. Tagantsev, X. Q. Pan, S. K. Streiffer, L. Q. Chen, S. W. Kirchoefer, J. Levy, and D. G. Schlom. Room-temperature ferroelectricity in strained SrTiO<sub>3</sub>. *Nature*, 430:758–761, August 2004.
- [71] A Ohtomo and H. Y Hwang. A high-mobility electron gas at the laalo<sub>3</sub>/srTiO<sub>3</sub> heterointerface. *Nature*, 427(6973):423–426, Jan 2004.
- [72] A. Ohtomo and H. Y. Hwang. Corrigendum: A high-mobility electron gas at the laalo<sub>3</sub>/srTiO<sub>3</sub> heterointerface. *Nature*, 441:120–+, may 2006.
- [73] G. A. Baraff, Joel A. Appelbaum, and D. R. Hamann. Self-consistent calculation of the electronic structure at an abrupt gaas-ge interface. *Phys. Rev. Lett.*, 38(5):237–240, Jan 1977.

## Bibliography

---

- [74] W. A. Harrison, E. A. Kraut, J. R. Waldrop, and R. W. Grant. Polar heterojunction interfaces. *Phys. Rev. B*, 18(8):4402–4410, Oct 1978.
- [75] Naoyuki Nakagawa, Harold Y Hwang, and David A Muller. Why some interfaces cannot be sharp. *Nat Mater*, 5(3):204–209, Mar 2006.
- [76] Y Tokura and N Nagaosa. Orbital physics in transition-metal oxides. *Science*, Jan 2000.
- [77] R Pentcheva and W. E Pickett. Charge localization or itineracy at  $\text{LaAlO}_3/\text{SrTiO}_3$  interfaces: Hole polarons, oxygen vacancies, and mobile electrons. *Phys. Rev. B*, 74(3):1–7, Jul 2006.
- [78] Min Sik Park, S. H Rhim, and Arthur J Freeman. Charge compensation and mixed valency in  $\text{LaAlO}_3/\text{SrTiO}_3$  heterointerfaces studied by the flapw method. *Phys. Rev. B*, 74(20):1–6, Nov 2006.
- [79] S. Gemming and G. Seifert.  $\text{SrTiO}_3(001)/\text{LaAlO}_3(001)$  multilayers: A density-functional investigation. *Acta Materialia*, 54(16):4299 – 4306, 2006.
- [80] D. R Hamann, D. A Muller, and H. Y Hwang. Lattice-polarization effects on electron-gas charge densities in ionic superlattices. *Phys. Rev. B*, 73(19):1–5, May 2006.
- [81] F. Lichtenberg, D. Widmer, J. G. Bednorz, T. Williams, and A. Reller. Phase diagram of  $\text{LaTiO}_x$ : from 2d layered ferroelectric insulator to 3d weak ferromagnetic semiconductor. *Zeitschrift fr Physik B Condensed Matter*, 82:211–216, 1991.
- [82] F. Lichtenberg, A. Herrnberger, K. Wiedenmann, and J. Mannhart. Synthesis of perovskite-related layered  $\text{A}n\text{B}n\text{O}3n+2 = \text{A}n\text{B}n\text{O}3n+2$  type niobates and titanates and study of their structural, electric and magnetic properties. *Progress in Solid State Chemistry*, 29(1-2):1 – 70, 2001.
- [83] S Thiel, G Hammerl, A Schmehl, CW Schneider, and J Mannhart. Tunable quasi-two-dimensional electron gases in oxide heterostructures. *Science*, 313(5795):1942–1945, 2006.
- [84] Rossitza Pentcheva and Warren E Pickett. Avoiding the polarization catastrophe in  $\text{LaAlO}_3$  overlayers on  $\text{SrTiO}_3(001)$  through polar distortion. *Phys. Rev. Lett.*, 102(10):1–4, Mar 2009.

- [85] M. Salluzzo, J. C. Cezar, N. B. Brookes, V. Bisogni, G. M. De Luca, C. Richter, S. Thiel, J. Mannhart, M. Huijben, A. Brinkman, G. Rijnders, and G. Ghiringhelli. Orbital reconstruction and the two-dimensional electron gas at the  $\text{LaAlO}_3/\text{SrTiO}_3$  interface. *Physical Review Letters*, 102(16):166804, 2009.
- [86] G Rijnders and DHA Blank. Perovskite oxides: An atomic force pencil and eraser. *Nat Mater*, 7(4):270–271, 2008.
- [87] A Brinkman, M Huijben, M Van Zalk, J Huijben, U Zeitler, J. C Maan, W. G Van Der Wiel, G Rijnders, D. H. A Blank, and H Hilgenkamp. Magnetic effects at the interface between non-magnetic oxides. *Nat Mater*, 6(7):493–496, Jul 2007.
- [88] N Reyren, S Thiel, A. D Caviglia, L. F Kourkoutis, G Hammerl, C Richter, C. W Schneider, T Kopp, A.-S Ruetschi, D Jaccard, M Gabay, D. A Muller, J.-M Triscone, and J Mannhart. Superconducting interfaces between insulating oxides. *Science*, 317(5842):1196–1199, Aug 2007.
- [89] A. D Caviglia, S Gariglio, N Reyren, D Jaccard, T Schneider, M Gabay, S Thiel, G Hammerl, J Mannhart, and J.-M Triscone. Electric field control of the  $\text{LaAlO}_3/\text{SrTiO}_3$  interface ground state. *Nature*, 456(7222):624–627, Dec 2008.
- [90] C. W. Schneider, S. Thiel, G. Hammerl, C. Richter, and J. Mannhart. Microlithography of electron gases formed at interfaces in oxide heterostructures. *Applied Physics Letters*, 89(12):122101, 2006.
- [91] C Cen, S Thiel, G Hammerl, C. W Schneider, K. E Andersen, C. S Hellberg, J Mannhart, and J Levy. Nanoscale control of an interfacial metal–insulator transition at room temperature. *Nat Mater*, 7(4):298–302, Apr 2008.
- [92] C Cen, S Thiel, J Mannhart, and J Levy. Oxide nanoelectronics on demand. *Science*, 323(5917):1026–1030, Feb 2009.
- [93] M Basletic, J.-L Maurice, C Carrétéro, G Herranz, O Copie, M Bibes, É Jacquet, K Bouzehouane, S Fusil, and A Barthélémy. Mapping the spatial distribution of charge carriers in  $\text{LaAlO}_3/\text{SrTiO}_3$  heterostructures. *Nat Mater*, 7(8):621–625, Aug 2008.

- [94] M. Breitschaft, V. Tinkl, N. Pavlenko, S. Thiel, C. Richter, J. R. Kirtley, Y. C. Liao, G. Hammerl, V. Eyert, T. Kopp, and J. Mannhart. Two-dimensional electron liquid state at  $\text{LaAlO}_3\text{-SrTiO}_3$  interfaces, 2009.
- [95] S Schintke and W Schneider. Insulators at the ultrathin limit: electronic structure studied by scanning tunnelling microscopy . . . . *JOURNAL OF PHYSICS CONDENSED MATTER*, Jan 2004.
- [96] S Schintke, S Messerli, M Pivetta, and F Patthey. Insulator at the ultrathin limit: MgO on Ag(001). *Phys. Rev. Lett.*, Jan 2001.
- [97] J Viernow, DY Petrovykh, A Kirakosian, JL Lin, FK Men, M Henzler, and FJ Himpsel. Chemical imaging of insulators by STM. *PHYSICAL REVIEW-SERIES B-*, 59:10356–10361, 1999.
- [98] M Takizawa, H Wadati, K Tanaka, M Hashimoto, T Yoshida, A Fujimori, A Chikamatsu, H Kumigashira, M Oshima, K Shibuya, T Mihara, T Ohnishi, M Lippmaa, M Kawasaki, H Koinuma, S Okamoto, and A. J. Millis. Photoemission from buried interfaces in  $\text{SrTiO}_3/\text{LaTiO}_3$  superlattices. *Phys. Rev. Lett.*, 97(5):1–4, Aug 2006.
- [99] A. Savoia, D. Paparo, P. Perna, Z. Ristic, M. Salluzzo, F. Miletto Granozio, U. Scotti di Uccio, C. Richter, S. Thiel, J. Mannhart, and L. Marrucci. Polar catastrophe and electronic reconstructions at the  $\text{LaAlO}_3/\text{SrTiO}_3$  interface: Evidence from optical second harmonic generation. *Physical Review B (Condensed Matter and Materials Physics)*, 80(7):075110, 2009.

# Acknowledgments

Here I would like to express my thanks to the people who have been very helpful during the time of my stage at University "Federico II".

First of all I would like to thank my supervisor Dr. Marco Salluzzo for giving me the opportunity to work in his group, gaining both knowledge and friends during this three years. I thank him for being both patient and decisive when needed.

For being my friends and sometimes colleagues during my stay in Napoli I owe my deepest gratitude to Milan, Gabriella and Fabio.

I warmly thank my colleagues: Roberto, Nathascia, Alessandro, Davide, Paolo.

I owe my special thanks to Prof. Giancarlo Abbate and Prof. Antonello Andreone, the coordinators of the PhD program, for support through these three years, and to Prof. Ruggero Vaglio, Prof. Umberto Scotti di Uccio, Prof. Lorenzo Marrucci and Dr. Fabio Miletto for the numerous scientific discussions.

Very special thanks to Guido Celentano for help in fight against Administrative problems in and out of University.

Finally, I would like to thank my family my mother Miroslavka, father Slobodan and my sister Jasmina for being patient with me all this years and for helping me in all possible ways, even when I was far from home.

This work was financially supported by the National Fellowship of Italian Government, and from the EU under the project Nanoxide, Contract No. 033191.